DOCTORAL THESIS

Dust Attenuation in Dusty Star-Forming Galaxies Using Spectral Energy Distribution

Author:
Mahmoud HAMED

Advisor:
Katarzyna MAŁEK
Auxiliary advisor:
Junais

*A thesis submitted in fulfillment of the requirements
for the degree of Doctor of Philosophy*

in the

NATIONAL CENTRE FOR NUCLEAR RESEARCH ŚWIERK

May 8, 2023

Declaration of Authorship

I, Mahmoud HAMED, declare that this thesis titled, "Dust Attenuation in Dusty Star-Forming Galaxies Using Spectral Energy Distribution" and the work presented in it are my own. I confirm that:

- This work was done wholly or mainly while in candidature for a research degree at the National Centre for Nuclear Research.

- Where any part of this thesis has previously been submitted for a degree or any other qualification at the National Centre for Nuclear Research or any other institution, this has been clearly stated.

- Where I have consulted the published work of others, this is always clearly attributed.

- Where I have quoted from the work of others, the source is always given. With the exception of such quotations, this thesis is entirely my own work.

- I have acknowledged all main sources of help.

- Where the thesis is based on work done by myself jointly with others, I have made clear exactly what was done by others and what I have contributed myself.

Signed:

Date:

NATIONAL CENTRE FOR NUCLEAR RESEARCH

Abstract

Dust Attenuation in Dusty Star-Forming Galaxies Using Spectral Energy Distribution

Mahmoud HAMED

Despite its low contribution to the total mass of the interstellar medium (ISM), dust plays a crucial role in the evolution of galaxies, and it has the biggest impact on the shape of their total spectral energy distribution (SED). Dust attenuates the stellar light by absorbing the short wavelength photons incoming from the newly-formed stars, and emits them thermally in the infrared (IR). The affluence of IR and radio detections of millions of galaxies, provided by powerful instruments such as Herschel and ALMA, has allowed us to study the cold dust in galaxies over a wide range of redshift.

To account for dust attenuation in models, one should assume a dust attenuation law which describes how stellar emission is absorbed by dust. Attenuation laws are representative of different distribution of dust relative to the stellar population, and they vary from simple screen models to more complex dust-stars geometries. These laws are represented by "curves" of attenuation, the slope of which dictates how much attenuation is dust causing on a specific wavelength range. Recent studies show a non-universality of dust attenuation curves when reconstructing galaxy SEDs. Moreover, assumed dust attenuation slopes can strongly alter the estimation of main physical properties of galaxies obtained by fitting the observed SED through theoretical models, such as the stellar masses. Therefore, dust attenuation slopes have a direct implication on our understanding of how galaxies build up their stellar masses through the cosmic times. Despite the growing knowledge in the field of extragalactic astronomy, key questions remain unanswered: What dust attenuation law one should use at high redshift? What are the physical conditions on which dust attenuation curves depend?

In this thesis, I aim at answering the aforementioned questions by analyzing the SEDs of galaxies and study the correlations between dust attenuation and various physical properties of these galaxies. First, I study a complex system of two galaxies around the cosmic noon ($z \sim 2$), one of these galaxies is a massive ultra dusty galaxy, detected by ALMA. I analyze the role of dust attenuation in these galaxies and most importantly, the importance of their morphology in determining their physical characteristics, such as their loci from the main sequence of star-forming galaxies.

To generalize the peculiar aspect of morphological extension of dust emission in dusty star-forming galaxies, I study the effect of star-to-dust spatial extension on the preferred dust attenuation law in these galaxies. For this, I build one of the largest ALMA-detected sample that is studied from the aspect of dust attenuation (122 galaxies in total), and derive the effective radii of these galaxies. With careful SED modeling of these galaxies, I derive key physical parameters that govern galaxy evolution and investigate the correlation between the relative compactness of stellar emission and dust emission on the one hand, and on the other hand the dust attenuation law preferred for these galaxies.

Lastly, I conduct a large study of dust attenuation relation at intermediate redshift, with a large sample of $\sim 1\,000$ galaxies from VIMOS Public Extragalactic Redshift Survey (VIPERS) that do not possess ALMA detection, therefore their dust continuum is inaccessible. However, I study the effect of their stellar continuum spatial distribution with the dust attenuation (in the IRX-β plane, where β is the UV slope and IRX is the IR excess). I also investigate the role of gas phase metallicity, the inclination of galaxies, and most importantly the environments in which they reside.

The results of these works show that the morphological properties of galaxies at different redshift ranges are highly important, and they should be taken into account as a prior for SED fitting, to accurately estimate the stellar masses and other quantities. Moreover, important correlations were found between dust attenuation and other physical properties, such as the metallicity, galaxy compactness, and the relative spatial extension of star-to-dust continua. I found that galaxies with relatively compact stellar emission preferred a steeper attenuation law, while galaxies with larger stellar emission preferred a shallow attenuation curve.

I found a strong dependence of the IRX-β dust attenuation relation on gas-phase metallicity, and also strong dependencies on stellar ages, stellar masses, specific star formation rates and the compactness of the sources characterized by the Sérsic indexes. Metallicity is one of the drivers of the dust attenuation scatter, this also results from the older stars and higher masses at higher β values. The correlation with specific dust mass is strong in shifting the galaxies away from the IRX-β relation towards lower β values. I find that more compact galaxies witness a larger amount of attenuation than less compact galaxies. There is a subtle variation in the dust attenuation scatter between edge-on and face-on galaxies, but the difference is not statistically significant. Galaxy environments do not significantly affect dust attenuation in star-forming galaxies at intermediate redshift.

These results are promising in the era of big surveys, with the James Webb Space Telescope (JWST) which is allowing us to expand our knowledge of high redshift galaxies, and the upcoming Legacy Survey of Space and Time (LSST) which will allow to detect a large number of galaxies with high resolution optical/UV maps. This will allow us to quantify compactness of millions of galaxies, and study their dust attenuation and emission.

Streszczenie

Dust Attenuation in Dusty Star-Forming Galaxies Using Spectral Energy Distribution

Mahmoud Hamed

Pomimo niewielkiego udziału w całkowitej masie ośrodka międzygwiazdowego, pył odgrywa kluczową rolę w ewolucji galaktyk. Ma on też znaczący wpływ na kształt widmowego rozkładu energii galaktyk. Pył tłumi światło gwiazdowe poprzez absorbowanie fotonów o krótkiej długości fali pochodzących od nowo powstałych gwiazd i emituje je termicznie w podczerwieni. W ostatnich latach, dzięki teleskopom podczerwonym oraz submilimetrowym, takim jak Kosmiczne Obserwatorium Herschela czy The Atacama Large Millimeter/submillimeter Array (ALMA), możliwe było zaobserwowanie zimnego pyłu w milionach galaktyk, w szerokim zakresie przesunięć ku czerwieni.

Aby uwzględnić istnienie pyłu podczas modelowania widma elektromagnetycznego galaktyk, należy założyć prawo tłumienia pyłu, które opisuje, w jaki sposób emisja gwiazdowa jest absorbowana przez pył. Prawa tłumienia są reprezentatywne dla różnych rozkładów pyłu w stosunku do populacji gwiazd i różnią się od prostych modeli ekranowych do bardziej złożonych geometrii pył – gwiazdy. Prawa te są reprezentowane przez krzywe tłumienia, których nachylenie określa jak silna jest absorpcja pyłu w danym zakresie długości fal. Ostatnie badania pokazują niejednorodność charakterystyk krzywych tłumienia pyłu przy rekonstrukcji SED galaktyk. Co więcej, założone nachylenie tłumienia pyłu w funkcji długości fali może silnie zmienić oszacowanie głównych własności fizycznych galaktyk uzyskanych przez dopasowanie obserwowanego SED do modeli teoretycznych. W szczególności bardzo silny jest wpływ założonej funkcji tłumienia pyłu na oszacowane masy gwiazdowe galaktyk. Dlatego też, nachylenie tłumienia pyłu ma bezpośredni wpływ na nasze zrozumienie tego, jak galaktyki budują swoje masy gwiazdowe w czasie kosmicznym.

Pomimo ciągle rosnącej wiedzy w dziedzinie astronomii pozagalaktycznej, kluczowe pytania pozostają bez odpowiedzi: Jakie prawo tłumienia pyłu należy stosować dla galaktyk znajdujących się na wysokim przesunięciu ku czerwieni? Jakie są warunki fizyczne galaktyk i ich otoczenia, od których zależą krzywe tłumienia pyłu? W niniejszej pracy staram się odpowiedzieć na powyższe pytania analizując widma energetyczne galaktyk i badając korelacje pomiędzy tłumieniem pyłu, a podstawowymi własnościami fizycznymi tych galaktyk. Najpierw badam złożony układ dwóch galaktyk w okolicach kosmicznego południa (z~2, czyli w okresie, kiedy tempo tworzenia gwiazd w galaktykach było najsilniejsze). Jedna z tych galaktyk jest masywną ultra pyłową galaktyką, wykrytą przez teleskop ALMA. Analizuję rolę tłumienia pyłu w tych galaktykach, a przede wszystkim znaczenie ich morfologii w określaniu ich cech fizycznych, takich jak ich położenie względem głównego ciągu galaktyk gwiazdotwórczych.

Aby uogólnić osobliwy aspekt wpływu morfologii na absorpcję i emisję pyłu w pyłowych galaktykach gwiazdotwórczych badanych w pierwszej części pracy, rozszerzyłem swoją analizę. W tym celu zbudowałem największą próbkę galaktyk na wysokim przesunięciu ku czerwieni (z~2) badaną pod kątem tłumienia pyłu, dla której dostępne są obserwacje ALMA (122 galaktyki). Dla tych galaktyk zmierzyłem promienie efektywne w zakresie ultrafioletowym i podczerwonym. Dzięki dokładnemu modelowaniu widm energetycznych, wyprowadzam kluczowe parametry fizyczne rządzące ewolucją galaktyk i badam korelację pomiędzy nimi. Skupiam się na emisji pochodzącej z widma części gwiazdowej i pyłowej z jednej strony, a z drugiej strony prawem tłumienia pyłu preferowanym dla tych galaktyk.

W ostatnim kroku mojej analizy przeprowadzam badanie relacji tłumienia pyłu dla galaktyk znajdujących się w połowie wieku istnienia Wszechświata ($z\sim0.7$). Dla tej próbk i nie są dostępne obserwacje submilimeterowe pochodzące z teleskopu ALMA, jednak próbka ta, pochodząca z VIMOS Public Extragalactic Redshift Survey (VIPERS) posiada obserwacje spektroskopowe, w tym też linie emisyjne. Badam wpływ rozkładu przestrzennego kontinuum gwiazdowego na tłumienie pyłu (w płaszczyźnie IRX-β, gdzie IRX zdefiniowane jest jako stosunek jasności w podczerwonym zakresie widma galaktyki do jasności w zakresie ultrafioletowym, natomiast β jest nachyleniem widma w zakresie ultrafioletu i jest wskaźnikiem tłumienia) dla tych galaktyk. Analizuję również rolę metaliczności gazu, kąta nachylenia w stosunku do obserwatora, a przede wszystkim środowiska, w którym przebywają.

Wyniki tych prac pokazują, że własności morfologiczne galaktyk są niezwykle istotne w różnych zakresach przesunięć ku czerwieni. Podczas modelowania widm energetycznych galaktyk własności te powinny zostać uwzględnione aby prawidłowo dobrać prawo tłumienia pyłu i w sposób poprawny oszacować masy gwiazdowe i inne wielkości fizyczne. Co więcej, znalazłem ważne korelacje pomiędzy tłumieniem pyłu a innymi właściwościami fizycznymi, takimi jak metaliczność, zwartość galaktyk i względne przestrzenne położenie obszarów gwiazdowych i pyłowych. Wykazałem, że galaktyki o stosunkowo zwartej emisji gwiazdowej preferowały silniej nachylone (w funkcji długości fali) prawo tłumienia, niż galaktyki o rozleglejszym obszarze emisji gwiazdowej.

Stwierdziłem silną zależność pomiędzy relacją IRX-β a metalicznością gazu oraz parametrami opisującymi populacje gwiazdowe: ich wiek, masa gwiazdowa, czy tempo formowania się gwiazd znormalizowane do masy gwiazdowej galaktyki. Również kształt fizyczny populacji gwiazdowej mierzony przez indeks Sersica ma wpływ na relację IRX-β. Metaliczność jest jednym z motorów zmienności tłumienia pyłu. Wyższa metaliczność oznacza, że w galaktyce znajdują się starsze populacje gwiazdowe, a co za tym idzie, także masa gwiazdowa jest większa - ma to silny wpływ na parametr β. Z moich analiz wynika, że im wyższa masa pyłu (normalizowaną do masy gwiazdowej) tym więcej młodych populacji gwiazdowych znajduje się w galaktyce. Ich emisja powoduje przesunięcie galaktyk o wyższej masie pyłu w kierunku niższych wartości galaktyk od relacji IRX-β w kierunku niższych wartości β. Z moje analizy wynika, że bardziej zwarte galaktyki są świadkami większego tłumienia niż galaktyki mniej zwarte. Istnieje subtelna różnica w rozproszeniu tłumienia pyłu w zależności od nachylenia kąta galaktyki w stosunku do obserwatora, ale różnica ta nie jest statystycznie istotna. Równocześnie, otoczenie w jakim znajduje się galaktyka nie wpływa znacząco na tłumienie pyłu dla galaktyk znajdujących się około 7 miliardów lat od nas ($z\sim0.7$).

Wyniki te są obiecujące w erze wielkich przeglądów, takich jak James Webb Space Telescope (JWST), który pozwala nam poszerzyć wiedzę o galaktykach o wysokim przesunięciu ku czerwieni i jeszcze dokładniej zbadać relacje pył - populacje gwiazdowe. Również Legacy Survey of Space and Time (LSST) - nadchodzący wielki przegląd optyczny, będzie obserwował setki tysięcy galaktyk za pomocą map optycznych/UV o wysokiej rozdzielczości. Badania nad zależnością tłumienia pyłu od czynników związanych z koncentracją gwiazd, rozmiarami obszarów gwiazdowych, metalicznością i innymi właściowościami fizycznymi galaktyk pozwoli na właściwe oszacowanie tłumienia pyłu i prawidłową analizę fizyczną tych obiektów.

Acknowledgements

I would like to thank Kasia for her support, trust, and for believing in me during these years. I am grateful for having the most loving and supporting family, some of which did not live long enough to see me as a PhD. I thank Mama and Baba for their endless support and for letting me follow my dreams. I thank Lidia for being the light in my life, I am incredibly fortunate to have her with me. The future is the brightest for both of us. I thank my partner Tiago, meeting you has changed my life for the better. Thank you for accompanying me during these years and for standing by my side, and for providing me with strength and inspiration. I thank all the friends and comrades that I got the chance to meet during this journey. Especially I thank Gabriele for making those four years not only bearable, but also enjoyable. Pazienza. I thank Francesco, Prasad, and all the PhD students who endured or are enduring this, and who accompanied me everyday during these four years. Nikita, this is also for you, hope you feel proud. I thank Monika for helping me with bureaucracy and for keeping this place functioning. I especially thank her for helping me with the Preludium grant, and filling tens of documents for me. I am grateful to the National Science Centre for trusting me enough to make me a PI for my projects. I also thank everyone I met in Warsaw. I consider myself one of the luckiest people who have this huge amount of support and love from family and friends. I wish everyone the same...

x

Contents

List of Figures

List of Tables

To my family, and to my younger self...

1

Introduction

Since the advent of modern astronomy in the last few decades, the number of observed galaxies has proliferated. This has led to a realization that these objects are not merely ordinary entities inhabiting the rapidly expanding universe. In fact, galaxies possess characteristics comparable with living organisms, undergoing a life cycle that involves birth, growth, and death. The field of extragalactic astrophysics has undergone exponential growth, owing primarily to the multiplication of advanced astronomical facilities equipped with powerful telescopes. This has enabled us to explore the universe beyond the boundaries of our own Milky Way. With the aid of these sophisticated instruments, we have acquired a wealth of knowledge pertaining to the processes underlying star formation and evolution within galaxies.

The baryonic matter represents around 5% of the total content of the Universe today (Planck Collaboration et al., 2020). Within this small fraction, it was estimated that only a few percent of the baryonic mass in the Universe is contained in galaxies (Carlstrom et al., 2002; Shull et al., 2012; Nicastro et al., 2018). This mass is mainly made of stars, gas, and dust. Interstellar dust accounts for a mere 1% of the total baryonic mass in the interstellar medium (ISM) (Popping et al., 2017; Galliano et al., 2018).

Despite this small contribution to the overall mass of the baryonic matter within galaxies, interstellar dust plays a crucial role in galaxy evolution. These dust particles are typically small, with sizes ranging from a few nanometers to a few micrometers (Weingartner et al., 2001; Draine et al., 2007). Interstellar dust particles are made of complex compounds comprising various elements such as oxygen, carbon, iron, silicon, and magnesium. These elements are synthesized by stars during their lifetime and then ejected to the ISM during supernova explosions. In the ISM, dust grains undergo different physical and chemical processes. Part of this dust will eventually end up in dense and cold molecular clouds, where it acts like a radiation shield from the stars, cooling down the molecular gas in these clouds. This in turn allows the gas to remain cool and dense enough to undergo gravitational collapse and form future stars (Slavin et al., 2020).

Besides the cooling effect that dust grains provide in the dense molecular clouds, dust within these clouds provides a surface onto which atomic hydrogen gas can assimilate and form molecular hydrogen, which is the primary fuel of star formation (Wakelam et al., 2017). Therefore, interstellar dust is vital in the most important baryonic event in galaxies, i.e. star formation. The dynamic presence of dust in every aspect of star formation, makes it a driving force of the evolution of galaxies.

Interstellar dust does not only contribute to the stellar formation process, but it also completely reshapes the spectral energy distribution (SED) of galaxies. It absorbs and scatters light efficiently, especially that of the young stars emitting in the ultraviolet (UV) (Draine, 2003a), making the stellar light appear dimmer. This dimming can make it harder to detect young, blue stars that are indicative of recent star formation (e.g., Kennicutt et al., 2007).
On the other side of the electromagnetic spectrum, dust predominantly re-emits thermally in the infrared (IR). This thermal emission of interstellar dust can be in the wavelength range of a few micrometers to several hundred micrometers. The exact range depends a lot on the temperature of the dust, which in turn depends on its distance from the stellar radiation field. In general, warmer dust emits at shorter wavelengths, while cooler dust emits at longer wavelengths (Dale et al., 2002).

The complex dynamics of interstellar dust and its consequences on galaxies' spectra, are of high importance at higher redshifts, when the Universe was younger. In fact, the young Universe was much dustier than it is today (Dwek et al., 2007; Hirashita et al., 2014; Béthermin et al., 2015; Hirashita et al., 2017; Shen et al., 2022). This is due to a number of factors, including the abundance of heavy elements produced by the first generation of stars, and the high star formation rate (SFR), and supernova explosions in the early Universe (Michałowski et al., 2012; Madau et al., 2014; Schreiber et al., 2015; Béthermin et al., 2017). Therefore, higher redshift SFR is largely more obscured by dust (Takeuchi et al., 2005; Whitaker et al., 2017). To have a complete picture of the evolution of galaxies accross cosmic time, it is therefore necessary to understand how dust behaves in the ISM.

Today, we are witnessing an unprecedented technological advancement in extragalactic astronomy. With new observational facilities and telescopes, we are able to gain a panchromatic view of galaxies at different epochs of the Universe. For instance, with the James Webb Space Telescope (JWST), The Large Synoptic Survey Telescope (LSST), and the Atacama Large Millimeter Array (ALMA), observational data are becoming more and more robust. This opens a new era of observational astrophysics, where a parallel improvement in modeling is required, in order to understand the physics of the earlier galaxies.

1.1 Spectral energy distribution: Panchromatic view of galaxies

Galaxies emit photons across the whole electromagnetic spectrum. Short wavelength UV photons are mostly incoming from the young stars. However, the determination of the SFR of galaxies at high redshift is not straightforward. To compute the instantaneous SFR, one should model the star formation history (SFH), and evidently dimming of starlight, i.e. dust attenuation.
The SFH describes the rate at which stars formed in a galaxy over its lifetime, as well as the duration and intensity of periods of enhanced or reduced star formation. The SFH can be determined through a variety of methods, including analyzing the color-magnitude diagrams of resolved stellar populations (Cook et al., 2019), studying the spectral features of integrated light (Ruiz-Lara et al., 2015), and modeling the chemical abundances of stars in nearby galaxies (Snaith et al., 2015). However, SFHs of high redshift galaxies are hard to determine due to lower resolutions. This can be overcome by models that account for different types of SFHs, which are described in section 1.1.1.

Interstellar dust will dim the young, recently-formed stars, by absorbing a significant fraction of their emission, and re-emit it in the IR. This means that the IR emission contains information about the hidden SFR. Therefore, accurately accounting for this reprocessed

energy will provide a more accurate determination of SFR. In the following subsections, the most important aspects of the SED will be covered. An example of an SED of a galaxy is shown in Figure 1.1.
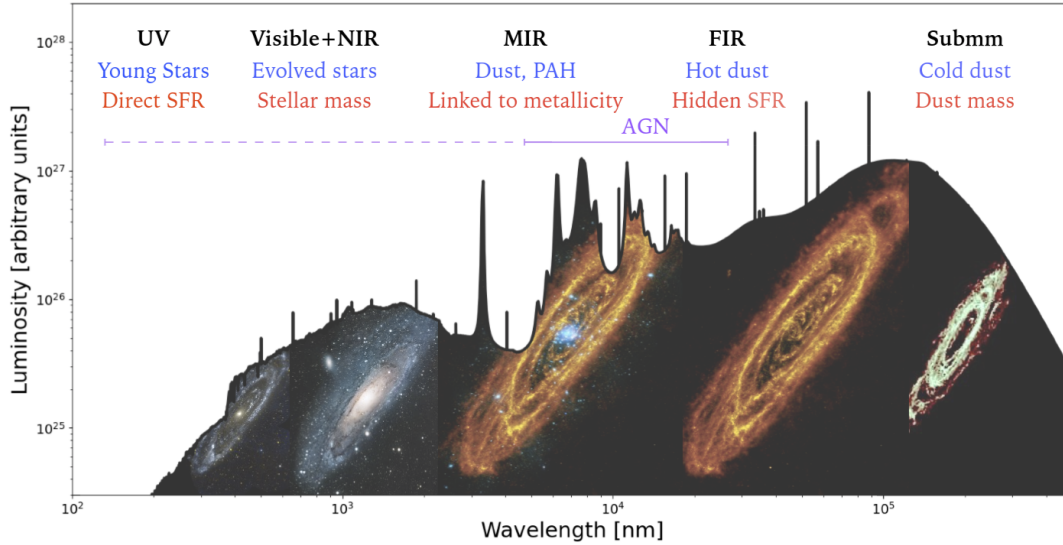
FIGURE 1.1: SED of a mock galaxy highlighting the most important physical observables in each wavelength range. The background images show the M31 galaxy at different wavelengths. Images are credited to ESA.

1.1.1 Stellar emission

Stars are the main source of light in galaxies, whether it is direct or indirect. The vast majority of the UV to optical light in star-forming galaxies is incoming from the stars (Sparke et al., 2007). Other less significant light sources are gas clouds and active galactic nuclei (AGN) if present. The UV photons in the ISM are directly traced back to the young stellar continuum emission, and therefore can be regarded as a direct indicator of the SFR. In normal star-forming galaxies, stars younger than 200 Myr contribute to 90% of the UV emission of these galaxies (Hao et al., 2011; Murphy et al., 2011; Kennicutt et al., 2012).

Older stars constitute the majority of the stellar mass in galaxies because they have more time to form and accumulate over the course of galaxies' evolution. Thus, estimating stellar masses of galaxies can be done by integrating their optical to near-infrared (NIR) spectra (Bell et al., 2003; Taylor et al., 2011; Meidt et al., 2014). However, the determination of the stellar mass of galaxies strongly depends on the assumed models of the initial mass function (IMF), SFH, and dust attenuation. The IMF of galaxies describes the relative number of stars that form with different masses in a population of stars. The shape of the IMF was determined empirically by studying the distribution of stellar masses in a given stellar population (Salpeter, 1955; Kroupa, 2002; Chabrier, 2003). Although the choice of the IMF can affect the results of SED fitting of galaxies to some extent, the magnitude of the effect is not very large (Pforr et al., 2012; McGee et al., 2014; Clauwens et al., 2016).
The choice of a SFH on the other hand, leaves a strong impact on the determination of the stellar masses and the SFR of galaxies. Stellar mass is typically estimated by comparing the observed SED of a galaxy to a set of theoretical models that describe the luminosity and colors of stars at different ages and metallicities (e.g., Bruzual et al., 2003). The SFH determines the relative contributions of stars of different ages. Therefore, the choice of SFH can affect the inferred stellar mass by changing the assumed mix of stellar populations. At high

redshift, however, it is often difficult to describe the SFH of unresolved galaxies (Pacifici et al., 2016; Zhang et al., 2017). To overcome this challenge, many models are available to describe past episodes of star formation. Generally speaking, a delayed version of exponentially declining SFH can describe the star formation activity in normal star-forming galaxies. This type of SFH is more physical than constant SFHs. It assumes that the majority of the stars in galaxies were formed early during their formation, followed by a decline as galaxies grow more massive and lose their gas reservoirs (Ciesla et al., 2017; Chevallard et al., 2019). However, at higher redshift, to account for the boosted SFRs that we observe in e.g., dusty star-forming galaxies (DSFGs), an additional recent burst in SFH is required. This flexible SFH can limit the degeneracies with other physical properties that occur in the short wavelength range (Ciesla et al., 2018; Aufort et al., 2020).

Attenuating the stellar emission by interstellar dust when constructing an SED of a galaxy, affects the derivation of its physical properties like no other SED component. Therefore the treatment of dust attenuation in galaxies should be performed carefully. Dust attenuation is discussed in the following section, where many attenuation recipes are presented along with their effect on observables that govern galaxy evolution.

1.1.2   Dust attenuation

B, V, I   B, I, K
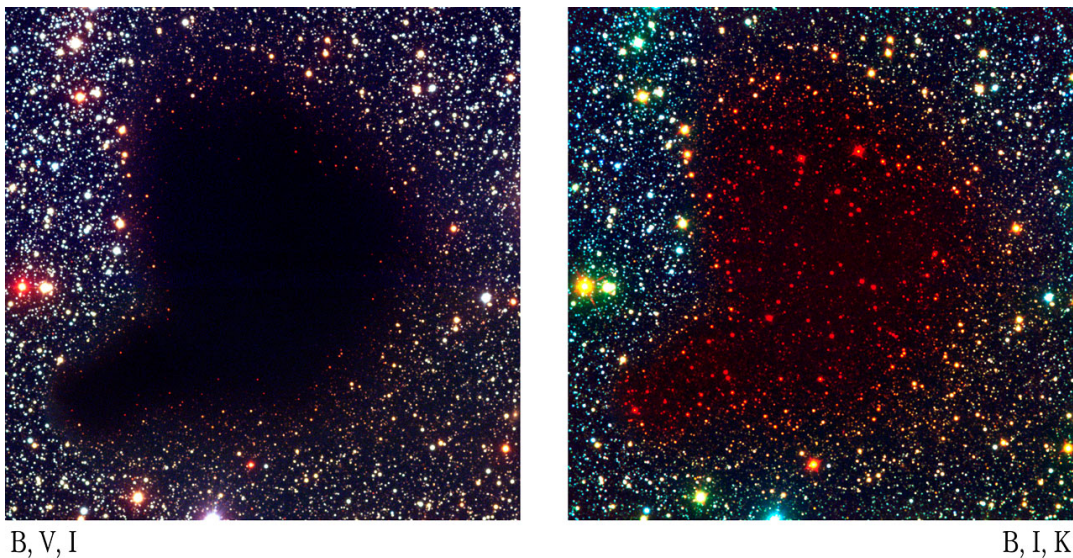
FIGURE 1.2: A comparison of the Barnard 68 molecular cloud in a color composite of visible and near-infrared on the left and infrared on the right. Credits: ESO.

With the strong effect that dust plays in the lifecycle of galaxies and their ISM, dust attenuation is the leading aspect to consider when performing SED fitting. Dust attenuation is the process in which interstellar dust particles absorb and scatter stellar light, leading to a reduction in the observed intensity of light from distant objects, such as galaxies. The history of dust attenuation of galaxies is a fascinating story that spans over a century, as astronomers tried to study the nature and effects of dust on our observations of the Universe. Historically, astronomers in the early 20th century noticed that the light from distant stars appeared redder than expected (e.g., Russell, 1922; Eddington, 1926). This phenomenon, known as reddening, was later explained as the result of the absorption and scattering of blue light by interstellar dust grains. Figure 1.2 shows the Barnard 68 molecular cloud, as seen with optical bands (left) and in IR (right). While these early observations and discussions of reddening

did not explicitly mention galaxies, they laid the groundwork for the later development of the concept of dust attenuation and its effects on astronomical observations. However, it was not until the 1930s that astronomers began to consider the impact of dust on the observations of galaxies ("obscuring clouds" in Hubble 1934). These works and other consequent ones, marked the beginning of a more systematic study of dust attenuation in galaxies, and laid the foundation for later developments in the field.

Nowadays, dust remains an important area of research in astronomy. With the advent of telescopes such as the Hubble Space Telescope and the Atacama Large Millimeter/Submillimeter Array (ALMA), astronomers are able to study dust in galaxies with unprecedented detail and resolution. Sophisticated models were developed that take into account the interplay between dust and stars in galaxies. These models are based on a combination of theoretical calculations and observations of dust, from the local Universe to distant galaxies. Attenuation is a complex phenomenon that is influenced not only by the geometry of stars and dust, but also by the properties of dust grains and the scattering of light (Trayford et al., 2020). Radiative transfer models are also needed to accurately model this process (Weingartner et al., 2001; Narayanan et al., 2015). The attenuation curves are constructed based on the extinction curves. Loss of light due to absorption or scattering along the line of sight is referred to as extinction, whereas attenuation encompasses both extinction and the effects of obscure stars and scattering back into the line of sight. The geometrical arrangement of stars and dust within a galaxy plays a significant role in determining the extent of attenuation (Salim et al., 2020). In this section, some of the widely used attenuation laws will be presented.

The Calzetti et al. (2000) dust attenuation law

The dust attenuation law proposed by Calzetti et al. (2000, herafter C00) is a widely used model that describes the effects of dust on the observed spectra of galaxies. It is one of the most used attenuation laws today and is a standard tool for analyzing the properties of galaxies across a wide range of wavelengths. This law was developed in response to earlier observations of galaxies that suggested that the effects of dust on their spectra were more complex than had been previously thought. In particular, astronomers had noticed that the SEDs of some galaxies exhibited features that could not be explained by simple models of dust attenuation, such as the screen model that assumes a uniform distribution of dust along the line of sight.

The C00 law was derived empirically through the analysis of a sample of 40 nearby starburst galaxies. This analysis was based on the comparison of the observed UV fluxes of these galaxies with theoretical models that predicted the expected UV flux in the absence of dust attenuation. The derivation of the attenuation law was then achieved by assuming a functional form for the attenuation curve. The choice of local starburst galaxies is ideal, since they are UV-bright. C00 then derived the dust attenuation of these galaxies by using the observed UV spectral slope and correcting it for the effects of dust absorption. The method involved calculating the intrinsic UV spectral slope of a galaxy, which represents the UV radiation emitted by stars before it is absorbed or scattered by dust. They used an extinction curve based on the properties of individual stars to correct for the effects of dust attenuation. This curve describes how the light from stars is attenuated as it passes through the interstellar medium. By applying this curve to the observed UV spectral slope, C00 were able to derive the dust attenuation of galaxies.
This law was modified by several consequent works when applied to different samples of galaxies, giving a flexible approach to the original law.

In general, the C00 attenuation law can be written as:

$$k(\lambda) = \left(\frac{A(\lambda)}{E(B-V)}\right) \times \left(\frac{\lambda}{\lambda_V}\right)^\delta, \tag{1.1}$$

with δ being the slope of attenuation, $k(\lambda)$ is the attenuation curve at a given wavelength λ, $A(\lambda)$ is the extinction curve, and E(B-V) is the difference between the observed B and V color index and the intrinsic value for a given stellar population. In the original C00 law, $\delta=0$.
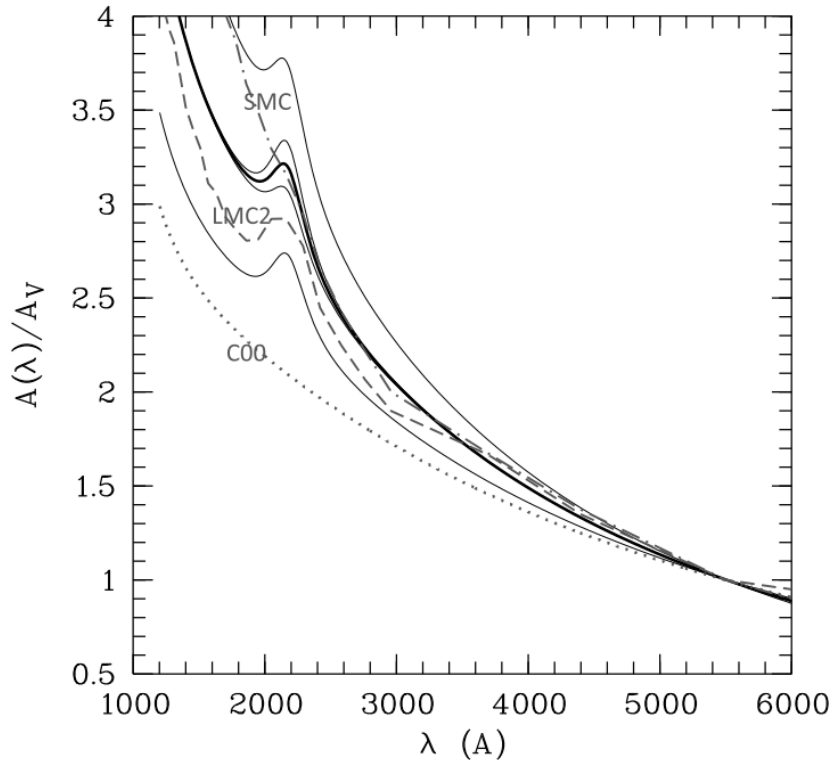
FIGURE 1.3: Variation attenuation as a function of wavelength, normalized to the V band attenuation. The dotted line shows the C00 attenuation. The dashed line shows the extinction curve of the Large Magellanic Cloud supershell. The dot-dashed line shows the extinction of the Small Magellanic Cloud. The black bold line shows the mean attenuation of a sample of galaxies around $z = 2$ from Buat (2013). This plot was taken from Buat (2013).

Figure 1.3 shows the attenuation law of C00 along with other well-studied extinction curves of the nearby Magellanic clouds. In the literature, many recipes of the original C00 law exist, e.g., modifying it with a UV bump at 217.5 nm (e.g., Buat et al., 2011, 2012). In Equation 1.1, the term $(\lambda/\lambda_V)^\delta$ allows for modifications of the C00 law by varying the obscuration with different slopes δ.

In the treatment of star-to-dust geometry, the C00 law assumes a foreground dust screen model, replicating the fact that the starburst regions of the UV-bright galaxies are encompassed by dust (Calzetti et al., 1994; Calzetti, 2001). This attenuation law is flatter than that of the Milky Way and the Magellanic Clouds (Figure 1.3).

Despite its relative simplicity, the C00 attenuation curve succeeds in reproducing the observed UV spectra of different types of galaxies (e.g., star-forming galaxies, AGNs) at different redshift ranges (e.g., Ciesla et al., 2015; Buat et al., 2019; Decleir et al., 2019).

The Charlot et al. (2000) dust attenuation law

Besides the empirical attenuation law given by C00, another very commonly used attenuation law is that of Charlot et al. (2000, hereafter, CF00). This model is different in its approach to the stellar light dimming problem, as it assumes different attenuation for the young and old stellar populations, therefore introducing a more complex dust-to-star mixing geometry.
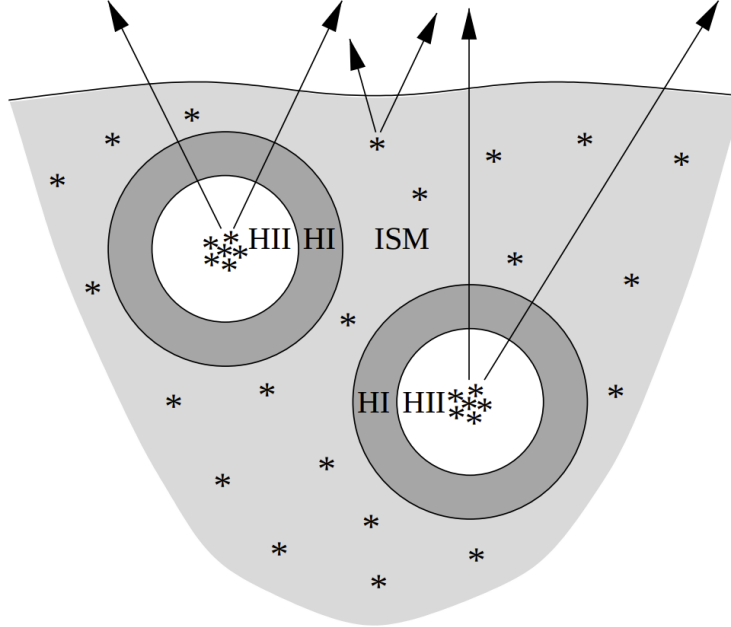
FIGURE 1.4: Simple illustration depicting the birth clouds and surrounding ambient ISM of stars. In the inner regions of dense molecular clouds, young stars are born. The ambient ISM contains the old stars. Dust is in both the H_{II} and H_I regions of the birth clouds, and within the ambient ISM. Arrows represent the light traveling through the birth clouds and the ISM, depending on its origin. Illustration taken from Charlot et al. (2000).

The different attenuation for the young and older stars reflects the fact that younger stars are typically found in more dusty environments than older stars. This difference in attenuation can be attributed to the way in which dust is distributed within galaxies, with younger stars being born in regions where the dust is still concentrated. This law distinguishes between the demographics of a given stellar population, with the classification of stars as old or young determined by the duration t_0 of escaping the birth clouds (BC). Young stars are assumed to disperse from the birth clouds within t_0. The t_0 is typically assumed to be 10 Myr.
to summarize the concept of CF00, The attenuation experienced by stars in the birth cloud is caused by both the ISM and the birth cloud itself, whereas stars in the ISM are only affected by the dust contained in their ambient surrounding, as depicted in Figure 1.4. Following this law, the attenuation in the BC and that in the ISM can be expressed as follows:

$$
\begin{cases}
A^{\text{ISM}}_{(\lambda)} = A_{V(\text{ISM})} \left(\frac{\lambda}{\lambda_V} \right)^{-\delta_{\text{ISM}}} \\[2ex]
A^{\text{BC}}_{(\lambda)} = A_{V(\text{BC})} \left(\frac{\lambda}{\lambda_V} \right)^{-\delta_{\text{BC}}},
\end{cases}
\tag{1.2}
$$

where δ_{ISM} and δ_{BC} are the power-law exponents of the ISM and the BC respectively. This makes the young stars experience an attenuation equal to $A^{\text{BC}}_{(\lambda)} + A^{\text{ISM}}_{(\lambda)}$, while the older

stellar population will undergo an attenuation worth $A_{(\lambda)}^{\mathrm{ISM}}$. In its original form, CF00 found that a slope value of $\delta_{\mathrm{ISM}} = \delta_{\mathrm{BC}} = 0.7$ being consistent with the observed SEDs of a large sample of nearby galaxies.

Additionally, the V band attenuation that acts upon the young stars and the old ones is expressed through a ratio μ, given by:

$$\mu = \frac{A_V^{\mathrm{ISM}}}{(A_V^{\mathrm{ISM}} + A_V^{\mathrm{BC}})}. \tag{1.3}$$
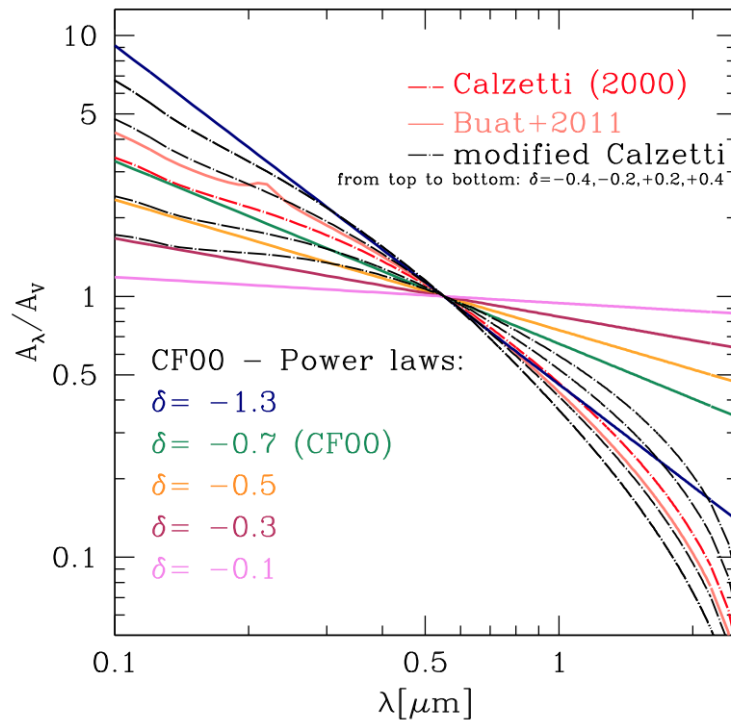
FIGURE 1.5: Different attenuation laws are shown with different power-law slopes for both the ISM and the BC. The original CF00 recipe is shown in green, both δ_{ISM} and δ_{BC} are set to the initial value of the CF00 recipe. The C00 law is shown in a red dash-dotted line. The CF00 law can be modified with different slopes, making the total attenuation curve shallower or steeper. This Figure was taken from Lo Faro et al. (2017).

Many studies using this attenuation law kept the original value of the slope of $\delta = 0.7$ for both the ISM and the BC (e.g., Buat et al., 2019; Villa-Vélez et al., 2021; Figueira et al., 2022; Carnall et al., 2023). However, other works changed these slopes either by keeping the slope parameters free (e.g., Lo Faro et al., 2017; Wang et al., 2020), or by adopting $\delta^{\mathrm{BC}} = 1.3$ (da Cunha et al., 2008; Battisti et al., 2019). This was done to better fit their samples.

In general, a higher slope value is often referred to in the literature as "grayer" or "shallower" version of the attenuation law. Having a shallower attenuation slope will result in a more significant older stellar population fraction that is attenuated. Depending on the redshift and the type of galaxies, the slopes of this law can be modified in order to better reproduce the observed spectra Lo Faro et al. (e.g., Lo Faro et al. 2017, found that $\delta^{\mathrm{ISM}} = 0.48$ is most adapted for ultra-luminous IR galaxies (ULIRGs) around the cosmic noon). This is due to the higher attenuation they exhibit in the NIR range, which makes the shallower version of

CF00 account for the dimmed older stellar population.

The variation of both the ISM and BC slopes in the CF00 law, along with the C00 law are shown in Figure 1.5. One could see the effect shallower curves (e.g., $\delta = -0.1$) are efficiently attenuating at higher wavelengths in the NIR range, which can be traced largely to the old stars in the ISM.

The values initially adopted in CF00 for δ, t_0, and μ were determined by fitting the same sample of starburst nearby galaxies that C00 used, initially from Meurer et al. (1999). Although these values can fit a large variety of galaxies, shallower curves and a large variation of the μ parameter are needed to model dust attenuation in other types of objects, e.g., in ULIRGs at high redshift.

1.1.3 Dust emission

After interstellar dust absorbs and scatters light, leading to obscuration and reddening of starlight, it primarily emits thermal radiation in the IR regime (Figure 1.6). This dust radiation can provide crucial insights into the physical conditions and processes occurring in galaxies, such as star formation and the heating mechanisms of the ISM. In this section, the current understanding of dust emission in galaxies will be reviewed.
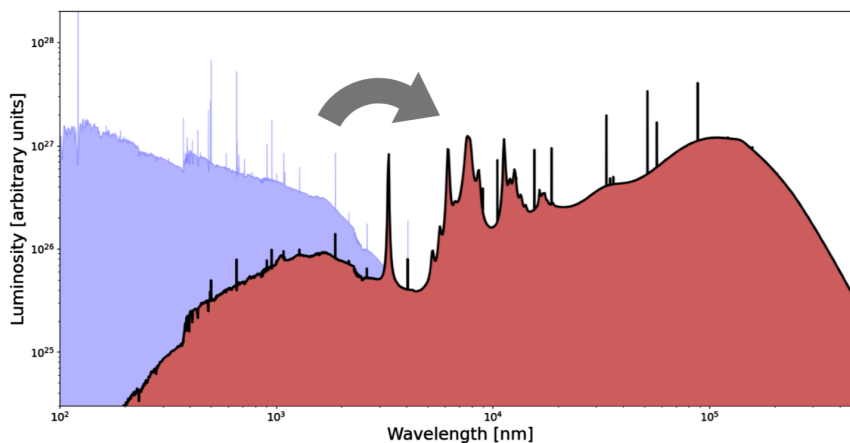
FIGURE 1.6: Exemplary SED of a galaxy is shown. The violet region shows the initial stellar light that is lost by dust absorption. The red region shows the total SED with a big part of it being in the IR domain, which is emitted by dust.

Dust grains in galaxies are typically composed of silicates, carbonaceous materials, and polycyclic aromatic hydrocarbons (PAHs). The size distribution of dust grains follows a power-law distribution with a peak at around 0.1 microns, although larger grains can also be present in varying proportions (Masaki et al., 2012; Asano et al., 2013; Hirashita et al., 2013). The size distribution affects the absorption and emission properties of dust, with larger grains being more efficient at absorbing and re-emitting radiation in the mid-IR and far-IR regimes. In these regimes, dust emission can be typically observed in galaxies, with a peak in the SED at around $100\,\mu$m. Dust temperature can be inferred from the shape of the SED, with warmer dust emitting more strongly at shorter wavelengths.

PAH emission is a prominent feature observed in many galaxies. These complex organic molecules are excited by ultraviolet and optical photons and emit in the mid-IR region of

the electromagnetic spectrum. This emission is widely used as a tracer of star formation activity in galaxies. The strength of the PAH emission correlates with the amount of dust and the SFR in galaxies (Kennicutt et al., 2009; Takagi et al., 2010; Shipley et al., 2016; Xie et al., 2019; Zhang et al., 2023), making it a valuable tool to estimate the SFR in galaxies that are too distant or too faint to be resolved. Furthermore, the PAH emission is sensitive to the ionization state of the gas, and it has been used to study the ionizing radiation field in galaxies (Lebouteiller et al., 2007; Wenzel et al., 2020; Xie et al., 2022).

The origins of PAH emission in galaxies remain a hot topic in astrophysics. They are thought to form in the atmospheres of carbon-rich stars (Gielen et al., 2011; Seok et al., 2014; Guzman-Ramirez et al., 2015). Once injected into the ISM, the PAHs are processed by a variety of physical and chemical processes, like heating by interstellar radiation.
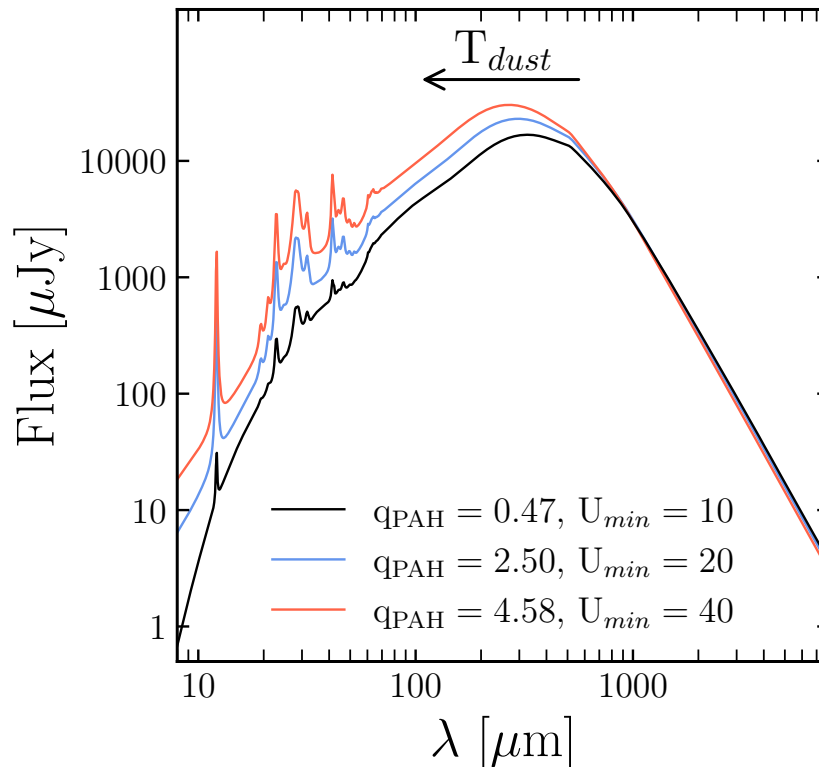
FIGURE 1.7: Examples of IR emission templates with different PAH fractions (q_{PAH}), and radiation field U. The Figure was obtained by simulating the dust emission with the Code Investigating GALaxy Emission, using Draine et al. (2014) models.

To account for all of the known and unknown composites of interstellar dust is a challenging task. However, models of dust emission based on the known composites and their abundances and sizes, along with observational features of dust, do exist (e.g., Draine et al., 1984; Desert et al., 1990; Dale et al., 2002; Draine et al., 2007, 2014). Though, a unique dust emission model does not exist due to observational limitations. Most of the proposed models consist of grains of silicate, graphite, and PAHs. These grains dictate the spectrum of dust emission, after they absorb the energy of the radiation field in galaxies. This radiation field consists mainly of the radiation emitted by stars, especially the hot young stars in normal star-forming galaxies.

Generally, dust emission shows the features of PAHs at around ~10 μm. As we move at longer wavelengths, the emission is increasingly dominated by the presence of small, warm

dust grains that are typically heated by radiation fields. For wavelengths beyond $100\,\mu$m, the emission is predominantly due to large, comparatively colder dust grains. The heating mechanisms of these various dust species, as well as their composition and metallicity, collectively influence the dust SED. Figure 1.7 shows examples of dust SEDs with different PAH fractions, and different minimal radiation fields incoming from the young stars. High fractions of PAHs add prominent features at the beginning of the IR emission. A stronger radiation field shifts the peak of the dust SED to the shorter wavelengths, showing higher dust temperatures.

1.2 The IRX-β dust attenuation relation

The effect of an attenuation law can be characterized by the UV slope β, which is obtained by fitting the observed flux F(λ) in the UV range as:

$$F(\lambda) \propto \lambda^{\beta}. \tag{1.4}$$

Calzetti et al. (1994) found that this UV slope correlates with the ratio in the optical depth between H$_\alpha$ and H$_\beta$, known as the Balmer optical depth:

$$\tau'_B = \tau_\beta - \tau_\alpha = ln\left(\frac{H_\alpha/H_\beta}{2.88}\right) \tag{1.5}$$

which measures the extinction of H$_\alpha$ relative to H$_\beta$. This correlation is seen in Figure 1.8 where different UV ranges were used in order to obtain β. This finding has important implications for future research, such as the work of Meurer et al. (1999), which aimed to leverage the linearity between the UV slope β and dust extinction, to gain a deeper understanding of dust attenuation in galaxies.
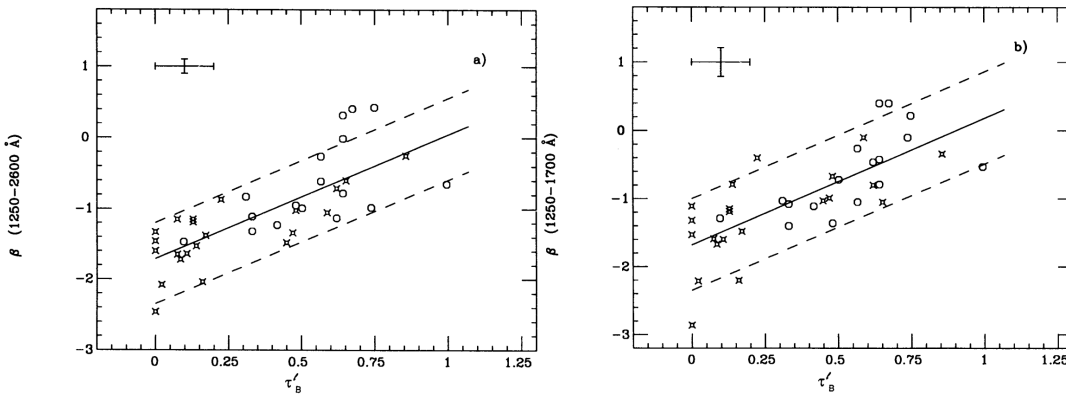
FIGURE 1.8: UV power-law slope β variation with the Balmer optical depth τ'_B in a sample of nearby galaxies (taken from Calzetti et al. (1994)). *Left panel:* β is obtained by fitting a wavelength range of 0.125 to 0.260 μm. *Right panel:* β is obtained by fitting a wavelength range of 0.125 to 0.170 μm.

Using the same sample of nearby starburst galaxies that Calzetti et al. (1994) used, Meurer et al. (1995) and Meurer et al. (1999) found a strong relation between the UV slope β and the infrared excess of galaxies (IRX). This connection was defined by the dust luminosity over the UV luminosity. As β was found to be directly proportional to attenuation (Calzetti et al., 1994), IRX was found to have a linear relationship with the attenuation of the FUV

band, making IRX a useful indicator of dust attenuation as well (Meurer et al., 1999; Gordon et al., 2000).

The Infrared excess (IRX) is commonly expressed as the ratio of the IR luminosity to the UV luminosity. Mathematically, this ratio can be expressed as:

$$IRX = \frac{L_{IR}}{L_{UV}}. \tag{1.6}$$

The IRX-β dust attenuation relation is based on the idea that the amount of dust in a galaxy will absorb and scatter the UV light emitted by young, massive stars, and re-emit it in the IR part of the spectrum. This is done by conserving the total spectral energy. The IRX-β can be seen as being shaped by dust attenuation. Although this relationship is expected, it is still unclear what causes the variation and whether it is universal.

Despite the fact that this relation was well investigated in different galaxy types and redshift ranges, its universality is debated. Many outliers were found in this relation, such as galaxies with high dust attenuation and high IRX values. These galaxies may have undergone unusual or extreme star formation, such as ULIRGs at high redshift (Casey et al., 2014; Álvarez-Márquez et al., 2016; McLure et al., 2018). Figure 1.9 shows two examples of the IRX-β
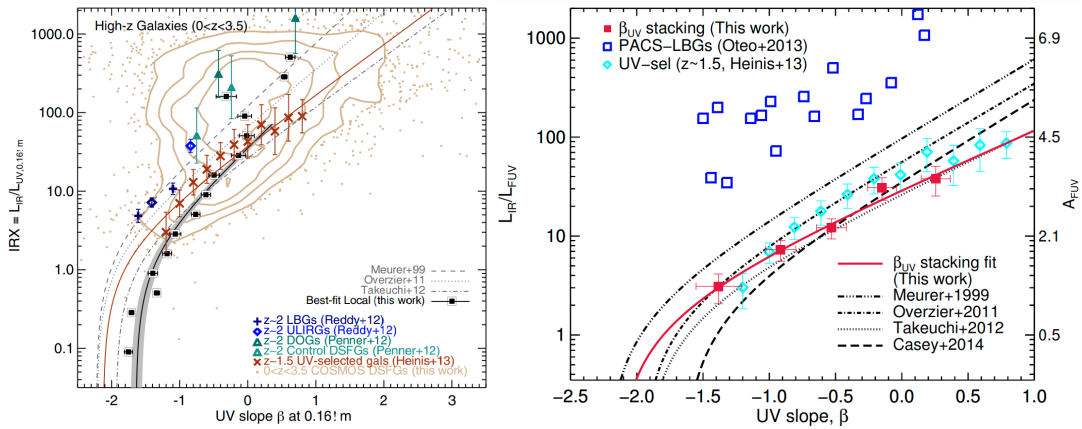
FIGURE 1.9: IRX-β relation of different galaxy samples. In the left panel: galaxies at redshift ranges varying from the local Universe to $z = 3.5$. These galaxies have detections in the FIR. This Figure is from Casey et al. (2014). In the right panel: high redshift galaxies with IR detections, taken from Álvarez-Márquez et al. (2016).

scatter from Casey et al. (2014) and Álvarez-Márquez et al. (2016). The UV-selected galaxies from Casey et al. (2014) follow the relation, while the ULIRGs and the dust-obscured galaxies (DOGs) are above the fit from Meurer et al. (1999). Similarly, in Álvarez-Márquez et al. (2016), IR-detected galaxies are above the relation of Meurer et al. (1999).

1.3   Estimating physical properties of galaxies

In this section, I will present some of the methods to estimate key physical properties that govern galaxy evolution. Although there are many physical quantities that affect the life-cycle of a galaxy, here the most important ones will be presented. These quantities that are essential for this thesis are the stellar mass, SFR, dust luminosity, mass, and temperature.

1.3.1 Stellar mass

Stellar mass, or $M_\star$, is a crucial characteristic of galaxies. Estimating it, allows us to understand how galaxies evolve and gives us an idea about the cosmic assembly of mass. The simplest technique in estimating the stellar mass of galaxies is by studying the stellar mass-to-light ratio ($M_\star/L$) (Bell et al., 2001, 2003). This technique is based on the idea that the luminosity emitted from stars is correlated to their masses. This is typically done assuming a simple stellar population model such as Bruzual et al. (2003), and measuring colors of galaxies in optical-near IR bands. Being a simple technique, also makes it uncertain, as color-based stellar mass-to-light ratio estimations do not involve correcting for dust attenuation. Even when correcting for dust attenuation (such as in Zibetti et al. 2009), derived stellar masses are found to be sensitive towards assumed SFHs and metallicities of the stellar population (Maraston et al., 2006; Cimatti et al., 2008; Muzzin et al., 2009).

Another technique for estimating the stellar mass of a galaxy is the broadband photometry fitting. This technique relies on detections in the UV to NIR bands, and fitting the SED of the observed fluxes. Deriving the stellar mass is achieved by assuming a SFH and stellar population model, and attenuating the stars with dust (e.g., Shapley et al., 2001; Taylor et al., 2011). Although estimating $M_\star$ using SED fitting is sensitive towards the assumed dust attenuation (this will be discussed in detail further on in this thesis), the mass can be sensitive towards the assumed SFH.

A general flexible SFH model can be written as:

$$SFR(t) \propto \begin{cases} e^{-t/\tau_{(\text{main})}} & \text{for } t < t_0 - t_1 \\ e^{-t/\tau_{(\text{main})}} + k \times e^{-t/\tau_{(\text{burst})}} & \text{for } t \geq t_0 - t_1, \end{cases} \tag{1.7}$$

where τ_{main} and τ_{burst} are the e-folding times for the main stellar population and the burst respectively. k is the strength of the recent variation of the SFR. t_0 and t_1 are the times of old star formation, and the recent burst respectively. Following this form, which is used widely in the literature (e.g., Boquien et al., 2019; Aufort et al., 2020; Donevski et al., 2020; Hamed et al., 2021), one can assume different models of SFHs. For example, a delayed SFH model (defined in section 1.1.1) is when the majority of stars are assumed to be formed in the very early stage of a galaxy's life, followed by a rapid decrease in SFR (in this case, $\tau_{(\text{burst})} = 0$ in equation 1.7). A delayed SFH coupled with a recent burst will add a recent enhancement in the SFR by assuming $\tau_{(\text{burst})} > 0$, reproducing a starburst or an increase in the recent SFR. While a constant SFH is modeled by assuming that a galaxy is forming stars at the same rate since its formation until now (can be achieved with $\tau_{(\text{burst})} = 0$, and a very large $\tau_{(\text{main})}$, e.g., older than the age of the Universe). Figure 1.10 shows the comparison in derived stellar masses of a sample of galaxies using different SFH models. A large difference in $M_\star$ is obtained when using a constant SFH and a delayed one.

1.3.2 Star formation rate

Another crucial measurement in the context of galaxy evolution is the SFR. It is the most important baryonic event in galaxies, since stellar evolution is required in order to form the building blocks of galaxies. Measuring the SFR is challenging, and in this section, I will present some of the most important and very different estimations of this quantity.

In order for a star to be formed, the process begins with a cloud of gas that is mostly molecular hydrogen (H_2) collapsing. As a result, it is reasonable to assume that there is a
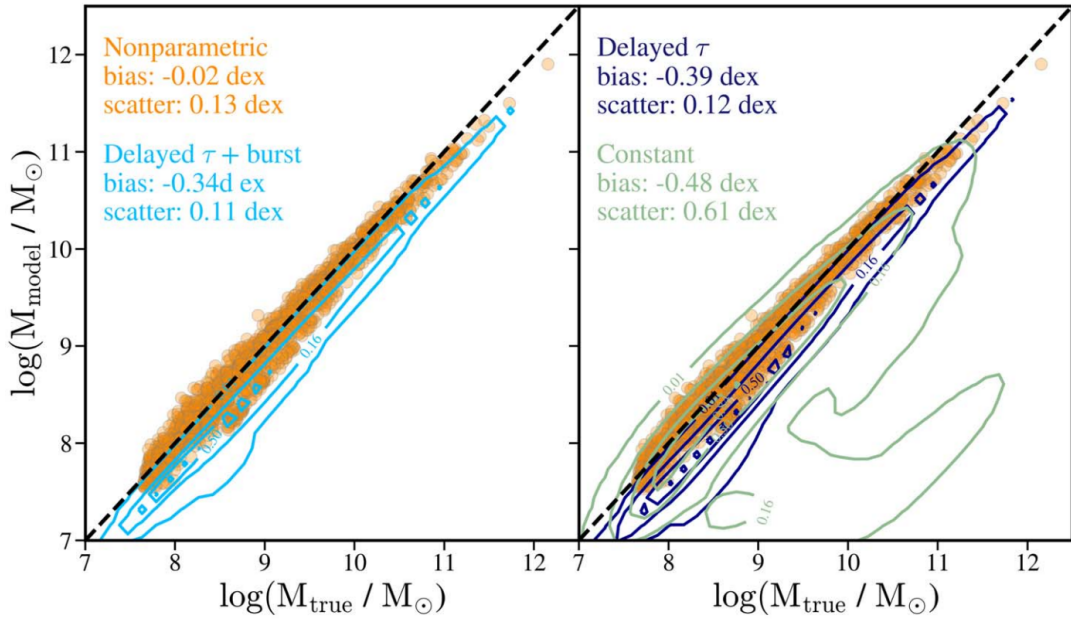
FIGURE 1.10: Comparison between different SFHs in deriving stellar masses of a sample of simulated galaxies with known (true) stellar masses. From Lower et al. (2020).

strong connection between the density of molecular gas and the SFR (Schmidt, 1959; Kennicutt, 1998). The relation between the SFR and the H_2 gas surface density is usually referred to as the Schmidt-Kennicutt law. This correlation is shown in Figure 1.11.

Unfortunately, detecting H_2 is not straight-forward[1]. But astrophysicists rely on molecular tracers for the H_2 molecule density, such as the CO emission[2] whose studied abundance with respect to H_2 allows for an estimation of the molecular gas in galaxies (e.g., Glover et al., 2011; Garilli et al., 2014; Clark et al., 2015). Figure 1.11 shows correlations between the CO emission of different J transitions and the IR luminosities of galaxies at high redshift. The IR luminosity is indicative of the SFR (Kennicutt, 1998).

Another indicator of the SFR is the H_α since its origins are the massive short-lived stars, with the mean age of the stellar emission contribution to H_α emission are < 10 Myr (Hao et al., 2011; Murphy et al., 2011). Some of the other molecular tracers of the SFR, when available, are H_β (Kennicutt, 1998), $[O\,II]$ (Kennicutt, 1998; Rosa-González et al., 2002; Gilbank et al., 2010), and $[O\,III]$ (Villa-Vélez et al., 2021).

One can also estimate the SFR in galaxies using calibrators of photometric bands, such as from the UV bands (Salim et al., 2007; Davies et al., 2016; Brown et al., 2017), and from the IR bands (Kennicutt, 1998; Zhu et al., 2008; Rieke et al., 2009). A systematic study of these SFR calibrators was reported in Figueira et al. (2022).

Another very commonly used method to estimate the SFR of a galaxy is through the SED fitting (e.g., Burgarella et al., 2005; Noll et al., 2009; Boquien et al., 2019). The power of this

---

[1]H_2 lacks a permanent dipole moment, and the selection rules are limited to $\Delta J = 0, \pm 2$. As a result, the first transition that corresponds to the lowest energy is $J = 2 \longrightarrow 0$, which necessitates an excitation potential of roughly 510 Kelvins. However, since star-forming regions are quite cold (of the order of a few tens of Kelvins), H_2 in star-forming regions is virtually undetectable.

[2]The first excitation potential of the CO molecule is of the order of few tens of Kelvins.
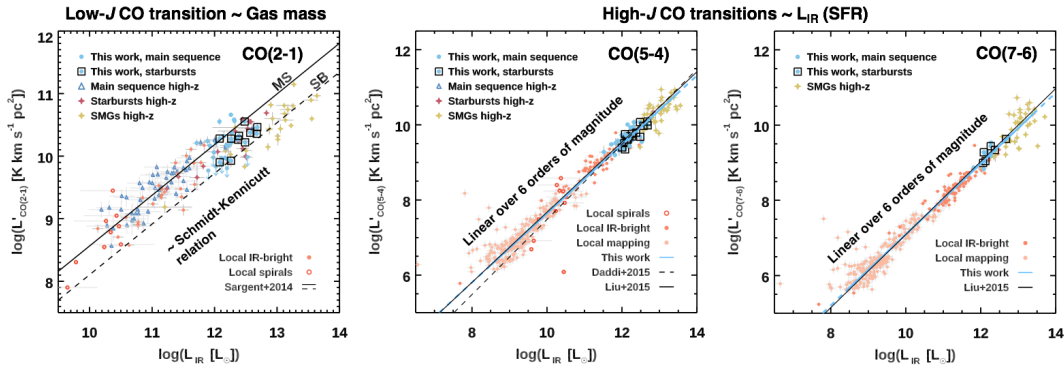
FIGURE 1.11: Correlation between CO luminosity and IR luminosity from Valentino et al. (2020). The left panel shows the low *J* transitions CO (2-1), correlating to the IR luminosities and indicative of the gas mass of galaxies. The center and right panels show higher *J* transitions of CO (5-4) and (7-6) respectively, versus the IR luminosities.

method is the ability to combine different photometric observations in order to estimate the direct SFR and the SFR hidden by dust. In fact, the majority of the SFR is hidden by dust up to at least $z \sim 2$ (Takeuchi et al., 2005; Gruppioni et al., 2015). This renders the composite SFR indicators highly important in estimating this physical quantity. For example, a galaxy at $z = 2$ with UV-IR detections, will be modeled by assuming a stellar population model with a specific SFH, then these stars will be attenuated by interstellar dust. This deals with the UV-near IR part of the spectrum. Additionally, using IR dust emission templates one can fit the IR fluxes of this galaxy, and by doing so, the hidden SFR is estimated (Boquien et al., 2019). Additionally to the instantaneous SFR, the SFR over the past epochs of bursts or quenches[3] can also be estimated, however, this estimation is sensitive towards the assumed SFH (Ciesla et al., 2018).

1.3.3 Dust properties

Effects of interstellar dust span across a very wide wavelength domain. Therefore, dust has intensive (e.g., temperature) and extensive (e.g., mass) properties. Here I will provide a summary of the most important observables of dust in galaxies. To measure dust luminosity, the simplest way is to integrate the IR luminosity, which is typically done between 8 μm and 1000 μm (Schreiber et al., 2018b; Boquien et al., 2019). Dust emission libraries should be assumed in order to best describe dust emission. These libraries are based on observations and theoretical assumptions (e.g., Dale et al., 2002; Draine et al., 2007, 2014). Another important dust observable is its temperature, since it gives hints about dust grain types and dust distribution in the ISM. To derive the average dust temperature of a galaxy, it is sufficient to know the wavelength at which dust emission peaks. This is done by assuming a modified blackbody as a representation of dust emission (as in e.g., Casey, 2012; Casey et al., 2014; Schreiber et al., 2018b).

Dust mass is a more delicate quantity to estimate, as it requires assumptions on grain compositions. To estimate the dust mass, one can start by calculating the IR luminosity (8-1000 μm), and relate it to the dust mass by assuming a dust emission model (e.g., Dale et al., 2002; Draine et al., 2014; Schreiber et al., 2018b). Most of the models assume that the dust grains are in thermal equilibrium with the radiation field of the young stars. Dust emission

---

[3]A quenched galaxy is a galaxy that is no longer actively forming new stars.

models calculate the emission spectrum of the dust as a function of the dust temperature, the grain size distribution, and the dust composition. Fitting these models to the observed IR photometry allows one to obtain the dust mass of a given galaxy. Additionally, several calibrations exist in the literature in order to estimate dust mass. Such methods include prior knowledge of the gas mass and metallicity (Magdis et al., 2012), or assuming cold and warm dust components to the observed flux (Dunne et al., 2001).

All of the aforementioned observables depend on the assumed dust models, with the underlying assumptions of the type of grains and their sizes. The quality of the IR detections, especially at high redshift, allows for a better estimation of these properties.

1.4   Physical observables in the context of galaxy evolution

The physical observables discussed in previous sections - such as stellar mass, SFR, dust mass, and gas content - are all intimately connected in the context of galaxy evolution. The interplay between these properties determines the rate at which galaxies grow and evolve over cosmic time. For example, the SFR is directly related to the amount of gas available for star formation, while the dust content influences the efficiency of star formation by shielding gas from UV radiation and enhancing cooling. The stellar mass of a galaxy reflects its history of star formation and chemical enrichment, while the metallicity provides clues about the sources of chemical enrichment. Together, these properties paint a picture of a galaxy's past and present, and can help to predict its future evolution. By studying these physical properties and their interrelationships, we can better understand the processes that shape the diversity of galaxies we observe in the Universe today.
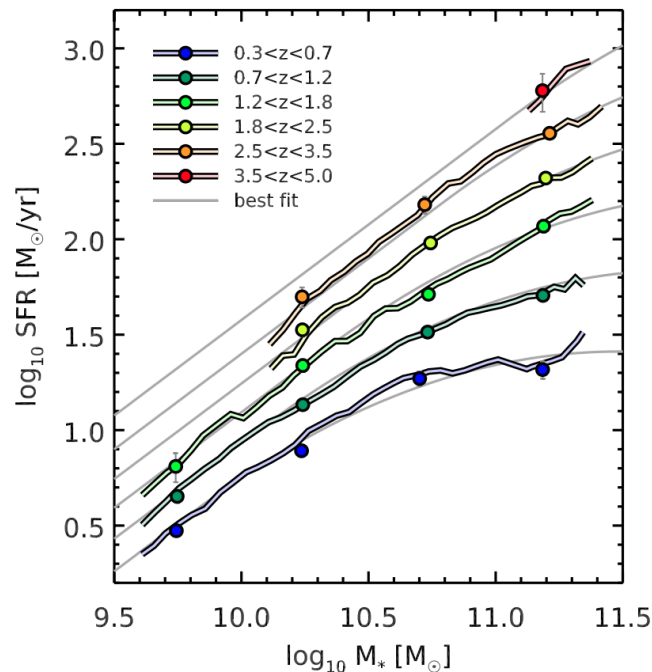
FIGURE 1.12: Evolution of the main sequence of star-forming galaxies with redshift. The colors represent different redshift ranges. From Schreiber et al. (2015).

Observationally, SFRs of most galaxies seem to follow a tight correlation with their stellar masses. This is typically referred to as the main sequence of star-forming galaxies (e.g.,

Daddi et al., 2007; Noeske et al., 2007; Rodighiero et al., 2011; Schreiber et al., 2015), as shown in Figure 1.12. Galaxies can generally be classified into three types based on their SFRs relative to their stellar masses: main sequence or normal star-forming galaxies, starburst galaxies with very high SFRs compared to their stellar masses, and passive or dead galaxies with low to no star formation. At higher redshift, galaxies formed stars at a higher rate for a given mass compared to today's galaxies, translating into an increasing main sequence. This trend can be attributed to the higher gas fractions of galaxies at high redshifts, which may result in increased SFRs (Tacconi et al., 2010). Additional contributors to the increased SFRs at high redshift are the higher abundance of dust (Ferrara et al., 2016), which facilitates the cooling of gas clouds. Higher galaxy merging rates are also observed in the early Universe, which encouraged gas inflows and mass assembly (Perret et al., 2014).

A fundamental empirical relation also correlates the stellar mass of galaxies with their metallicities[4]. This is referred to as the mass-metallicity relation (MZR) (e.g., Gallazzi et al., 2006; Panter et al., 2008; Zahid et al., 2017). The physical interpretation of the MZR is that galaxies with higher stellar masses have higher metallicities because they have been able to retain and enrich their gas reservoirs more efficiently than lower mass galaxies. This enrichment is thought to occur through a combination of in-situ star formation and gas accretion from the intergalactic medium (Sánchez Almeida et al., 2014). At the same time, feedback processes such as supernova explosions, galactic winds (Hopkins et al., 2012), and AGN activity can expel gas from galaxies (Matsuoka, K. et al., 2018), reducing their metallicity and slowing down their star formation. This relation is portrayed in Figure 1.13.
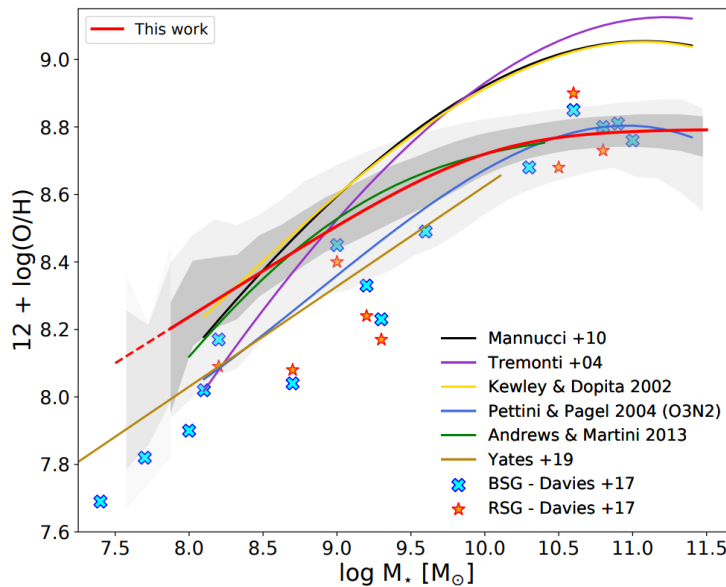
FIGURE 1.13: The stellar mass-metallicity relation from Curti et al. (2020). Gas-phase metallicity is denoted by 12+log(O/H). Different fits represent the fits from different samples studied in the literature. The references to these fits are given in the legend.

Dust mass is also found to be correlated with the stellar mass of galaxies at low redshift (Beeston et al., 2018) and at high redshift (Pantoni et al., 2019). The stellar-to-dust masses relation is thought to arise due to a combination of factors related to galaxy evolution. Dust is produced in the ISM by the same processes that produce heavy elements, such as supernovae

---

[4]Stellar metallicities and gas-phase metallicities both correlate with the stellar masses.

and asymptotic giant branch stars (Michałowski, 2015; Leśniewska et al., 2019), which are more prevalent in higher mass galaxies (Li et al., 2019b). Additionally, higher mass galaxies are expected to have higher gas fractions, and hence more raw material from which dust can form. A correlation between the dust mass and the stellar mass is shown in Figure 1.14. The dust-to-stellar mass ratio, however, is not constant across redshift (Béthermin et al., 2015; Donevski et al., 2020). This ratio can be expressed as in Béthermin et al. (2015):

$$\frac{M_{dust}}{M_\star} \propto \frac{Z \times M_{gas}}{M_\star}, \tag{1.8}$$

where Z is gas metallicity and M_{gas} is the mass of the molecular gas. The dust-to-stellar mass ratio is influenced by two opposing factors; the increasing SFR at higher redshifts and the decreasing Z (Béthermin et al., 2015).
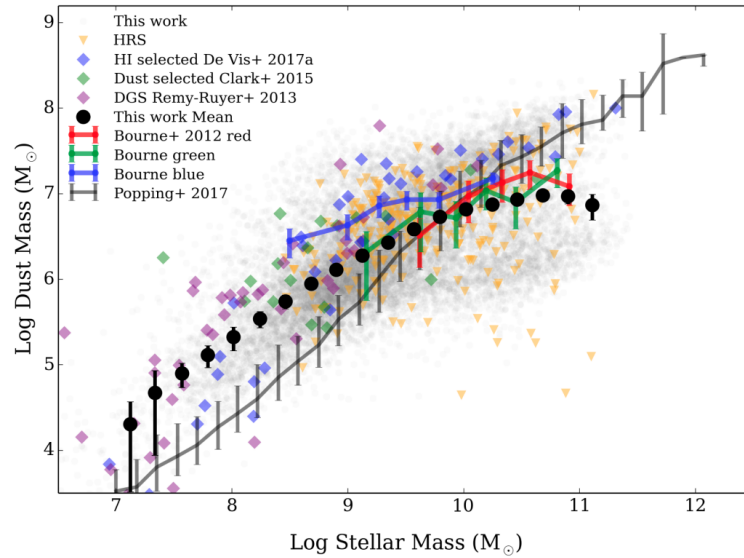
FIGURE 1.14: The dust mass to stellar mass ratio for galaxies in the local Universe from Beeston et al. (2018). The various fitted data represent the samples from the literature, which are denoted in the legend.

In the ISM, dust is a key player that affects galaxy evolution through cosmic time. SFR is found to be more attenuated in the younger Universe, therefore its recovery necessitates an understanding of dust attenuation. Improved methods for estimating dust content and correcting for its effects on observations will continue to be a major focus of research in the extragalactic astrophysics field. Our view of galaxy evolution is distorted by interstellar dust, as can be seen in Figure 1.15. The SFR density peaks at $z \sim 2$ (Hopkins et al., 2006; Madau et al., 2014), an epoch often referred to as the cosmic noon. The present evaluations of the SFR density at redshifts higher than 4 are affected by limited data (compared to lower redshifts) and a greater uncertainty. However, we live in an era of large surveys and powerful instruments such as the JWST and LSST, that will allow us to extend our view to previously unvisited redshifts (e.g., Adams et al., 2023). Measuring the SFR from the UV bands of high redshift galaxies requires the correction for dust attenuation, as no such correction, will strongly underestimate the SFR and hence impact our understanding of the evolution of galaxies.
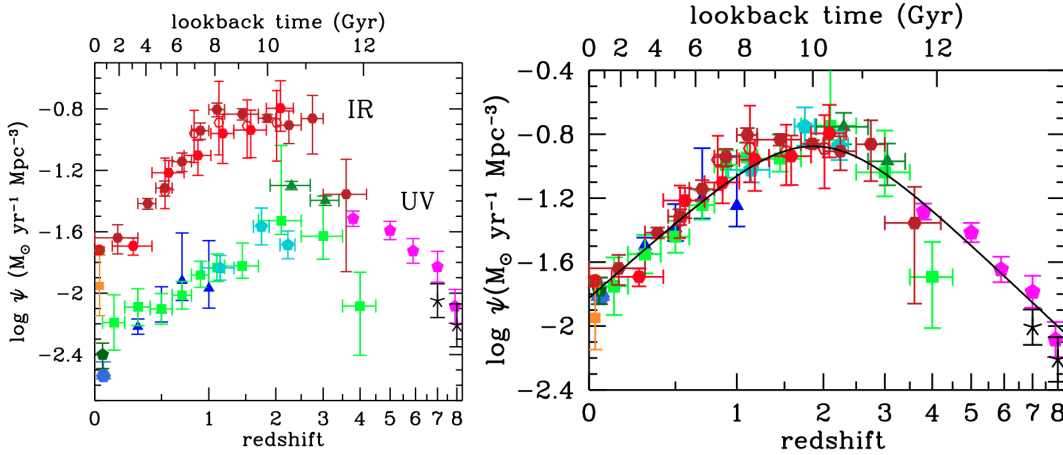
FIGURE 1.15: *Left panel:* Cosmic SFR density derived from IR and UV, uncorrected for dust attenuation in the case of UV. *Right panel:* Cosmic SFR density, corrected for dust attenuation. Both Figures are from Madau et al. (2014).

1.5 Challenges in understanding dust attenuation in galaxies

Despite the advances in modern astronomy, the dust attenuation problem remains a major challenge in extragalactic astrophysics. A big challenge is a degeneracy between dust attenuation and other galaxy properties, such as metallicity and age (e.g., Pozzetti et al., 2000; Papovich et al., 2001; Scoville et al., 2015; Li et al., 2020; Qin et al., 2022). Because dust attenuation affects the observed fluxes of different filters in different ways, it can be difficult to disentangle the effects of dust attenuation from other galaxy properties.

Another big remaining uncertainty is the spatial distribution of dust in galaxies. While we have some knowledge of the global dust content of galaxies, we know very little about the distribution of dust within individual galaxies, which can vary significantly from galaxy to galaxy (Draine, 2003b; Guo et al., 2015; Hodge et al., 2016). We also lack a complete understanding of what is the role of dust distribution and dust compactness in affecting attenuation.

Perhaps the biggest problem concerning dust attenuation in galaxies would be its universality. That is, is dust attenuation universal across all types of galaxies and in different epochs of the Universe? Or whether it varies depending on the physical properties of galaxies? Several studies have investigated this question using both observational and theoretical approaches (e.g., Wild et al., 2011; Narayanan et al., 2018; Ferreras et al., 2021). Observational studies have found evidence for variations in the dust attenuation curve with galaxy properties, such as a steeper slope in low-metallicity galaxies (Shivaei et al., 2020). However, we still do not know what governs the curve of dust attenuation, and what role dust and stellar morphology play in this.

Despite these variations in dust attenuation curves (Boquien et al., 2012; Kriek et al., 2013; Buat et al., 2014; Małek et al., 2018; Salim et al., 2018), most of extragalactic astronomers typically use a single and simple functional form to describe attenuation in large samples of galaxies. This represents a major issue in deriving the physical observables of galaxies, especially the stellar masses. In fact, shallow attenuation laws will assume a dimmer older stellar population, increasing the stellar masses of galaxies (e.g., Małek et al., 2018; Buat et al., 2019). The choice of a functional form (e.g., Calzetti et al., 2000; Charlot et al., 2000) to treat dust attenuation in galaxies, strongly affects the observables. This may result

in a distorted view of galaxy evolution, especially since we still lack knowledge of whether the attenuation curve varies with redshift.

These questions are particularly important when studying DSFGs. These objects were a major contributor to the cosmic SFR, and dust is a key ingredient of their ISM, allowing a deeper study of their dust attenuation law variations. An important question is whether the variations in attenuation of DSFGs are the same as observed in normal star-forming galaxies.

In this thesis, I try to answer these questions through three papers that deal exactly with dust attenuation and physical observables of galaxies at different redshift ranges. The thesis is organized as follows:

In Chapter 2, I present Hamed et al. (2021) in which I investigate SFR, dust, gas, and stellar masses in a pair of peculiar galaxies at the cosmic noon ($z \sim 2$). One of these galaxies is an ultra-massive ULIRG, in which dust attenuation plays a big role in its "starburstiness". I also analyze the morphological differences between its dust continuum (detected by ALMA) and the stellar component.

In Chapter 3, I present Hamed et al. (2023), in which I study a large sample of DSFGs detected by ALMA, and investigate the variation of dust attenuation slopes with the star-to-dust compactness in these galaxies.

In Chapter 4, I study the IRX-β dust attenuation relation at a redshift range of ($0.5 < z < 0.8$), usually referred to as intermediate redshift[5], and investigate the potential drivers of dust attenuation in normal star-forming galaxies.

Each Chapter will be followed by a page of take-away points, to facilitate the reading. And at the end of the thesis, I summarize my work in conclusion, and discuss future perspectives.

---

[5]An often unvisited redshift range in studies that deal with dust attenuation. Of course, the local Universe is highly resolved, and high redshift is à la mode, but what is in between is important to grasp the full evolutionary view of galaxies.

Summary of the first chapter

- Interstellar dust absorbs and scatters light, causing reddening and dimming effects that can obscure and alter our observations of galaxies. The impact of dust attenuation on measurements of galaxy properties, such as stellar masses and star formation rate, can be significant.

- Spectral energy distribution is a powerful tool, allowing us to have a panchromatic view of physical mechanisms that govern galaxy evolution. Dust attenuation plays a crucial role in the SED modeling, despite the dust accounting for a negligible amount of the total baryonic mass in the interstellar medium (ISM).

- Different models and assumptions are used to correct for dust attenuation, leading to varying results. Generally, two often used attenuation laws are that of Calzetti et al. (2000) and Charlot et al. (2000). The former is based on observations of nearby starburst galaxies, while the latter is a model developed to explain the observations.

- Although many advances were achieved in the past to link dust attenuation with other physical properties, such as gas metallicity, little is known about the role of the spatial distribution of dust and stars on attenuation in galaxies.

- The main drivers of the IRX-β dust attenuation relation are not fully investigated. Though many literature exists studying this relation at high redshift and in the local Universe, the intermediate redshift ($0.2 \lesssim z \lesssim 1$) is still poorly studied. Investigating this redshift range will allow us to understand the evolutionary paths of the dust attenuation dependencies.

- Dusty star-forming galaxies are believed to be the progenitors of present-day massive elliptical and quiescent galaxies, and are among the most luminous galaxies in the Universe. They are primarily detected in the far-IR regime due to their high dust content, and are thought to contribute significantly to the cosmic SFR density during the cosmic noon.

2

Multiwavelength dissection of a heavily dust-obscured galaxy and its blue companion at z~2

2.1   Abstract

We study a system of two galaxies, Astarte and Adonis, at $z \sim 2$. At this time, the Universe was undergoing the peak of its star formation activity. Astarte is a dusty star-forming galaxy at the massive end of the main sequence (MS), and Adonis is a less massive companion galaxy that is bright in the ultraviolet and has an optical spectroscopic redshift. We investigate whether this ultramassive galaxy is quenching, and whether it has always been on the MS of star-forming galaxies. We used the code CIGALE to model the spectral energy distribution. The code relies on the energetic balance between the ultraviolet and the infrared. We derived some of the key physical properties of Astarte and Adonis, mainly their star formation rates (SFRs), stellar masses, and dust luminosities. We inspected the variation of the physical parameters depending on the assumed dust-attenuation law. We also estimated the molecular gas mass of Astarte from its CO emission, using different αCO and transition ratios ($r31$), and we discuss the implication of the various assumptions on the gas-mass derivation. We find that Astarte exhibits a MS-like star formation activity, and Adonis is undergoing a strong starburst phase. The molecular gas mass of Astarte is far lower than the gas fraction of typical star-forming galaxies at $z = 2$. This low gas content and high SFR result in a depletion time of 0.22±0.07 Gyr, which is slightly shorter than expected for a MS galaxy at this redshift. The CO luminosity relative to the total infrared luminosity suggests a MS-like activity when we assume a galactic conversion factor and a low transition ratio. The SFR of Astarte is on the same order when different attenuation laws are used, unlike its stellar mass, which increases when shallow attenuation laws are used ($\sim 1 \times 10^{11}$ $M_\odot$) assuming a Calzetti relation, versus ($\sim 4 \times 10^{11}$ $M_\odot$) assuming a shallow attenuation law). We discuss these properties and suggest that Astarte might be experiencing a recent decrease in star formation activity and is quenching through the MS following a starburst epoch.

2.2 Introduction

Studying galaxy evolution throughout cosmic time is a key element of modern astrophysics and is crucial for our understanding of the life cycle of the progenitors of passive elliptical galaxies that we observe in the local Universe. Evidence suggests that the star formation rate (SFR) density has peaked around a redshift of $z \approx 2$ (e.g., Hopkins et al., 2006; Madau et al., 2014; Béthermin et al., 2017; Gruppioni et al., 2020), making this epoch (cosmic noon) particularly interesting. Moreover, at cosmic noon, dusty star-forming galaxies (DSFGs) (e.g., Smail et al., 1997; Blain et al., 2002; Weiß et al., 2013b; Casey et al., 2014; Donevski et al., 2020) contributed significantly to the star formation activity of the Universe (e.g., Chapman et al., 2003, 2005). Furthermore, dust-obscured star formation activity plays an important role at higher redshifts (e.g., Takeuchi et al., 2005; Murphy et al., 2011; Béthermin et al., 2015; Bourne et al., 2017; Whitaker et al., 2017). It is therefore crucial to study the massive DSFGs at higher redshift.

The plethora of multiwavelength data, especially the infrared (IR) detections from *Herschel*, played a central role in our understanding of the evolution of DSFGs as a function of redshift. However, there are still controversies regarding how these galaxies build up their stellar masses. These controversies arise from the systematic uncertainties caused by the heavy dust attenuation in this type of object (e.g., Hainline et al., 2011; Michałowski et al., 2012). This is caused by the sensitivity of the stellar mass estimate to the type of star formation history (SFH), the choice of the synthetic stellar population (SSP), and the assumed initial mass function (IMF). The accuracy of the derived stellar masses of DSFGs was also discussed in detail in Casey et al. (2014).

On the other hand, the growing number of Atacama Large Millimeter Array (ALMA) observations in the recent years provides unparalleled help in constraining the evolution of DSFGs. These data allow us to build a comprehensive view of the role of these giant IR-bright sources by tracing their molecular gas and dust content (e.g., Donevski et al., 2020). The wealth of multiwavelength data also contributed to significantly improve the estimation of physical properties that govern such galaxies by modeling their spectral energy distribution (SED, e.g., Burgarella et al., 2005; da Cunha et al., 2008; Noll et al., 2009; Conroy, 2013; Ciesla et al., 2014).

To build an SED, different aspects of a galaxy must be considered, most importantly, the star formation history (SFH), the change of which strongly affects the derived SFR (e.g., Buat et al., 2014; Ciesla et al., 2017), stellar populations of varied ages and metallicities, dust emission with different dust grain sizes and temperatures, nebular and synchrotron emissions, etc. Extinction caused by dust is critically important in any spectrum fitting of a galaxy because it changes the shape of the SED the most by absorbing a significant number of the ultraviolet (UV) photons and thermally reemits them in the IR. This behavior can be modeled by assuming that dust absorbs the shorter wavelength spectrum of galaxies following attenuation laws that are typically described by simple power laws with varying complexities, and it can reproduce the observed extinction in galaxies of different redshifts and types. However, dust attenuation laws are not universal (e.g., Wild et al., 2011; Buat et al., 2018; Małek et al., 2018; Salim et al., 2020). The need of different attenuation recipes is inevitable in order to reproduce the spectra of galaxies of different masses, IR luminosities, and the redshift. This makes it challenging to interpret some of the physical features, especially when different attenuation laws can reproduce a good SED of a galaxy (Buat et al., 2019).

A non-negligible fraction of galaxies exhibits nonalignment and sometimes a total disconnection between the dust continuum and the stellar population (Dunlop et al., 2017; Elbaz et al., 2018). This directly challenges SED fitting techniques that rely on the energetic balance between the UV and the IR because the key assumption for these techniques is that any

physical property derived from one part of the spectrum should be valid for the entire galaxy. Several approaches have been investigated to test the validity of this strategy. Buat et al. (2019) suggested the decoupling of the stellar continuum from the IR emission by modeling their fluxes in addition to comparing the derived parameters such as the SFRs, dust luminosities, and stellar masses with those derived using full SEDs. Statistical samples of such massive and dusty galaxies (e.g., Dunlop et al., 2017; Elbaz et al., 2018; Buat et al., 2019; Donevski et al., 2020) offers an important insight into the evolution of dust and gas mass through cosmic time. However, the nature of these giants is not fully understood.

The interstellar medium (ISM) is the most important element in understanding the physical processes of star formation because it contains the building materials for future stars, most importantly, hydrogen. The hydrogen density was found to be tightly correlated with the SFR, as suggested by Schmidt (1959) and investigated by Kennicutt (1998). This correlation is known as the Schmidt-Kennicutt law, and it takes the gas in its molecular and atomic forms into account, even though molecular gas has the strongest effect. The mass of this gas can be estimated based on the emission of the easily excited CO molecules (e.g., Carilli et al., 2013; Weiß et al., 2013a; Decarli et al., 2019; Riechers et al., 2020). Tracing the molecular gas with CO emission relies entirely on already established abundances in galaxies of the local Universe. Large interferometers such as ALMA offer unique opportunities for detecting these emission lines with unprecedented accuracy. The luminosity of the lines can give an estimate of the molecular hydrogen mass of a galaxy, typically using a conversion factor. On the other hand, conversion factors in high-redshift galaxies are highly debated (see Bolatto et al., 2013 for a comprehensive review).

Nonetheless, an estimate of the molecular gas reservoir of galaxies at the high-mass end of the main sequence (MS) is crucial for characterizing their star formation activity. For instance, Elbaz et al. (2018) showed that some galaxies exhibit a starburst (SB)-like gas depletion timescale although they reside on the MS.

Despite the growing number of detections of these heavily dust-obscured ultramassive objects at high redshift, the progress of SED modeling, and the better comprehension of the high-redshift ISM, we still lack a full picture of how these galaxies form and quench. They might always have steadily formed stars throughout the MS, or they might be former SBs transiting to the red sequence through the MS.

To answer these questions, it is essential to understand how the star formation is fueled by the gas in massive objects, and why this activity ceases. Quenching mechanisms are still not fully understood, and they might be caused by active galactic nuclei (AGN) feedback or outflows (e.g., Cattaneo et al., 2009; Dubois et al., 2013; Combes, 2017) to environmental effects that can lead to gas-stripping (e.g., Coil et al., 2008; Mendez et al., 2011).

Motivated by these questions, we analyze and interpret the multiwavelength observations of a pair of galaxies at z∼2 with the original COSMOS2015 catalog (Laigle et al., 2016 IDs: 647980 and 648299, hereafter Astarte and Adonis). Astarte is an ultramassive ($M_\star > 10^{11} M_\odot$), IR-bright galaxy whose CO emission is serendipitously detected with ALMA. Adonis is a low-mass galaxy bright in near-UV and optical bands.

The structure of this paper is as follows: in Section 2.3 we describe the data of the two galaxies. In Section 2.4.1 we probe the molecular gas of Astarte using its ALMA-detected CO emission line, and in Section 2.4.1 we investigate the morphology of this line compared to multiwavelength detections. In Section 2.4.2 we derive the physical properties of the two galaxies using SED fitting. The discussion and conclusion are presented in Sections 4.7 and 2.6, respectively.

Throughout this paper, we adopt the stellar IMF of Chabrier (2003) and ΛCDM cosmology parameters (WMAP7, Komatsu et al., 2011), $H_0 = 70.4$ km s^{-1} Mpc^{-1}, $\Omega_M = 0.272$, and $\Omega_\Lambda = 0.728$.

2.3 Observations

The system of Astarte and Adonis was initially part of a selection of z~2 galaxies at the high-mass end ($M_\star > 10^{11}$ $M_\odot$) of the MS of star-forming galaxies (e.g., Noeske et al., 2007; Daddi et al., 2010; Rodighiero et al., 2011; Schreiber et al., 2015) detected by *Herschel*/PACS observations of the COSMOS field (PEP survey, Lutz et al., 2011). In the COSMOS2011 catalog from which the system was selected, the system is not deblended even in the optical and near-IR and appears as a single source. This is probably caused by the fact that this early catalog is mainly built using the *i* band, in which Astarte is particularly faint. The zCOSMOS survey (Lilly et al., 2009) measured the spectroscopic redshift at the position of the HST/ACS source from zCOSMOS and found $z_{spec} = 2.140$. In the more recent COSMOS catalog (Laigle et al., 2016), both *z*- and near-IR bands were used to detect and deblend the object. Adonis and Astarte thus have individual flux measurements in the optical bands of Subaru, the near-IR bands of VISTA, and the mid-IR with *Spitzer*/IRAC. Astarte is detected at 250 and 350 μm with *Herschel*/SPIRE using a 24 μm prior (Oliver et al., 2012). The deblending, coupled with the far-IR detection of Astarte, results in a low-mass low-SFR object (SFR = 37 $M_\odot$ yr^{-1} with a stellar mass of 9.46×10^9 $M_\odot$), and a dust-obscured ultramassive object (SFR = 131 $M_\odot$ yr^{-1} with a stellar mass of 1.41×10^{11} $M_\odot$), as initially estimated using LePhare (Arnouts et al., 2011).

Astarte and Adonis were observed by ALMA as part of a program (2013.1.00914.S, PI: Béthermin) targeting a pilot sample of four massive z~2 main-sequence galaxies in band-7 continuum and their CO emission. The goal was to measure their gas and dust content and to compare their short-wavelength morphology with their CO and continuum morphologies.

2.3.1 Near-UV to IR observations

The near-UV (rest-frame far-UV) detections of our two galaxies are provided by the Canada France Hawaii Telescope (CFHT) in the *u* band. Visible and near-IR detections (rest-frame near-UV) are obtained via the broad band Suprime-Cam of Subaru in the *B, V, r, i$^+$* bands and the mid-IR data (rest-frame near-IR) are from the IRAC camera of *Spitzer*. The IR-bright Astarte has a MIPS detection at 24 μm with a signal-to-noise ratio (hereafter S/N) > 20 and is very bright (S/N ~ 20) in IR detections of *Herschel,* where the beam size is large. The 100 μm observation from PACS did not detect the two galaxies, but provided an upper limit, which is taken into account in the SED fitting because it constrains the far-IR part of the spectrum.

The radio continuum of Astarte was tentatively detected with the Karl G. Jansky Very Large Array (VLA) in the S band at ν =3 GHz (Smolčić et al. (2017). This tentative detection was not included in the initial catalog of Smolčić et al. (2017) because it falls just below their detection threshold of 5σ (S/N=4.3). Adonis has not been detected with the VLA at 3 GHz. We thus estimated a 3σ upper limit from the standard deviation in the cutout image around our two sources. The beam width of the VLA detection is 0.75ʺ, and the continuum is shown in Figure 2.1.

The Jin et al. (2018) catalog provides the JCMT fluxes at 850μm for both our galaxies (2440±2519 μJy for Astarte and 3910±2516 μJy for Adonis). We refrain from using these highly deblended fluxes because of the high uncertainties, which are probably caused by the degeneracies in the deblending of this close pair and because most of the flux is unexpectedly attributed to the smaller and less IR-bright Adonis. Table 3.1 presents a summary of the available photometric data from different instruments of the two galaxies.
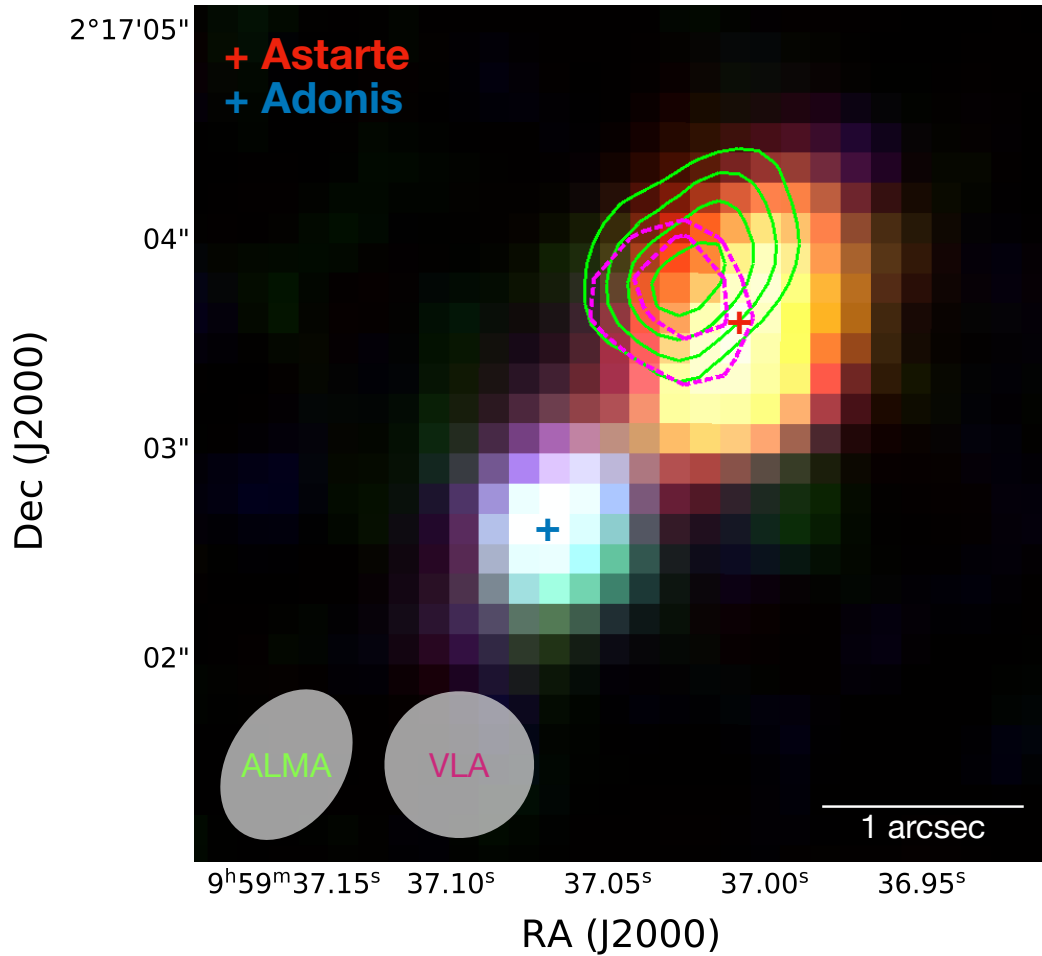
FIGURE 2.1: Integrated flux of ALMA-detected CO emission (green contours) along with the VLA-detected radio continuum at 3 GHz (magenta contours) in the RGB image (VISTA Ks, H, and J) of Astarte and Adonis. The beam size of ALMA is 0.78" × 0.50" (lower left beam). The beam FWHM of VLA is 0.75". The outermost contour of the CO integrated flux (green) is at 2σ significance. The subsequent contours are in steps of 1σ, and the innermost contour shows 5σ. The magenta contours show 2 and 3σ significance. The blue cross is centered on Adonis, and the red cross is centered on Astarte.

2.3.2 ALMA observation

Astarte was observed at 2.7 mm with ALMA (band 3) with a time on source of 45 minutes using 32 antennas on September 5, 2015, cycle-2 (P.I. M.Béthermin). We used the Common Astronomy Software Applications package and pipeline (CASA) v5.4[1] (McMullin et al., 2007) to flag and reduce the visibility data. The deconvolution was performed with the CLEAN algorithm using natural weighting for an optimal S/N. The multifrequency synthesis mode of the line-free channels showed an insignificant continuum emission of the spectrum, therefore we did not need to subtract it. In the deconvolution process, the cell size was set to 0.1″. The achieved synthesized beam size is 0.78″ × 0.56″, the velocity resolution of the cube is 21.36 km s^{-1}, and the rms is 0.47 mJy beam^{-1} km s^{-1} per channel.

[1] https://casa.nrao.edu/

Telescope/	Filter	λ	Astarte	Adonis
COSMOS15 ID			647980	648299
redshift			$z_{phot} = 2.153$	$z_{spec} = 2.140$
Telescope/	Filter	λ	S_ν	S_ν
Instrument		(μm)	(μJy)	(μJy)
CFHT/	u	0.383	0.104 ± 0.032	0.492 ± 0.032
MegaCam				
Subaru/	B	0.446	0.127 ± 0.018	0.596 ± 0.032
Suprime-Cam	V	0.548	0.252 ± 0.033	0.938 ± 0.049
	r	0.629	0.246 ± 0.029	0.904 ± 0.041
	i^+	0.768	0.331 ± 0.035	0.973 ± 0.042
	z^{++}	0.910	0.719 ± 0.062	1.329 ± 0.063
VISTA/	Y	1.02	0.836 ± 0.155	1.519 ± 0.162
VIRCam	J	1.25	2.691 ± 0.175	2.682 ± 0.181
	H	1.65	4.234 ± 0.241	3.243 ± 0.254
	Ks	2.15	9.536 ± 0.351	4.776 ± 0.362
Spitzer	IRAC1	3.6	18.60 ± 0.07	3.70 ± 0.10
	IRAC2	4.5	25.10 ± 0.10	2.80 ± 0.13
	IRAC3	5.8	25.10 ± 2.00	3.60 ± 2.60
	IRAC4	8.0	15.30 ± 3.30	-
Spitzer	MIPS1	24	351 ± 17	
Herschel	PACS	100	< 6734	
Herschel	SPIRE	250	17792 ± 744	-
	SPIRE	350	16058 ± 1026	-
VLA	S	1.3×10^5	9.9 ± 2.3	< 7.3

TABLE 2.1: Summary of the data of the two sources observed through the different instruments. S_ν is the flux in (μJy). λ is the center of the specific filter band.

2.4 Results

2.4.1 Probing the molecular gas of Astarte

In the data cube we find only one significant line and no significant continuum source in the field of view. The line extraction procedure along with the derivation of the luminosity and the gas mass are described in the following subsections.

Line extraction

The ALMA-detected emission line of Astarte corresponds to the CO(3-2), with a peak at an observed frequency of $\nu_{obs} = 109.65$ GHz, implying $z_{CO(3-2)} = 2.154$, which agrees with the photometric redshift $z_{phot,Astarte} = 2.153^{+0.051}_{-0.058}$ Laigle et al. (2016). This confirms Astarte as the origin of the detected-CO emission. We do not detect Astarte in the continuum and measured a 3σ upper limit from the map of 0.117 mJy. The expected flux densities from the SED modeling discussed in Sect.2.4.2 are 0.007 mJy and 0.049 mJy for Adonis and Astarte, respectively. It is thus not surprising that none of our two sources are detected. The flux uncertainty was determined by deriving the standard deviation in the source-free pixels in the map that was not corrected for the primary beam because it has similar noise levels in the emission-free pixels (the noise in the central region is $\sim 2\%$ higher than in the outermost

region of the map). The achieved S/N is 5.2 for the brightest channel of the CO(3-2) of Astarte. The emission line was extracted by fitting a Gaussian to the profile. The goodness of the Gaussian fit was verified with a χ^2 test. Its properties are summarized in Figure 2.2 along with the redshifted CO(3-2) line. The full width at half maximum (FWHM) of the Gaussian is found to be 152.74±33.21 km s^{-1}. The spectroscopic redshift of the system at
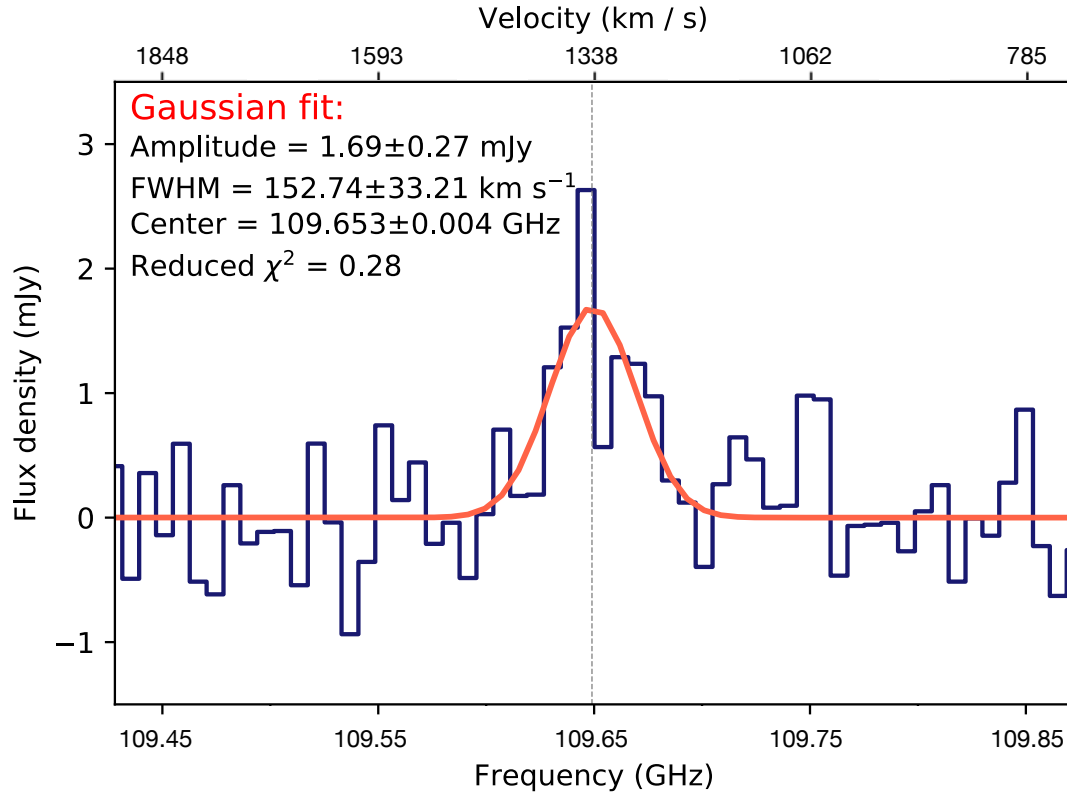
FIGURE 2.2: Spectral profile of Astarte with the redshifted CO(3→2) line (dashed vertical gray line) and the Gaussian fit (red) with its properties.

the position of HST detection found by by the zCOSMOS survey Lilly et al. (2009) is $z_{spec} = 2.140$. This z_{spec} corresponds to that of Adonis because only this UV-bright galaxy is detected with HST/ACS. When the redshift difference of Astarte and Adonis is taken into account, the corresponding radial velocity difference ΔV is $1335\,km\,s^{-1}$. This velocity difference is greater than what is found in interacting pairs of galaxies, which is typically $\Delta V < 350\,km\,s^{-1}$ (Lambas et al., 2003; Alonso et al., 2004). Outflows and absorption in the UV lines could account for few hundred km s^{-1} (Cassata et al., 2020), or a division of the Hubble flow and peculiar motions, which could account for a significant velocity contribution if it is along the line of sight. Therefore this does not rule out a possible interaction between Astarte and Adonis.

Line-integrated flux and luminosity

The intensity is calculated by integrating over the Gaussian fit of the line, which is then converted into the apparent line luminosity (L') using the expression from Solomon et al., 1997, which expresses L' with the integrated source brightness temperature in units of $K\,km\,s^{-1}\,pc^2$,

$$L'_{line} = 3.25 \times 10^7 \times I \times \frac{D_L^2}{(1+z)^3 \nu_{obs}^2}, \qquad (2.1)$$

where D_L is the luminosity distance in Mpc, I is the intensity in Jy km/s, and ν_{obs} is the observed frequency in GHz. As a consistency test, we also estimated the integrated flux of the line using the moment-zero map, which was obtained by summing the channels in which the emission line is detected. The line flux is measured in the moment-zero map using a 2D Gaussian fit of the source. As shown in Béthermin et al. (2020), there is no significant difference between this method and a fit in the uv plane for faint compact sources observed by ALMA. The resulting flux densities of the two methods are presented in Table 4.2. There is $1.2\,\sigma$ significant difference between the intensities derived by each methods. The spectrum is extracted at a single point assuming a point source, while the 2D fit can recover the flux from an extended source. This small difference in flux suggests that our source was marginally resolved. Hereafter, we use the flux from the moment-zero map, which takes this into account. However, we cannot formally exclude another faint and diffuse component at larger scale considering the depth of our data. Figure 2.1 shows the flux-integrated moment-zero map of Astarte represented by confidence levels contours. The size of the CO disk is $\sim 74\,kpc$.

Peak flux density (mJy)	$I^{spec}_{CO(3-2)}$ (Jy km s^{-1})	$I^{mom}_{CO(3-2)}$	$L'_{CO(3-2)}$ (10^9 K km s^{-1} pc^2)
1.690 ± 0.277	0.251 ± 0.062	0.328 ± 0.047	8.508 ± 1.219

TABLE 2.2: Summary of the CO(3-2) emission line properties of Astarte. $I^{spec}_{CO(3-2)}$ is achieved by integrating over the Gaussian of the emission line. $I^{mom}_{CO(3-2)}$ is the intensity derived from the moment-zero map.

Deriving the molecular gas mass

To derive the total mass of the molecular gas in a galaxy, we assumed that the H$_2$ mass is proportional to the CO(1-0) line luminosity, which is the commonly used tracer of the cold star-forming molecular clouds because only a small excitation potential is required. The H$_2$ mass can be derived using a conversion factor α_{CO} (e.g., Downes et al., 2003; Greve et al., 2005; Tacconi et al., 2006; Bothwell et al., 2013a; Carilli et al., 2013),

$$M_{H_2} = \alpha_{CO}\, L'_{CO(1-0)}, \tag{2.2}$$

where M$_{H_2}$ is the mass of the molecular hydrogen in $M_\odot$, α_{CO} is the conversion factor, and $L'_{CO(1-0)}$ is the line luminosity in $K\,km\,s^{-1}\,pc^2$. The practice of deriving the H$_2$ mass with this method is very common, especially for galaxies at high redshifts, for which information and spatial resolution is often limited. Our CO(3-2) line luminosity has to be converted into CO(1-0) luminosity using a luminosity line ratio $r_{31} = L'_{CO(3-2)}/L'_{CO(1-0)}$. We used $r_{31} = 0.42 \pm 0.07$, which is the average ratio found for $z = 1.5$ SFGs by Daddi et al. (2015). This resulted in

$$L'_{CO(1-0)} = (2.03 \pm 0.59) \times 10^{10}\, K\,km\,s^{-1}\,pc^2.$$

To convert this luminosity into hydrogen mass, we used two conversion factors: $\alpha_{CO} = 0.8$, and a galactic conversion factor of $\alpha_{CO} = 4.36$. The first recovered the molecular gas mass in SBs and submillimeter galaxies, where the gas is efficiently heated by dust. The galactic conversion factor is suitable for normal MS galaxies (Downes et al., 1998; Bolatto et al., 2013; Carilli et al., 2013). For $\alpha_{CO} = 0.8$, the mass of the molecular hydrogen is $M_{H_2(\alpha=0.8)} = (1.62 \pm 0.47) \times 10^{10}\, M_\odot$. $\alpha_{CO} = 4.36$ results in $M_{H_2} = (8.85 \pm 2.57) \times 10^{10}\, M_\odot$, which is a five times larger gas reservoir than we derived with $\alpha_{CO} = 0.8$.

Dynamical mass

With the velocity FWHM of the CO(3-2) line, we used the method described in Bothwell et al. (2013b) to estimate the dynamical mass of Astarte. Assuming that a rotating disk is the origin of the detected line, the dynamical mass can be written as in Neri et al. (2003),

$$M_{dyn} \; (M_\odot) = 4 \times 10^4 \; \Delta V^2 \; R / sin^2(i), \tag{2.3}$$

where ΔV is the FWHM of the line velocity, i is the inclination angle of the disk, and R is the radius of the disk in kiloparsec. For a random inclination of $\langle i \rangle = 57.3°$ (Law et al., 2009), the dynamical mass is found to be $(1.11 \pm 0.23) \times 10^{11}$ M$_\odot$. The ratio of gas mass to dynamical mass for a galactic conversion factor is therefore $M_{H_2}/M_{dyn} = 0.76 \pm 0.33$. For $\alpha_{CO} = 0.8$, $M_{H_2}/M_{dyn} = 0.15 \pm 0.07$. The hydrogen mass derived assuming a galactic conversion factor is able to trace the dynamical mass of Astarte, despite the relatively low FWHM of the CO line, as it is for similar FWHM values in Bothwell et al. (2013a).

CO emission morphology

We investigated the morphology of the CO(3-2) emission line of Astarte in relation to other wavelength detections of the system to closely study the association of the CO component with the UV, optical, and IR components, as shown in Figure 2.3. HST's observation in the I band (rest-frame mid-UV) do not show Astarte because it is heavily obscured by dust. However, the young stellar population of the less-dusty Adonis is visible in the HST I band and is bright in the u-band detection of CFHT (rest-frame far-UV) and in the J band of VISTA (rest-frame near-UV). In the Ks bands of CFHT and VISTA, which correspond to rest-frame visible light, Adonis becomes less bright and is very faint at higher wavelength observations of ALMA and VLA.

The dusty Astarte is not visible in the u band of CFHT (rest-frame far-UV). It is detected in the Ks bands of VISTA and CFHT, however, showing a bright stellar population in the visible rest-frame wavelengths. A spatial offset (of $\sim 0.39''$) is visible between the ALMA-detected CO emission and the emission of the stellar population (observed in the Ks bands) of Astarte. Faisst et al. (2020) found an average offset between the COSMOS2015 catalog and the Gaia reference frame of $\Delta(RA) = -63.9^{+70.7}_{-60.2}$ milliarcsec and $\Delta(Dec) = -1.4^{+80.4}_{-67.3}$ milliarcsec. This systematic offset cannot explain the visible offset between the CO emission and the rest-frame optical counterparts of Astarte. Moreover, we show that the continuum detected by the VLA at 3 GHz of Astarte and its CO emission detected by ALMA are aligned, eliminating the possibility of a systematic error due to the synthesized beam size of ALMA.

Although the original spectroscopic redshift of 2.140 (for both sources) found by zCOS-MOS (Lilly et al., 2009) was derived from the visible range of the HST observation, in which Astarte is not observed, ALMA offers a spectroscopic redshift for the latter ($z_{ALMA} = 2.154$). This shows the importance of long-wavelength detections especially for dust-obscured galaxies where the UV to near-IR emission is heavily attenuated (Schreiber et al., 2018a; Wang et al., 2019).

2.4.2 SFRs, stellar masses, and dust luminosities

SED modeling

We used the SED modeling code CIGALE[2] (Boquien et al., 2019) to derive the physical properties of our sources. The code allows modeling galaxy SED from the UV to the radio

---

[2] http://cigale.lam.fr
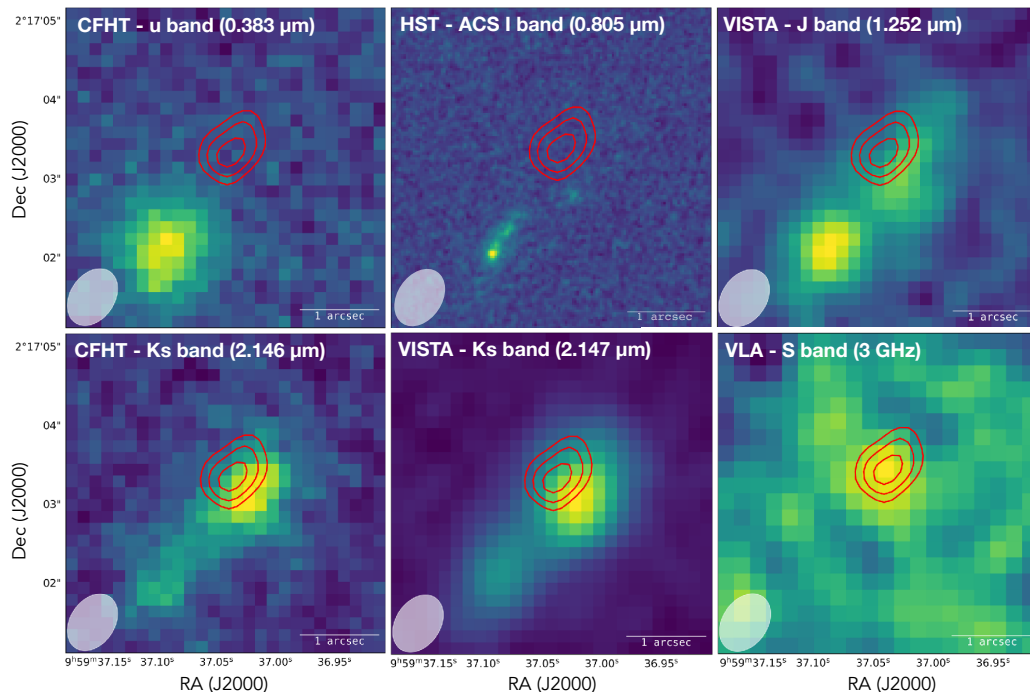
FIGURE 2.3: ALMA-detected CO(3-2) emission line contour map (red contours) of Astarte overlaid on detections from different telescopes and instruments at different bands as specified in every panel. From upper left to lower right: CFHT U band at 0.383 μm. HST I band at 0.805 μm. VISTA J band at 1.252 μm. CFHT Ks band at 2.146 μm. VISTA Ks band at 2.147 μm and for the VLA detection at 3GHz. The outermost contour is 3σ, and the subsequent contours are in steps of 1σ with red innermost contour showing 5σ. The beam size is 0.78"$\times$ 0.50". The white bar shows the 1 arcsecond scale.

wavelengths, taking the energetic balance between the emission absorbed by dust in the UV-visible range and the IR emission into account. CIGALE offers a variety of modules for each physical process a galaxy may undergo. The modules that we used in our SED fitting procedures are described below.

Stellar component

To model the stellar component of Astarte and Adonis, we used the SSP of Bruzual et al. (2003). This stellar library computes the direct stellar contribution to the spectrum (UV to near-IR range) by populating the galaxy with young and old stars of different masses, as well as the required gas mass that will produce such population. This model was developed based on observations of nearby stellar populations, and it describes the various stellar emissions that are expected in encounters within any galaxy. These models depend on the metallicity and the separation age[3]. We used a solar-like metallicity and took nebular emission into account because they contribute to the total SED model from the UV to near-IR.

Different stellar demographics must be modeled with an appropriate SFH in any SED modeling because it is critical to estimate the contribution of the young and old stars to the total flux. An appropriate SFH is key to deriving the SFR of a galaxy because it strongly depends on the assumptions made (Ciesla et al., 2017). CIGALE offers different SFH scenarios that vary from the simple delayed SFH to more complex scenarios containing episodes of bursts or sudden drops in SFRs. We used the SFH proposed by Ciesla et al. (2017), which is

---

[3]Age of the separation between the young and old stellar population.
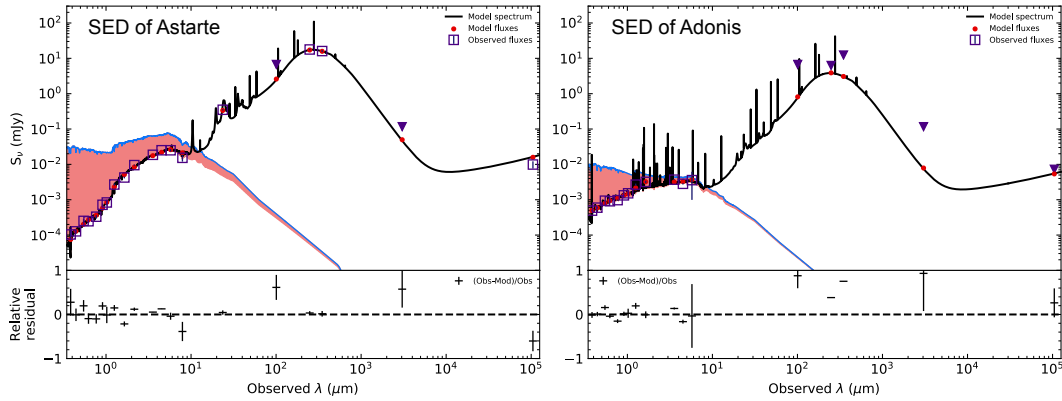
FIGURE 2.4: Best fits of the constructed SEDs of Astarte and Adonis along with their relative residuals. The SED of Astarte (left) is produced using the LF17 attenuation law. The SED of Adonis (right) is produced using the CF00 attenuation law. The best fit is shown in black. The unattenuated stellar emission is shown with the blue line. The filled region shows the difference between the unattenuated and the attenuated stellar emission, absorbed by dust. Red dots are the best-fit values of the observations, which are shown with the purple boxes. Upper limits are shown as purple triangles.

a combination of a smooth delayed buildup of the stellar population to model the long-term SFH of a galaxy, and a recent flexibility in the past few hundred million years to allow for recent and drastic SFR variations (burst or quench). This SFH model has been proven to limit biases by decoupling the estimations of the stellar mass, which are mainly constrained by rest frame near-IR data, from the SFR, which is constrained by UV and IR data (e.g., Ciesla et al., 2016, 2018; Schreiber et al., 2018a,b). This type of SFH was used in the study of high-redshift ($z < 3$) passive galaxies to model their SED (e.g., Merlin et al., 2018; Schreiber et al., 2018a,b). We limited the recent burst or quench episodes to the last 100 Myr of the life of our sources. The recent burst is motivated by the ALMA detection, but it is important to note that this burst makes it difficult to constrain the past SFH. The burst part of the SFH is usually responsible for fitting the UV data, whereas the previous SFH (delayed) is driven by the older stellar population, manifested in the visible part of the SED.

Attenuation laws

Two prominent attenuation laws are those of Calzetti et al. (2000) (hereafter C00) and Charlot et al. (2000) (hereafter CF00). They are widely used in the literature, and along with their alternations, they can describe the behavior of the extinction in the UV to near-IR caused by dust.

C00 and their recipes are at their core equivalent to reducing the short-wavelength flux from a stellar population by an opaque screen, with the opacity being dependent on the total extinction of the stellar emission at the B and V bands.

Another approach is the CF00 power law, which is fundamentally different from that of C00: it attributes a different attenuation to the ISM and to the birth clouds (hereafter BC). This makes the dust more effective at absorbing the UV light because the young stellar emission has to pass through the dust in the BC and the ISM. Stars that are older are only attenuated by the ISM dust. The CF00 approach is slightly more complex and physical than that of C00 for high-redshift ultradusty galaxies, embodying different dust distributions and densities throughout a galaxy.

C00 and CF00 relied for their efficiency of attenuating the stellar population on power laws for their slopes. The power-law slopes for BCs and ISM in CF00 were originally fixed

Parameter		Values
Star formation history Ciesla et al. (2017)		
Stellar age[i]	age_{main}	0.8 - 3.2 Gyr by a bin of 0.2 Gyr
e-folding time[ii]	τ_{main}	0.8, 1, 3, 5, 8 Gyr
Age of burst/quench episode	t_{flex}	5, 10, 50, 100 Myr
SFR ratio after/before	r_{SFR}	10^{-2}, 10^{-1}, 0, 10^{1}, 10^{2}, 10^{3}
Stellar synthesis population (Bruzual et al., 2003)		
Initial mass function	IMF	(Chabrier, 2003)
Metallicity	Z	0.02
Separation age		10 Myr
Dust attenuation laws		
(Calzetti et al., 2000)		
Colour excess of young stars	E(B-V)	0.1 - 1 by a bin of 0.1
Reduction factor[iii]	f_{att}	0.3, 0.5, 0.8, 1.0
(Charlot et al., 2000), (**Lo Faro et al., 2017**)		
V-band attenuation in the ISM	A_V^{ISM}	0.3 - 3 by a bin of 0.1
$Av_V^{ISM} / (A_V^{BC} + A_V^{ISM})$	μ	0.3, 0.5, 0.8, 1
Power law slope of the ISM		-0.7, **-0.48**
Power law slope of the BC		-0.7
Dust emission model (Draine et al., 2014)		
Mass fraction of PAH	q_{PAH}	1.77, 2.50, 3.19
Minimum radiation field	U_{min}	10, 25, 30, 40
Power law slope	α	2
Synchrotron emission		
far-IR/radio correlation coefficient		2.3 - 2.9 by a bin of 0.1
Power law slope slope	$\alpha_{synchrotron}$	0.4 - 0.9 by a bin of 0.1

TABLE 2.3: Input parameters used to fit the SEDs of Astarte and Adonis with CIGALE. (i) The stellar age is the age of the main stellar population. (ii) The e-folding time is the time required for the assembly of the majority of the stellar population. (iii) The reduction factor f_{att} is the color excess in old relative to young stars.

at -0.7 each. The recipe of Lo Faro et al. (2017) (hereafter LF17) of CF00 was tuned by assuming a power law for the slope of the attenuation in the ISM equal to -0.48. This recipe provides a steeper attenuation curve at shorter wavelengths. We used these three attenuation laws and compared their best fits and their effects on deriving the physical properties of our sources.

To assess which attenuation laws to use when different modules can produce good and comparable fits, we employed the Bayesian information criterion (BIC), defined as the $\chi^2 + k \ln n$, where χ^2 is the unreduced goodness of the fit, k is the degree of freedom of the model, and n is the total number of photometric fluxes used in the fit of the galaxy. We then evaluated the preference of a model over another by calculating the difference between their BICs: $\Delta BIC > 2$ translates into a notable difference between the two laws, and the fit with the lowest χ^2 is preferred. This method was used by Ciesla et al. (2018) to choose successful scenarios of SFHs of quenching galaxies, and by Buat et al. (2019) to assess SEDs of $z \sim 2$ ALMA-detected galaxies.

	Attenuation law	χ^2	reduced χ^2	BIC
	C00	43.22	2.12	73.18
Astarte	CF00	18.34	0.97	51.30
	LF17	16.06	0.84	49.01
	C00	16.28	1.10	46.78
Adonis	CF00	10.51	0.70	41.01
	LF17	13.99	0.93	44.49

TABLE 2.4: Comparison between the quality of fits of Astarte and Adonis produced with CIGALE with the three attenuation laws.

Dust emission

To model the dust emission, we used the Draine et al. (2014) IR emission models, which were calibrated using high-resolution observation of the Andromeda galaxy. Draine et al. (2014) considered a variety of dust grains heated by different intensities coming from the stars and the photodissociation regions, and this is an improved version of the previous Draine et al. (2007) model by varying the dust opacity across the radius of a galaxy. This IR model was successful in reproducing dust emissions of millions of *Herschel*-detected galaxies as a part of the HELP project (Małek et al., 2018).

Synchrotron emission

The VLA detection at 3 GHz of Astarte and Adonis allowed us to model the synchrotron emission of our objects, taking a nonthermal power law of the synchrotron spectrum and the ratio of the far-IR/radio correlation into account. The different parameters we used to build our SEDs are shown in Table 4.3.

SED fitting results

In the case of Astarte, the CF00 and LF17 attenuation laws result in best SED fits over C00. The BIC of every model was calculated and is shown in Table 2.4 along with the other quality of fit assessments. $\Delta BIC_{(C00,CF00)} = 21.88$ and $\Delta BIC_{(CF00,LF17)} = 2.29$, this privileged the best fit produced with the LF17 attenuation law and therefore was taken into account in deriving the physical properties. Despite the uncertainties on any assumed SFH model, the adopted SFH here fit the short wavelength data best.

For the less-massive Adonis, CF00 gave overall better fits than C00 and LF17, with $\Delta BIC_{(LF17,CF00)} = 3.48$ and $\Delta BIC_{(C00,CF00)} = 5.77$. The best SEDs of Astarte and Adonis are shown in Figure 2.4. The signature of dust attenuation is clear in the two SEDs, where the heavily dust-obscured Astarte has more attenuation of its overall stellar mass than is the case with Adonis. The derived properties of both galaxies are shown in Table 2.5. The L_{IR} of Astarte of about 10^{12} qualifies it to be an ultraluminous IR galaxy (hereafter ULIRG), while the low dust content of Adonis is manifested in the weaker IR luminosity and lower dust mass.

To closely inspect the visible dissociation of the gas and the stellar population in Astarte, we followed the method used in Buat et al. (2019) by dissecting the stellar continuum and the IR emission and comparing their derived properties with those obtained using full SEDs. Taking the UV to near-IR data (0.3 - 8 μm) into account, the best fit for the stellar continuum was obtained with the C00 law, with $\Delta BIC_{(CF00,C00)} = 8.3$ and $\Delta BIC_{(LF17,C00)} = 2.7$. The better quality fit of the stellar continuum produced using C00 is expected because this

Physical property	Astarte	Adonis
redshift	$z_{CO} = 2.154$	$z_{spec} = 2.140$
L_{IR} $(10^{12}\ L_\odot)$	3.16 ± 0.06	0.62 ± 0.04
SFR $(M_\odot/yr)$	395 ± 20	129 ± 59
$M_\star (M_\odot)$	$(3.74 \pm 0.19) \times 10^{11}$	$(9.37 \pm 1.76) \times 10^9$
$M_{dust}(10^9 M_\odot)$	1.01 ± 0.11	0.86 ± 0.13

TABLE 2.5: Summary of the physical properties obtained for Astarte and Adonis obtained with CIGALE.

power law effectively attenuates the young stellar population, while the other two laws can be equally efficient in attenuating the older stars, a behavior that translates into a rise in the near-IR absorbed light and therefore a rise in the total IR emission. The IR luminosity derived from the stellar continuum gives $L_{dust} = (2.43 \pm 1.01) \times 10^{12}\ L_\odot$, relatively close to L_{dust} derived from the full SED. The stellar mass derived from the stellar emission gives $(1.3 \pm 0.2) \times 10^{11}\ M_\odot$ and the $\text{SFR}_{(UV-near-IR)} = 430\ M_\odot yr^{-1}$. From the IR data (MIPS - ALMA continua), we obtain $L_{dust} = (3.25 \pm 0.08) \times 10^{12}\ L_\odot$, consistent with the luminostiy derived with the full SED. This result agrees with the results of Buat et al. (2019), who they found consistent dust luminosities derived from both the full SED and the IR data, while L_{dust} deduced from the stellar continuum was underestimated.

2.5 Discussion

Figure 2.5 shows the relative position of our galaxies to the MS of Schreiber et al. (2015). Adonis lies on 10×MS, qualifying it to be a strong SB, despite its relatively low SFR. While being a SB, this type of source cannot be detected even by the deepest 3 mm ALMA survey (expected flux of $7\,\mu$Jy), which have a 1σ noise of $9.7\,\mu$Jy González-López et al. (2020). Astarte is a MS galaxy with all the different attenuation recipes used. However, there is a clear difference concerning the position of Astarte relative to the MS as a result of the three attenuation laws. This is attributed to the significant difference in the derived stellar masses, with CF00 and LF17 attenuation laws resulting in a higher stellar mass than C00 as a result of the highest attenuation in near-IR. This contributes to a lower specific SFR (sSFR = SFR/$M_\star$) because SFRs do not differ significantly with the three laws.

The host halo masses of z~2 *Herschel*-detected massive MS galaxies were investigated in Béthermin et al. (2014) using clustering and X-ray stacking and were found to reside in halos of $>10^{13}$ $M_\odot$. These halo masses are also expected from the relation of stellar mass to halo mass (Behroozi et al., 2013; Durkalec et al., 2018; Behroozi et al., 2019). Astarte is about four times less massive than the average central galaxies at z~1 of Hilton et al. (2013) and van der Burg et al. (2013), which indicates that these MS giant galaxies continue to grow either through in situ star formation or accretion of other galaxies throughout cosmic time until lower redshifts.

We compared Astarte with CO-detected samples of the same redshift range from Genzel et al. (2010) (labeled G10) and Tacconi et al. (2013) (labeled T13). These samples of SFGs have constrained CO detections and well-investigated physical parameters (in Sargent et al., 2014).

We compared the molecular gas mass of Astarte derived from the CO emission line with that of G10 and T13 galaxies in Figure 2.6. G10 used a galactic conversion factor for SFGs and $\alpha_{CO} = 1$ for ULIRGs, while T12 adopted a galactic conversion factor for all their
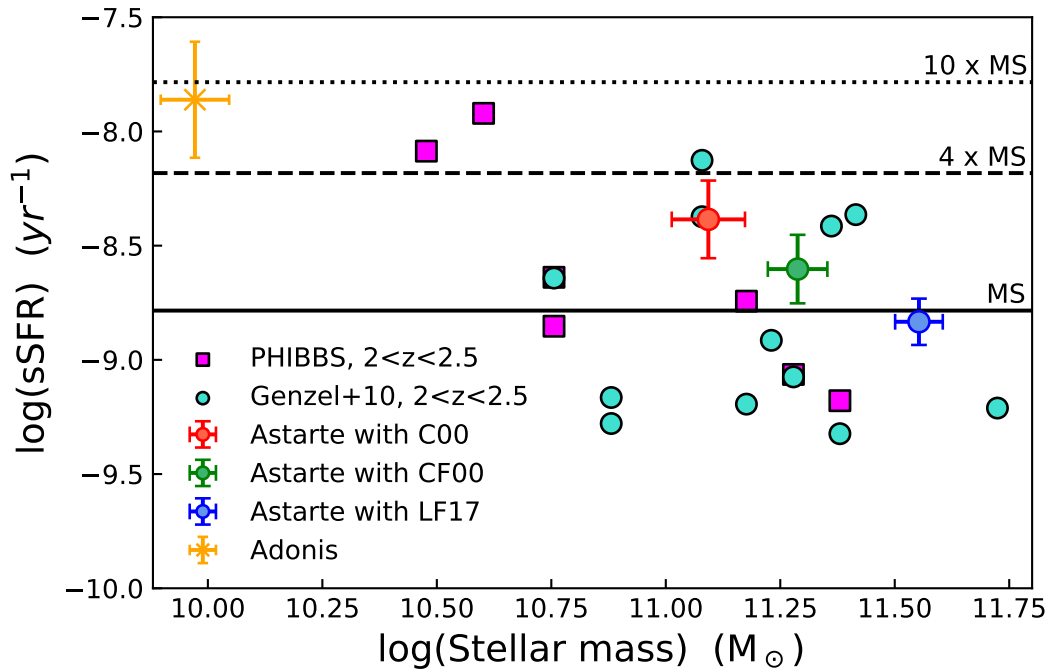
FIGURE 2.5: Relative position of the sSFR (SFR/M$_\star$) and stellar mass of Astarte using the three attenuation laws to the main sequence of Schreiber et al. (2015) at z=2. The yellow star shows the relative position of Adonis to the MS. Magenta squares denote PHIBSS CO-detected SFGs at z≈ 2 (Tacconi et al., 2013). Turquoise circles are ULIRGs at 2<z<2.5 from Genzel et al. (2010). The solid line shows the MS of Schreiber et al. (2015). The dashed and dotted lines are $MS \times 4$ and $MS \times 10$, respectively.

sources. Our choice of $\alpha_{CO} = 0.8$ underestimates the molecular gas mass of Astarte compared to the galaxies of G10 and T13. However, $\alpha_{CO} = 4.36$ produces a higher molecular gas mass with respect to its sSFR.

In Figure 2.7 we show the correlation between CO luminosities and the total IR luminosities. IR luminosities were derived from the SFRs of all the sources (G10, T13, and Astarte) using the Kennicutt relation (Kennicutt, 1998). The initial choice of $r_{31} = 0.42 \pm 0.07$ (the average in Daddi et al., 2015) places Astarte on the SB line from Sargent et al. (2014), contradicting its SED result. We therefore investigated the lowest excitation ratio from Daddi et al. (2015) of $r_{31} = 0.27 \pm 0.07$. This lower ratio moves Astarte closer to the MS within the error bars.

Using the total molecular gas mass of Astarte derived with the least excited CO(3-2) from Daddi et al. (2015) ($r_{31} = 0.27 \pm 0.07$), and assuming a galactic conversion factor, we estimate a gas fraction $f_{gas} = M_{gas}/(M_{gas} + M_\star) = (0.27 \pm 0.07)$. Although this falls within the lower limits of typical molecular gas fractions found in SFGs at z≈2 in Santini et al. (2014) and Béthermin et al. (2015), an α_{CO} adapted for SB with a higher r$_{31}$ ratio reduces the gas fraction significantly.

The gas mass derived with a galactic conversion factor gives Astarte a rather short depletion time of 0.22 ± 0.07 Gyr, making it very efficient at forming stars (for comparison, SBs have a depletion time of ~ 100 Myr, see Fig. 10 in Béthermin et al. 2015). Recently, Elbaz et al. (2018) found that compact SFGs on the MS with a relatively short depletion time are common. These active ultramassive objects can be hidden at the higher end of the tail of the MS. The average depletion time for the Elbaz et al. (2018) galaxies is about 0.25 Gyr, and
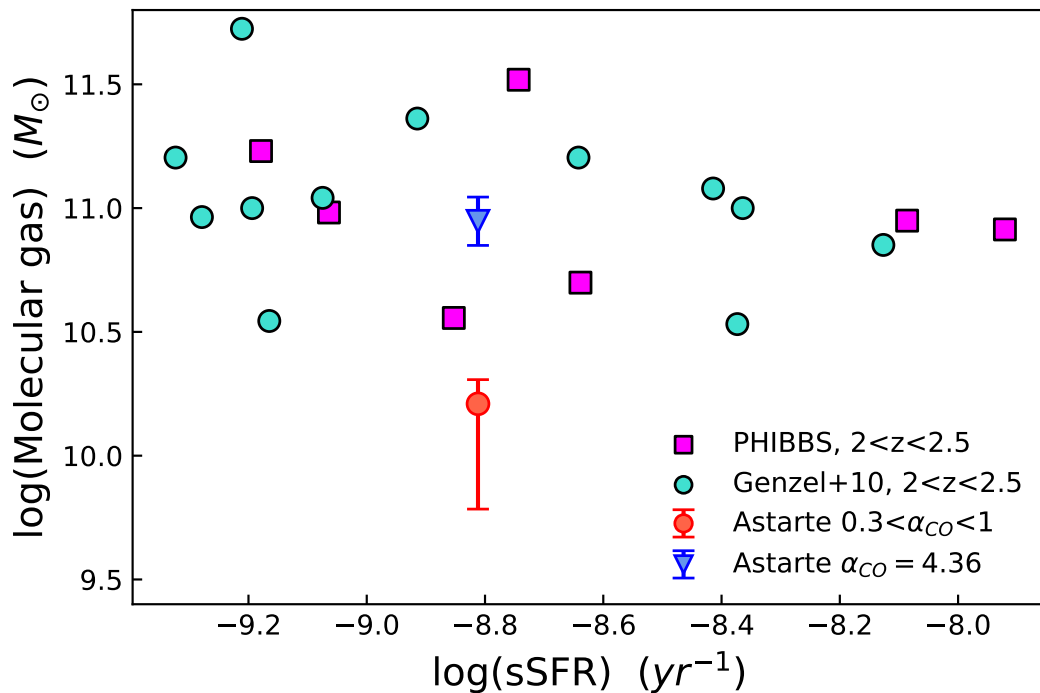
FIGURE 2.6: Molecular gas masses derived with the CO conversion factor vs. the sSFR. The magenta squares are from T13. Turquoise circles are ULIRGs at 2<z<2.5 from G10. The red circle shows the position of Astarte with $\alpha_{CO} = 0.8$, and the associated error bar shows the variation of the molecular gas mass using $0.3<\alpha_{CO}<1$. The blue triangle shows the molecular gas of Astarte for a galactic CO conversion factor of 4.36.

although we do not detect the continuum of Astarte with ALMA, its CO emission is compact, as it is the case for the continuum of ALMA-detected galaxies from Elbaz et al. (2018). This is also confirmed in Puglisi et al. (2019), where compact massive galaxies at the top of the MS exhibit high SFRs at their cores following their SB epoch.

2.6   Conclusion

We analyzed two galaxies, Astarte and Adonis, at the peak of the SFR density using multi-wavelength dissection combining ALMA observations with UV-submillimeter SED model-ing. We investigated the molecular gas content of Astarte through the ALMA detection of its CO(3-2) emission, relying on different excitation ratios of $L'_{CO(3-2)}/L'_{CO(1-0)}$ and different CO conversion factors. A galactic conversion factor when used along with the least excita-tion ratio from Daddi et al. (2015) confirmed the relative position of Astarte to the MS, as found from its SED modeling. Although the obtained gas fraction is at the lower limits of the fraction in MS galaxies (Santini et al., 2014; Béthermin et al., 2015), a possible explanation might be that the CO(3-2) instantaneous emission does not fully recover the molecular mass and the dynamics of Astarte because the excitation is weak (Daddi et al., 2015). Detections of other transition levels of CO would be helpful to better constrain the molecular mass of Astarte, and therefore its physical characteristics.

The physical dissociation of the CO line and the rest-frame stellar population in Astarte was also investigated, as was done in Buat et al. (2019), by deriving physical properties from the stellar emission (UV to near-IR) and the IR emission apart. As in Buat et al. (2019),
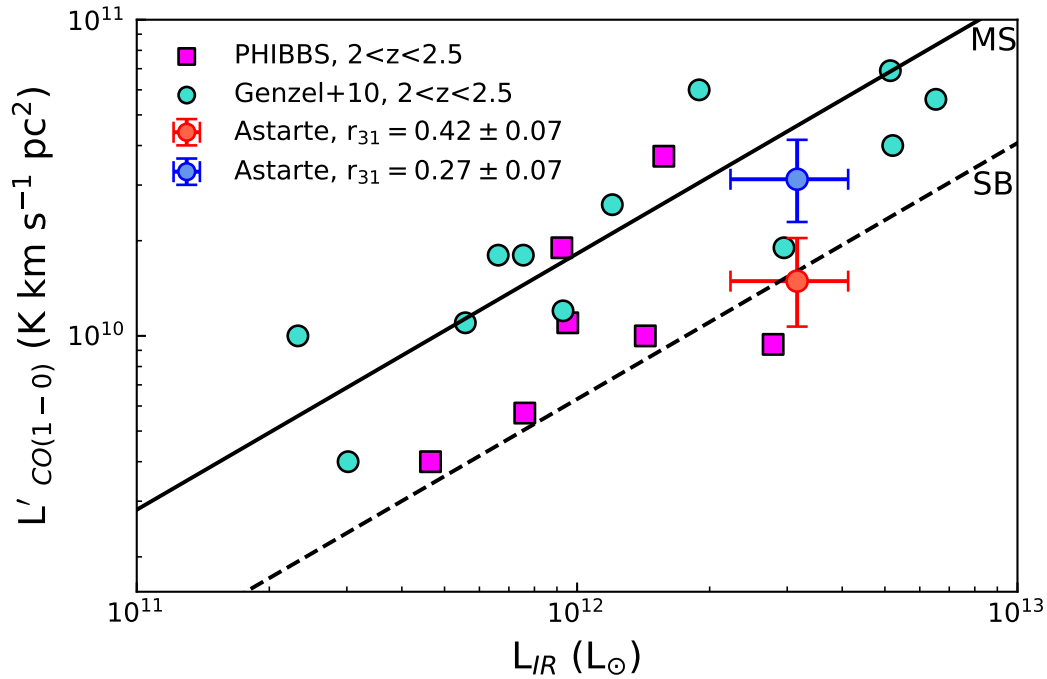
FIGURE 2.7: Correlation between CO(1-0) luminosities and the total IR luminosity. The filled magenta squares are from T13 and filled turquoise circles are the sources from G10. The solid black line is the linear regression for MS galaxies (Sargent et al., 2014), and the dashed line is that for SBs (the regression lines are from the complete sample in Sargent et al. 2014).

the dust luminosity derived from the full SED agrees with the luminosity derived from the the IR emission, while L_{dust} derived from the stellar emission is slightly underestimated. Furthermore, the C00 attenuation law was preferred when the stellar continuum alone was fit. This is consistent with the results of Buat et al. (2019) for galaxies with the same radial extension of rest-frame stellar emission and ALMA-detected emission. The LF17 attenuation law, which was tuned for ULIRGs at $z \sim 2$, succeeds best in mimicking the dust attenuation of Astarte when the whole UV-submillimeter SED was fit; this results in a higher stellar mass, however.

The molecular mass of Astarte, obtained with a galactic conversion factor and the lowest excitation ratio from Daddi et al. (2015), contributes to ~ 0.9 of its total dynamical mass, which is a larger contribution than what was found in ULIRGs by Neri et al. (2003). SFRs and stellar masses derived from the SED fittings show that Adonis is a SB galaxy, while Astarte is on the MS of SFGs. However, the small gas fraction makes Astarte very efficient in forming stars; its depletion time is an order of magnitude lower than what is expected in typical MS galaxies (Béthermin et al., 2015). This SB-like star formation activity on the MS was found for massive compact SFGs in Puglisi et al. (2019) in their post-SB phase. Short depletion times of MS massive galaxies were also found by Elbaz et al. (2018), confirming that Astarte is caught in the middle of quenching following an earlier SB activity.

Central galaxies at z~1 from Hilton et al. (2013) and van der Burg et al. (2013) are about four times more massive than Astarte. This indicates that even massive objects that are at the high end of the MS, when the Universe was undergoing its peak in the star formation rate density, continue their mass assembly down to lower redshifts.

Summary of the second chapter

- In this work, I studied a system of two galaxies around the cosmic noon, when the peak of star formation rate density took place. I used multiwavelength observations, including ALMA, VLA, and HST, to investigate the physical properties of these galaxies.

- The heavily obscured galaxy has a large stellar mass of $3.74\pm0.19 \times 10^{11}$ solar masses and a high star formation rate of 395 ± 20 solar masses per year. This galaxy has a compact, clumpy structure with a relatively low gas fraction (derived using the CO emission line). Additionally, it is not visible in the HST bands.

- The blue companion galaxy has a much lower mass ($9.37\pm1.76 \times 10^9$ solar masses) and a star formation rate that qualifies it to be a strong starburst.

- The low depletion time (0.22 ± 0.07 Gyr) of the massive infrared-bright galaxy suggests a strong starburst activity. However, the location of this galaxy with respect to the main sequence of star-forming galaxies, suggests a normal star formation activity.

- This starburst-like star formation activity on the main sequence was found for massive compact galaxies in post-starburst episodes, confirming that the massive ALMA-detected IR galaxy is caught in the middle of quenching following an earlier starburst activity.

- Assumed dust attenuation laws play a key role in deriving the physical properties of massive star-forming galaxies. Steeper attenuation curves produced less stellar mass while shallower curves resulted in larger stellar mass.

- A careful choice of dust attenuation law is crucial in studying dusty star-forming galaxies. The understanding of galaxies' morphological extensions in determining the most likely attenuation law, is needed.

3

Correlation of dust attenuation laws with star-to-dust compactness since $z = 4$

This chapter originally appeared as 'The slippery slope of dust attenuation curves: Correlation of dust attenuation laws with star-to-dust compactness since $z = 4$' by M. Hamed et al. 2023, Astronomy & Astrophysics, (Hamed et al., 2023)

3.1 Abstract

We investigate the dust attenuation of 122 heavily dust-obscured galaxies detected with the Atacama Large Millimeter Array (ALMA) and *Herschel* in the COSMOS field. We search for correlations between dust attenuation recipes and the variation of physical parameters, namely, the effective radii of galaxies, their star formation rates, and stellar masses. We aim to understand which of the commonly used laws best describes dust attenuation in dusty star-forming galaxies (DSFGs) at high redshift. We made use of the extensive photometric coverage of the COSMOS data combined with highly resolved dust continuum maps from ALMA. We used CIGALE to estimate various physical properties of these dusty objects, namely: their star formation rates (SFR), their stellar masses, and their attenuation at short wavelengths. We inferred the effective radii (Re) of galaxies using GALFIT in the *Y* band of HSC and ALMA continuum maps. We used these radii to investigate the relative compactness of the dust continuum and the extension of the rest-frame UV/optical Re(y)/Re(ALMA). We find that the physical parameters calculated from our models strongly depend on the assumption of the dust attenuation curve. As expected, the most impacted parameter is the stellar mass, which leads to a change in the "starburstiness" of the objects. We find that taking into account the relative compactness of star-to-dust emission prior to SED fitting is crucial, especially when studying dust attenuation of dusty star-forming galaxies. Shallower attenuation curves do not show a clear preference of compactness with attenuation, while the Calzetti attenuation curve is shown to prefer a comparable spatial extent of unattenuated stellar light and dust emission. The evolution of the $R_e(UV)/R_e(ALMA)$ ratio with redshift peaks around the cosmic noon in our sample of DSFGs, showing that this compactness is correlated with the cosmic SFR density of these dusty sources.

3.2 Introduction

In its earliest phases of evolution, the Universe not only experienced higher star formation rates (SFRs), but a significant fraction of this SFR was obscured by dust (e.g., Blain et al., 2002; Chapman et al., 2005; Takeuchi et al., 2005; Bouwens et al., 2012; Madau et al., 2014; Magnelli et al., 2014; Bourne et al., 2017; Whitaker et al., 2017; Gruppioni et al., 2020; Khusanova et al., 2020). Dusty star-forming galaxies (DSFGs, e.g., Viero et al., 2013; Weiß et al., 2013b; Casey et al., 2014; Béthermin et al., 2015; Strandet et al., 2016; Casey et al., 2017; Reuter et al., 2020), which are heavily attenuated in the ultraviolet (UV), have contributed notably to the cosmic SFR, making them crucial to our general comprehension of galaxy evolution. These dust-rich galaxies have managed to stack up their stellar masses across relatively short timescales, while efficiently depleting their gas reservoirs. Therefore, they may in fact be the direct progenitors of ultramassive passive red galaxies that are often encountered at high redshift (e.g., Daddi et al., 2005; Whitaker et al., 2013; Nayyeri et al., 2014; Toft et al., 2014; Carnall et al., 2020).

Our understanding of the nature of DSFGs has benefited from the plethora of multiwavelength photometry over the last two decades. With a decade's worth of observation programs carried out by the Atacama Large Millimeter/submillimeter Array (ALMA), it has become possible to enrich our datasets of infrared (IR) galaxies at higher redshifts via the multiplicity based on their blended, lower resolution detections with *Spitzer* and *Herschel*. This has recently made modeling dust attenuation at high redshifts a hot topic (e.g., Popping et al., 2017; Wang et al., 2017; McLure et al., 2018; Buat et al., 2019; Salim et al., 2019; Fudamoto et al., 2020).

Interstellar dust is highly efficient in absorbing the short wavelength photons, predominantly originating from young UV-bright massive stars, rendering the star-forming cold regions of the DSFGs virtually inaccessible. This attenuated light can be successfully reproduced by assuming a dust attenuation law (e.g., Burgarella et al., 2005; Buat et al., 2012, 2014; Lo Faro et al., 2017; Salim et al., 2018, 2020). In reality, however, a single attenuation law cannot mimic dust extinction in the interstellar medium (ISM) of a large and diverse sample of galaxies (e.g., Wild et al., 2011; Kriek et al., 2013; Buat et al., 2018; Małek et al., 2018; Salim et al., 2020). Different approaches appear to work when modeling dust attenuation with the aim of reproducing the spectral energy distributions (SEDs) of galaxies. Calzetti et al. (2000) derived a universal effective attenuation law that is used as a screen model by measuring the extinction in local starburst galaxies. The attenuation curve of Calzetti et al. (2000) succeeds in modeling dust reddening even at high-redshift metal-poor galaxies with a bright cold dust component. The double component dust attenuation law of Charlot et al. (2000) assumes a more complex, physical mixing of dust and stars. With this approach, newly formed stars are placed in the cold molecular clouds and experience double attenuation by the dust of the molecular clouds and the ISM. Older stars are attenuated by the dust grains of the ISM alone.

These attenuation laws, together with their different recipes, are often used in the literature when modeling the SED of galaxies. Such recipes include a steeper curve than that of Calzetti et al. (2000), with a UV bump around 0.217μm (Buat et al., 2011, 2012) and a shallower ISM attenuation than that of Charlot et al. (2000) (e.g., Lo Faro et al., 2017). However, when it comes to DSFGs, a proper dust attenuation curve that is able to accurately mimic the absorbed photons is crucial for any SED analysis, especially given that for these objects, dust plays a massive role in their evolution and is an important agent for their SEDs.

On the other side of the SED, the long-wavelength cutoff of the Rayleigh-Jeans-approximated tail is extensively covered by ALMA. Therefore, its cold dust continuum provides a vital element in the far-infrared (FIR) SEDs of DSFGs. However, ALMA-detected cold dust-emission maps at high resolution were often found to disagree spatially with detections at

shorter wavelengths, such as in the case of the UV-emitting star-forming regions or the stellar populations of DSFGs (e.g., Dunlop et al., 2017; Elbaz et al., 2018; Buat et al., 2019). This disagreement can either take the form of different levels of dust compactness relative to the higher energy detections or, in some cases, a complete physical dissociation of these two components. Such offsets are often found to be more significant than the systematic offsets that arise from instrumental uncertainties or large beam sizes (Faisst et al., 2020). In most cases, radio detections with the Karl G. Jansky Very Large Array (VLA) has confirmed the ALMA-detected physical dissociation (e.g., Rujopakarn et al., 2016; Dunlop et al., 2017; Elbaz et al., 2018; Hamed et al., 2021). This separation challenges a local energy balance, which could be an issue for SED modeling that takes into account a global conservation of energy. This problem was recently highlighted in Buat et al. (2019), since such an energy balance is at the core of widely used SED fitting tools (e.g., da Cunha et al., 2008; Noll et al., 2009; Boquien et al., 2019).

Reverse engineering the spectral distribution of DSFGs does not come without obstacles, despite the advent in current understanding of the physical and chemical processes that such galaxies undergo. The most commonly confronted obstacle in SED fitting is the degeneracy problem. Such a degeneracy arises from overlapping different physical contribution in one specific wavelength domain, such as the dust and stellar age degeneracy (e.g., Hirashita et al., 2017). Although this can be overcome by assuming an energetic balance and using the FIR emission as an additional constrain for dust attenuation and by choosing an appropriate star formation history (SFH, see Ciesla et al., 2016), a well-constrained attenuation curve will help limit such degeneracies, leading to better estimated physical parameters.

Dust attenuation curves significantly alter the stellar mass determination of galaxies (in general) and of DSFGs (in particular). As flatter and geometrically complex attenuation curves can dim the light coming from the older stellar populations in the ISM more efficiently than steeper ones, they naturally result in a significant hidden older stellar population in the optical to near-infrared (NIR) range. This, along with other assumptions such as the initial mass function (IMF) and the SFH, leads to large differences in the resulting stellar masses (e.g., Zeimann et al., 2015; Małek et al., 2018; Buat et al., 2019).

The uncertainty in the stellar mass determination of DSFGs (see the stellar mass controversy in Hainline et al., 2011; Michałowski et al., 2012; Casey et al., 2014) remarkably influences the position of these objects along the commonly named main sequence (MS) of star-forming galaxies (e.g., Brinchmann et al., 2004; Noeske et al., 2007; Daddi et al., 2010; Rodighiero et al., 2011; Lo Faro et al., 2015; Schreiber et al., 2015; Hamed et al., 2021). Most galaxies seem to follow the tight scatter of the MS independently of the redshift, whose outliers are typically referred to as starbursts. However, the strong dependence of the stellar mass estimation from SED fitting techniques on the assumed attenuation curve, varies massively this scatter and affects the "starburstiness" of already active DSFGs. It is therefore crucial to choose suitable attenuation laws in order to limit biases on the stellar mass determination.

Recently, Donevski et al. (2020) investigated the dust and gas contents of a large sample of DSFGs, linking dust abundance to other physical characteristics such as their SFRs. Despite the growing understanding of these objects, we still lack a complete picture of how dust attenuates their stellar radiation. Properly quantifying dust attenuation of DSFGs is crucial for quantifying the cosmic SFR and get a better grip on galaxy evolution. To achieve this goal, we study closely the dust attenuation curves in DSFGs and investigate the possible physical properties that they might depend on. With the constant improvements in our understanding of the nature of these dusty galaxies, many works have recently studied the relation between dust attenuation and other physical properties (e.g., Fudamoto et al., 2020; Lin et al., 2021; Boquien et al., 2022; Lower et al., 2022). In these works, links between dust attenuation properties and other physical observables were studied, such as the dust grain sizes, star-dust

geometry, and the star formation activity in these galaxies. The most widely used attenuation laws are that of Calzetti et al. (2000) and Charlot et al. (2000). Both of these laws are used interchangeably when modeling galaxies' photometry at high redshifts. However, we still lack a complete knowledge of the preference of attenuation laws in DSFGs at different redshift ranges.

In this paper, we aim to answer the question of which of the commonly used laws best describes dust attenuation in DSFGs at high redshift. Measuring the slopes of attenuation is beyond the scope of this paper. We make use of a large statistical sample with available dust continuum maps and their UV/optical counterparts. We study the effect of UV/optical to dust continuum compactness on the preferred attenuation law for our sample.

This paper is structured as follows. In Section 3.3, we describe the data analyzed in this work, both in terms of the photometry and the images. In Section 3.4.1, we detail the method we use to estimate the circularized effective radii of our sources. Section 4.4 provides a description of the SED fitting procedures we used to achieve the physical properties of our sources. The results and their respective discussions are presented in Section 3.5. Our summary and conclusions are given in Section 5. Throughout this paper, we adopt the stellar IMF of Chabrier (2003) and a ΛCDM cosmology parameters (WMAP7, Komatsu et al., 2011): $H_0 = 70.4$ km s^{-1} Mpc^{-1}, $\Omega_M = 0.272$, and $\Omega_\Lambda = 0.728$.

3.3   Sample selection

The large two-square-degree COSMOS field, centered on R.A., Dec. = (10h00m27.9171s, +02d12m35.0315s) (Scoville et al., 2007; Ilbert et al., 2013; Laigle et al., 2016), has been observed with an unmatched commitment from different instruments, covering a wide range of wavelength observation of galaxies up to redshift of six. This unique survey design offers rich data sets of millions of identified galaxies, allowing for deep investigations of galaxy evolution at various redshifts. The choice of COSMOS field galaxies in this work is motivated by the abundance of multiwavelength data spanning across a wide range of redshifts and the significant number of ALMA detections that this field enjoys. This set of optical, infrared, and submillimeter detections have allowed us to build a statistical sample of DSFGs. This sample is ideal for investigating the evolution of DSFG properties and the crucial role that dust attenuation plays in their evolution.

3.3.1   ALMA data

Since the main science objective in this study is to quantify the effect of the distribution of dust emission relative to the stellar continuum at different redshift ranges, the core of our sample was built around ALMA detections. For that purpose, we used ALMA fluxes and continuum maps from the A^{3}COSMOS automated ALMA data mining in the COSMOS field (Liu et al., 2019). This data set assembles hundreds of identified galaxies from the ALMA archive into a single catalogue. In our work, we use the primary beam-corrected ALMA maps.

The main advantage in our work is having access to dust continuum morphology relative to the spatial distribution of the star formation region and the stellar population in our sample. For this reason, we carefully selected a sample of galaxies characterized by good-quality detections.

For the submillimeter images, we use the A^{3}COSMOS-generated maps (Liu et al., 2019). These images were deconvolved using a robust cleaning with a Brigg's parameter of 2, namely, a natural weighting of visibilities. This results in significantly better signal-to-noise

TABLE 3.1: Summary of available photometric data in each band with its centered wavelength, the mean of S/N, and the number of detections in our sample. The detections of different ALMA bands (6 and 7) concern different galaxies.

Telescope/ instrument	Band	λ (μm)	Median S/N	Nº of detections
CFHT/MegaCam	u	0.38	25.13	107
	g	0.49	32.56	117
	r	0.62	66.10	122
	i	0.75	58.59	122
	z	0.89	38.01	122
Subaru/Suprime-Cam	B	0.437	28.00	122
	V	0.544	28.38	117
	Y	0.98	25.61	122
VISTA	J	1.25	81.01	122
	H	1.64	93.16	122
	Ks	2.15	100.82	122
Spitzer/IRAC	ch1	3.56	146.06	122
	ch2	4.50	157.26	122
	ch3	5.74	12.97	122
	ch4	7.93	10.12	122
Spitzer/MIPS	MIPS1	23.84	47.76	122
Herschel/PACS	100 μm	102.61	5.41	122
	160 μm	167.13	2.68	122
Herschel/SPIRE	250 μm	251.50	12.62	122
	350 μm	352.83	7.19	122
	500 μm	511.60	3.63	122
	7	947	12.47	85
ALMA	6	1255	12.89	37
				total = 122
JVLA	S (3 GHz)	1.3×10^5	14.10	122

(S/N) of the innermost regions of a source in the uv plane, thus defining its outermost "borders" in the image plane (see Section 2.1 in Liu et al. 2019 for a more detailed description of produced ALMA continuum images). To study dust attenuation through cosmic time, we select ALMA-detected galaxies with S/N higher than 5. Our preliminary sample is composed of 1,335 individual ALMA-detected galaxies.

3.3.2 Ancillary maps

For the shorter wavelength (rest-frame UV and optical) images, we used the third data release of the deep field continuum maps detected with the *y* band of the Hyper Suprime-Cam (HSC) of *Subaru* (Miyazaki et al., 2018; Aihara et al., 2022). These images have high angular resolution (0.64), which allows for a physical comparison with their ALMA counterparts.
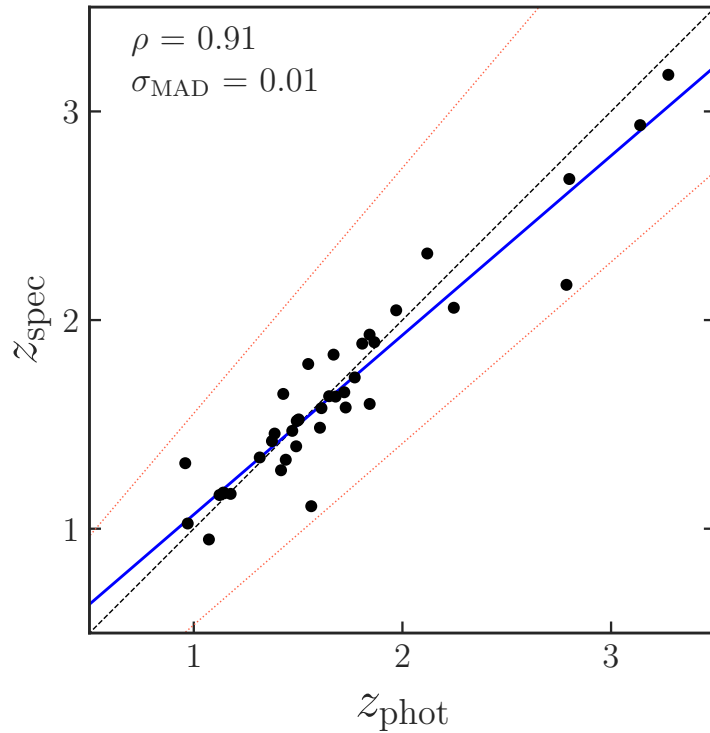
FIGURE 3.1: Comparison between the photometric redshifts of 43 galaxies
from the final sample, for which spectroscopic redshifts are available from
the literature (Liu et al., 2019). The Spearman's rank correlation coefficient
is shown as ρ, with the photometric redshift accuracy given by σ_{MAD} (Ilbert
et al., 2009). The red dotted lines correspond to $z_p = z_s \pm 0.15(1 + z_s)$
(Ilbert et al., 2009).

3.3.3   Auxiliary photometric data

We used the photometric data from the *Herschel* Extragalactic Legacy Project (HELP) panchro-
matic catalog (Shirley et al., 2019). This catalog was compiled while taking into account
visible to mid-infrared (MIR) range surveys as priors, homogenizing them, and extracting
fluxes from *Herschel* maps, whose angular resolution is significantly lower than their short-
wavelength counterparts.

To build the HELP catalogue, *Herschel* fluxes were extracted using the probabilistic de-
blender XID+ (Hurley et al., 2017), used on SPIRE maps, taking into into account the po-
sitions of sources observed with the high-resolution detections from *Spitzer* at $24\mu m$. This
technique was shown to increase the accuracy of photometric redshift estimations (Duncan
et al., 2018).

We performed a positional cross-match between ALMA catalogue and the HELP cata-
logue with a rather conservative 1 search radius. Although galaxies whose dust continuum
or molecular gas emission is significantly dissociated from the shorter wavelength continua
are not uncommon (e.g., Elbaz et al., 2018; Hamed et al., 2021), due to various factors such
as astrometry problems, positional errors as a result of the beam size, or physical factors,
this timid search radius avoids false matches (e.g., Buat et al., 2019; Liu et al., 2019). This
cross-matching procedure resulted in 383 individual galaxies ranging from z=0.3 to z=5.5.

To better constrain the physical properties of our statistical sample through SED model-
ing, we discarded galaxies that have fewer than three detections in the UV-NIR wave range.

This requirement rejected 30% of the sources. Additionally, we required minimum six detections in the MIR-FIR bands (8–1000 μm) out of which at least five detections would have a S/N>3. As a result of these selection criteria, the finally-selected sources have at least 10 detections in the UV to NIR (0.3–8 μm) range with S/N>5. For objects that had detections in similar bandpass filters, we used the detections coming from the deeper survey. This has a high importance in SED fitting procedures especially because measurements at similar wavelengths may be several orders of magnitude different from each other, which will negatively affect the quality of their fitted spectrum. Moreover, dense coverage of a very short part of the SED could add too much weight during the SED fitting process and bias the final fit (Małek et al., 2018). Our UV–NIR photometric data as well as the FIR counterparts have overall high S/N (mean of 60 for the former and 13.23 for the latter), while in the IR side of the spectrum, MIPS measurements at 24 μm, as well as SPIRE detections at 250 and 350 μm (and evidently all ALMA detections) have high S/N values (mean of 12.68 for all bands). All *Herschel*'s SPIRE fluxes (at 250, 350 and 500 μm) are essential since they cover the thermal part of the total SED up to $z \sim 4$, which contains the Rayleigh-Jeans dust emission tail. To constrain the IR–submilimiter part of the SED fits even better, we appended our sources with VLA detections at 3 GHz from Smolčić et al. (2017).

3.3.4 Final sample

The above-described selection yields a final sample of 122 galaxies with panchromatically high S/N, covering a redshift range of $1 < z < 4$. A total of 43 galaxies of our sample have spectroscopic redshifts from Liu et al. (2019), and for the rest of the sample, we used the reliable photometric redshifts provided by the HELP catalogue. Figure 3.1 shows a comparison between the spectroscopic and photometric redshifts of the galaxies in our sample that possess both measurements. We calculated the photometric redshift accuracy (Ilbert et al., 2009) as $\sigma_{MAD} = 1.48 \times \text{median}(|z_p - z_s|/(1 + z_s))$, where MAD is the mean absolute deviation. This redshift accuracy resulted in reliable photometric redshifts of our sample with $\sigma_{MAD} = 0.014$.

Table 3.1 shows the photometric bands and the associated S/N for the final sample of 122 DSFGs. Almost half of the final sample, 60 galaxies, have a S/N of Y band detection higher than 5, and all of the sources had a VLA detection. We want to stress that only 15 DSFGs from our sample (12%) do not have u band detection and we are missing five detections in the g and V bands. With the exception of those galaxies, the rest of the sample has a full set of 23 photometric bands, assuring excellent spectral coverage, which is essential for a detailed SED fitting.

3.4 Methods

3.4.1 Size measurements

To study the spatial extent of dust emission and that of the stellar populations and the star-forming regions in our sample, we derived homogeneous effective radii (R_e) of the dust continuum maps and their short (UV-optical) wavelength counterparts. To achieve this, we used `GALFIT` (Peng et al., 2002), parametrically fitting two-dimensional (2D) Sérsic profiles in the primary-beam-corrected images of our sample. With the Sérsic index ($n^{\text{Sérsic}}$), obtained from the fitting procedure, it is possible to quantify the concentration of light in a galaxy, which can provide important information about its morphology. Moreover, `GALFIT` provides the values of the ratio between the minor and major axis, and this allows for calculating the effective circularized radii (hereafter simply effective radii or R_e). With spectroscopic and

(reliable) photometric redshift information, we can convert the data into the real sizes of our objects. In this work, we analyzed the evolution of IR radii between redshift four and one, but also simultaneously changes in the rest-frame UV-optical.

For our analysis, we used the *Y* band of HSC, and ALMA (bands 6 and 7) images to compute physical sizes of our final sample of DSFGs. The mean angular resolution of the ALMA detections in our sample is 0.75 and, equivalently, 0.64 for the HSC *Y* band detection. This renders a comparison between sizes estimated from each of these bands directly valid, without the need to degrade them in terms of resolution.
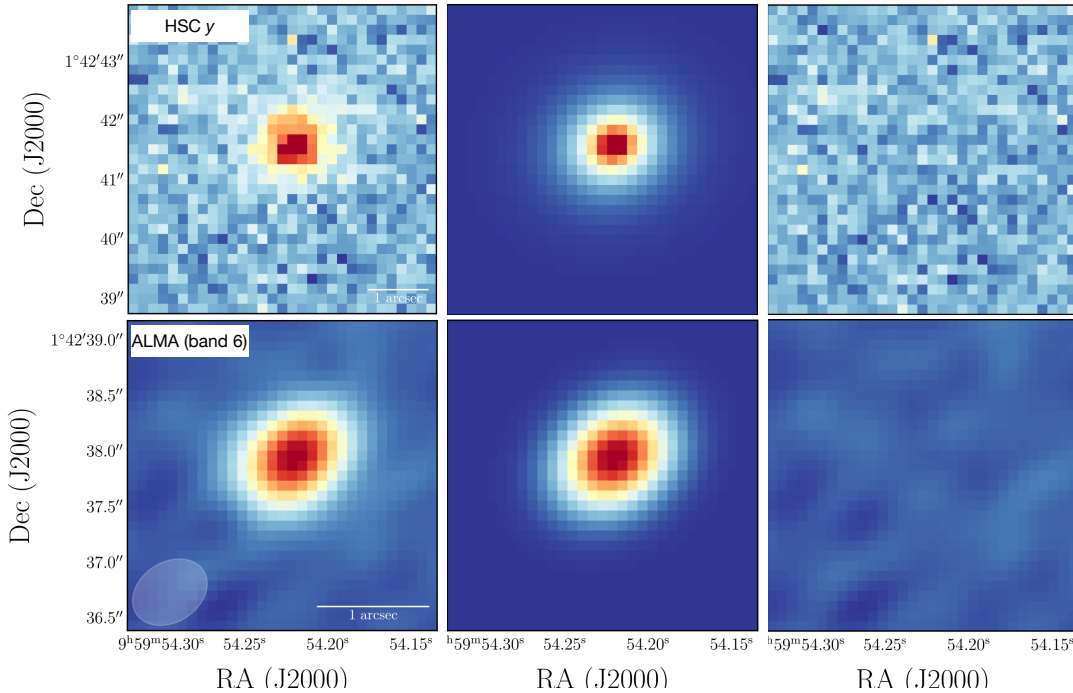
FIGURE 3.2: Example of `GALFIT` fitting of a galaxy from our sample (HELP-J095953.305+014250.922) with its modeled light profiles (second column) and its subsequent residuals (third column) at two different wavelengths shown from top to bottom. *Top:* HSC-*Y* band detection. *Middle:* ALMA band 6 detection. The left side of each row shows the scientific primary-beam-corrected image, with the beam size and the corresponding 1 arcsecond scale.

In computing the Sérsic profiles, we adopted a similar approach to Elbaz et al. (2018), by leaving ($n^{\text{Sérsic}}$) free. For the sake of comparison, we also fixed $n^{\text{Sérsic}} = 1$ (e.g., Hodge et al., 2016; Elbaz et al., 2018). While 5% of galaxies in our sample did not reach convergence when fixing $n^{\text{Sérsic}}$, R_e was found to be in good agreement in both cases (on average, 7% larger when fixing $n^{\text{Sérsic}}$ for ALMA detections) and we found an agreement within 23% for the resulting $n^{\text{Sérsic}}$ with a fixed and a free $n^{\text{Sérsic}}$.

In our profile fittings, we initially used an automated computation with `GALFIT` and we carefully checked the resulting models and their residuals. This was performed to get a general understanding of our sample's range of effective radii in each of the two used wavelength domains. This also allowed us to test different input values of $n^{\text{Sérsic}}$, including a Gaussian model – an important step when using this tool, since it alows us to validate the initial parameters needed for `GALFIT`. We found that varying $n^{\text{Sérsic}}$ between an exponential disk profile

TABLE 3.2: Summary of the derived effective radii of our sample from the available detections at two different wavelengths.

redshift	R_e^{ALMA} [kpc]	R_e^{UV-opt} [kpc]
$1 < z < 2$	2.59±0.25	5.75±0.18
$2 < z < 3$	2.12±0.32	5.03±0.22
$3 < z < 4$	2.54±0.15	3.54±0.26

($n^{\text{Sérsic}} = 1$) and a Gaussian profile ($n^{\text{Sérsic}} = 0.5$) leads to a slight change in the models and their consequent effective radii, with $R_e\,_{ALMA}^{n=0.5}$ being 26% smaller than $R_e\,_{ALMA}^{n=1}$.

After the aforementioned tests, we individually fit Sérsic profiles to each of our sources in the two bands (UV/optical and IR), while monitoring the resulting models, residuals, and profile parameters. This individual fitting was especially required for galaxies that did not fit in the automated computation ($\sim 5\%$ of the total sample), in the case of which a simple and slight parameter adaptation was enough to fit these sources. The distribution of the computed $n^{\text{Sérsic}}$ was rather narrow, ranging between 0.4 and 1.6 for ALMA detections and between 0.5 and 1.4 for the *Y* band.

Our technique in fitting Sérsic profiles in two bands of our sample was performed homogeneously in the same methodical approach. This is important to accurately quantify ratios of different R_e at varying wavelengths. Our primary effort was to calculate our effective circularized radii in a homogenized method with the same tool and approach, which reduces possible biases for the final physical interpretation. To test the reliability of our size measurements, we also computed the minimum possible size that can be accurately measured using the formula by Martí-Vidal et al. (2012) and Gómez-Guijarro et al. (2022):

$$\theta_{min} = 0.88 \times \frac{\theta_{beam}}{\sqrt{S/N}},$$

where the minimum size for each source (θ_{min}) is given in units of the synthesized beam FWHM (θ_{beam}), depending on the S/N of the source. All size measurements of our sample were above that limit.

Figure 3.2 shows an example of a galaxy `HELP-J095953.305+014250.922` at redshift z=2.15 seen in the HSC *Y* and ALMA band 6. Figure 3.2 shows the original image of that galaxy at two different wavelengths, with their light profiles fitted with `GALFIT`, and their subsequent residuals. The median radii and their errors (the median absolute deviation) at different redshift ranges are presented in Table 3.2, while the redshift evolution of these derived sizes along with the evolution of their star-to-dust compactness are shown in Figure 3.11 (left panel). This latter figure shows the change in the radii sizes (also related to the sample selection of DSFGs) of ALMA and HSC *y*, as well as a comparison with similar work done by Buat et al. 2019 based on galaxies at z~2. The evolution of these derived radii with the dust luminosity and stellar mass of our sample are shown in Appendix 3.7.2.
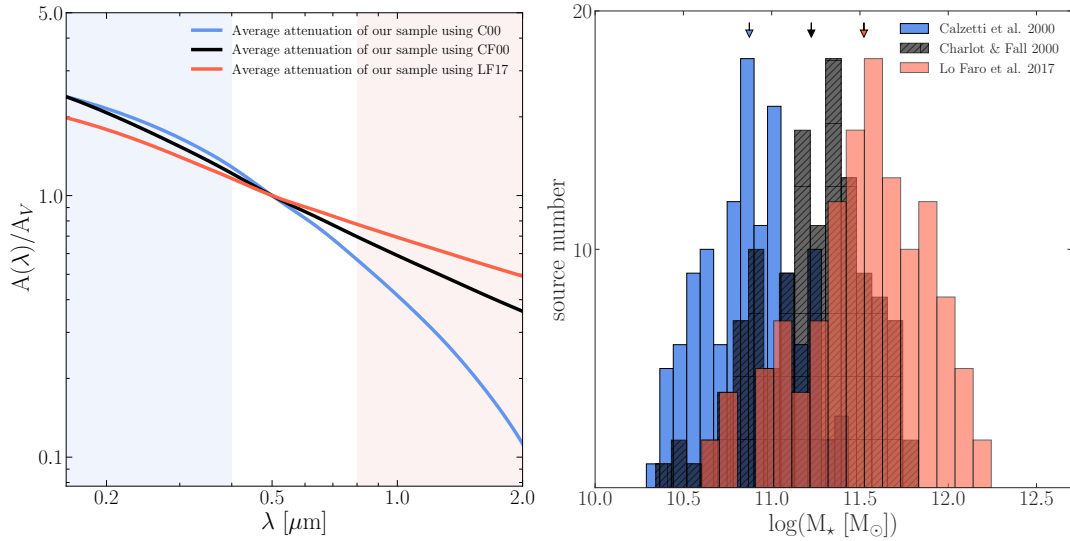
FIGURE 3.3: Average attenuation curves of our sample using three different attenuation laws/recipes (Calzetti et al., 2000; Charlot et al., 2000; Lo Faro et al., 2017) shown on the left. In the case of CF00 and LF17 curves, we show the combined curve of the ISM and the BC. Stellar masses of our sample are shown on the right, which were derived using the three attenuation curves as in the left panel. The arrows show the mean of the specific distribution.

3.4.2   SED fitting method

To derive the physical properties of our well-constrained multiwavelength sample, we used the Code Investigating GALaxy Emission CIGALE[1], an energy balance technique of the SED fitting (Noll et al., 2009; Boquien et al., 2019). This technique of SED fitting takes into account the balance between the energy absorbed in the rest-frame UV-NIR part of the total galaxy emission, and its rest-frame IR emission. The mediator agent in this energy balance is the dust, since it will absorb a significant part of the short wavelength photons emitted by the stars and emanate in the form of thermal emission in the FIR.

Reverse-engineering the total spectrum of a galaxy is not an easy feat. Some physical processes are completely unrelated, such as the synchrotron emission of accelerated electrons, which dominates the radio part of the SED, and the UV photons whose origins are traced directly back to the young stars. However, some physical processes release photons of the same frequency range, such as the MIR range which can have different contributors, such as active galactic nuclei (AGN) and polycyclic aromatic hydrocarbons (PAHs), resulting in degeneracies. Therefore, carefully choosing physically-motivated templates and parameters is crucial in order to deduce the key physical properties characterizing galaxies, since these parameters depend on the assumptions made (e.g., Ciesla et al., 2015; Carnall et al., 2018; Leja et al., 2018).

In the following subsections, we describe the different aspects of our SED fitting strategy, and motivate our choice of certain laws and parameters. The SED module description used in our work is presented below, with both the stellar part and the dust part.

Stellar SED

To forge the SED of a galaxy, we first assume a stellar population that is behind its direct and indirect emission. This means that we should take into account a stellar population library

---

[1]https://cigale.lam.fr/

TABLE 3.3: Input parameters used to fit the SEDs of our sample.

Parameter	Values
Star formation history	
delayed with a recent burst	
Stellar age (a)	redshift-dependent (0.5, 1, 2, 3, 5, 6, 8 Gyr)
e-folding time	1, 3, 6 Gyr
Age of recent burst	5, 10, 50, 100, 200, 300 Myr
Strength of the burst	0.001,0.005,0.01,0.2,0.3
Dust attenuation laws	
(Calzetti et al., 2000)	
Colour excess of young stars E(B-V)	0.1 - 1 by a bin of 0.1
f_{att}(b)	0.3, 0.5, 0.8, 1.0
(Charlot et al., 2000), (Lo Faro et al., 2017)	
V-band attenuation in the ISM A_V^{ISM}	0.3 - 6 by a bin of 0.1
Av_V^{ISM} / ($A_V^{BC} + A_V^{ISM}$)	0.3, 0.5, 0.8, 1
Power law slope of the ISM	-0.7, -0.48(c)
Power law slope of the BC	-0.7
Dust emission	
(Draine et al., 2014)	
Mass fraction of PAH	1.77, 2.50, 3.19
Minimum radiation field U_{min}	10, 25, 30, 40
Power law slope α	2
Synchrotron emission	
FIR/radio correlation coefficient	2.2, 2.4. 2.6
Power law slope slope	0.3, 0.6, 0.9

a) The age of the main stellar population.

b) Color excess of old stars.

c) Power law slope of LF17.

and its spectral evolution, stars with different ages and a certain metallicity. In this work, we used the stellar population library of Bruzual et al., 2003, along with the solar metallicity and an initial mass function (IMF) from Chabrier, 2003, which takes into account a single star IMF as well as a binary star systems.

The stellar population models were then convoluted with an assumed star formation history (SFH). These SFHs are sensitive to many complex factors including galaxy interaction, merging, gas accumulation, and depletion (e.g., Elbaz et al., 2011; Ciesla et al., 2018; Schreiber et al., 2018b; Pearson et al., 2019). The SFHs have a significant effect on the fittings of the UV part of the SED and, consequently, affect the derived physical parameters such as the stellar masses and the SFRs. Ciesla et al. (2016, 2017) showed that simple SFH models (such as a delayed model) are not enough to reproduce a precise fit of the UV data, especially for galaxies that are undergoing a starburst or quenching activity.

To model the SEDs of our IR-bright sample, we used a delayed SFH with a recent exponential burst (e.g., Buat et al., 2018; Małek et al., 2018; Donevski et al., 2020). This recent burst is motivated by the ALMA detection, which makes a scenario of numerous populations of young stars manifesting their presence through dust very likely. Furthermore, in such a
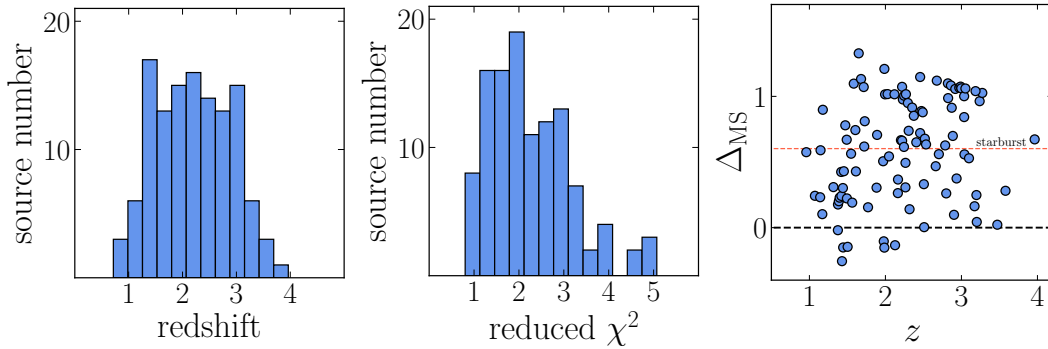
FIGURE 3.4: Redshift distribution of our sample of SFGs (left). Reduced χ^2 of the best fits of the galaxies in our sample using `CIGALE` (middle). Variation of ΔMS (distance to the main sequence of SFGs of Speagle et al. 2014) of the sample with redshift (right). The red dotted line shows the area above which a galaxy is considered a starburst.

scenario, a galaxy builds up the majority of its stellar population in its earlier evolutionary phase, then the star formation activity slowly decreases over time. This is followed by a recent burst of SFR. The SFR evolution over time is hereby modeled with:

$$SFR(t) \propto \frac{t}{\tau^2} e^{-t/\tau} + e^{-t'/\tau'}, \tag{3.1}$$

where the first term translates into a delayed SFH slowed by the factor of τ^2, which is the e-folding time of the main stellar population, extended over the large part of the age of the galaxy. The second term is the exponential decrease of recent SFR, where t' and τ' are the age of the burst and the e-folding time of the burst episode, respectively. This SFH provided better fits compared to the simpler delayed SFH, especially for non-quiescent galaxies. We varied τ (as shown in Table 4.2) to give a comprehensive flexibility of the delayed formation of the main stellar population. We discuss the choice of this SFH over a truncated version in Appendix 3.7.1.

Dust SED

The dust content of our sample of DSFGs is presumed to be the driving component of the shape of their SEDs. This makes the modeling of dust attenuation important to extract accurate physical properties.

To model the effect of dust, we use two different attenuation laws for our SED fitting: the approach of Calzetti et al. (2000, henceforth, C00)and that of Charlot et al. (2000, henceforth, CF00). While these two attenuation laws are relatively simple, they differ in how to attenuate a given stellar population.

The attenuation curve of C00 was tuned to fit a sample of starbursts in the local Universe. This curve attenuates a stellar population assuming a screen model:

$$k(\lambda) = \frac{A(\lambda)}{E(B-V)}, \tag{3.2}$$

where k(λ) is the attenuation curve at a given wavelength λ, A(λ) is the extinction curve, and E(B-V) is the color excess, which is the difference between the observed B-V color index and the intrinsic value for a given population of stars. Despite its simplicity, this attenuation curve, with its modifications, is widely used in the literature (e.g. Burgarella et al., 2005; Buat et al., 2012; Małek et al., 2014, 2017; Pearson et al., 2017; Buat et al., 2018; Elbaz
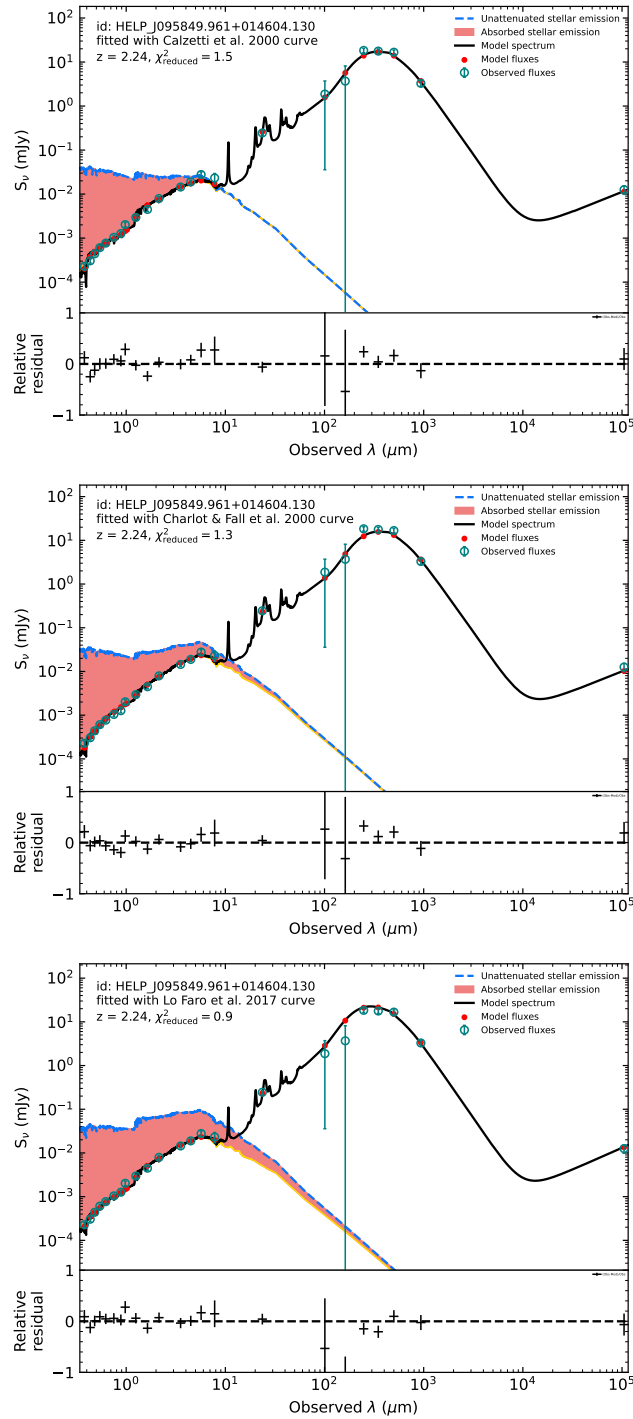
FIGURE 3.5: Computed SEDs of a galaxy from our sample (HELP − J095849.961 + 014604.130) fitted with three different attenuation laws, shown from left to right: Calzetti et al. (2000), Charlot et al. (2000), and Lo Faro et al. (2017). The χ^2 of every fit is shown on the figures. Red-filled area represents the attenuated stellar light.

et al., 2018; Ciesla et al., 2020). However, it does not always succeed in reproducing the UV extinction of galaxies at higher redshifts (Noll et al., 2009; Lo Faro et al., 2017; Buat et al., 2019).

Another approach is to also consider dust present in birth clouds. This is the core of the

attenuation curve of CF00. In this approach, dust is considered to attenuate the dense and cooler molecular clouds (hereafter MCs) differently than ambient diffuse interstellar media (ISM). This configuration is expressed by the following analytical expression:

$$A(\lambda)_{\text{ISM}} \propto \left(\frac{\lambda}{\lambda_V}\right)^{\delta_{ISM}} \text{ and } A(\lambda)_{\text{MC}} \propto \left(\frac{\lambda}{\lambda_V}\right)^{\delta_{MC}}, \tag{3.3}$$

where δ_{ISM} and δ_{MC} are the slopes of attenuation in the ISM and the MCs, respectively. Young stars that are in the MCs will therefore be attenuated twice: first by the surrounding dust and additionally by the dust in the diffuse ISM. A ratio of $Av_V^{ISM} / (A_V^{BC} + A_V^{ISM})$ is also believed to account for the attenuation of young stars residing in the birth clouds, and the older stars residing in the ISM.

In CF00, it was found that $\delta_{ISM} = \delta_{MC}$ = -0.7 satisfied dust attenuation in nearby galaxies, however, this curve is frequently used at higher redshifts (e.g., Buat et al., 2018; Małek et al., 2018; Pearson et al., 2018; Salim et al., 2020). By attenuating at higher wavelengths (until the NIR) more efficiently than C00, this approach considers a more attenuated older stellar population.

Lo Faro et al. (2017, henceforth, LF17) have found that a shallower attenuation curve reproduces the attenuation in ultra-luminous and luminous IR galaxies (ULIRGs and LIRGs) at z~2. For their sample, LF17 found δ_{ISM} = -0.48. This curve was used in Hamed et al. (2021) for a heavily dust-obscured ALMA-detected galaxy at z~2. It provides an overall better fit than other steeper attenuation laws.

To model dust attenuation of the galaxies of our sample, we used the aforementioned laws, with the parameters presented in Table 4.2. The mean normalized attenuation of our sample as a result of the three attenuation curves are shown in Fig. 3.3 (left panel). To obtain the results shown in the left panel of Fig. 3.3, we computed the attenuation values in the UV-NIR bands. Then we averaged the attenuation in each band for the whole sample. The curve of C00 is steeper than the double-component power-laws of CF00 and LF17, especially in the NIR domain.

Hot and cold dust components

Dust grains heated by AGN, along with the vibrational modes of polycyclic aromatic hydrocarbons (PAHs), dominate the MIR part of the SED of a galaxy. Thus, it is important to include AGN modeling in our SED fitting procedures, as well as to take into account PAH's contribution to the overall dust emission. Our initial analysis of the IRAC photometry of *Spitzer* did not suggest AGN candidates. We also included AGN-heated dust templates of Fritz et al. (2006) in our SED fitting procedure, but found no AGN contribution in our sample.

To model the IR emission in our SED models, we use the templates of Draine et al. 2014. These templates take into consideration different sizes of grains of carbon and silicate, thus allowing for different temperatures for the dust grains. These templates rely on observations and are widely used in the literature to fit FIR SEDs.

3.4.3   SED quality, model assessment

In assessing which SED provides the best fit for modeling the galaxies of our sample, we adopted a similar methodology to that of Buat et al. (2019). We compare the reduced χ^2 of the resulting fits with the three attenuation recipes used, and in the case of different attenuation laws providing a good reduced χ^2, we checked the Bayesian inference criterion (BIC) defined as $BIC = \chi^2 + k \times ln(N)$, where k is the number of free parameters and N is the
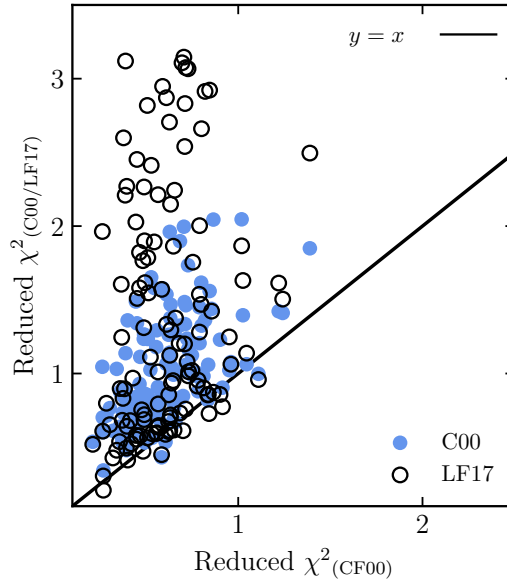
FIGURE 3.6: Comparison between reduced χ^2 of the mock sample obtained with CF00, C00, and LF17 attenuation laws.

number of data points. The mean reduced χ^2 was found to be 2.4 for our sample (Fig. 3.4 left panel, where we show the reduced χ^2 for the best fits of our sample).

To test the robustness of the method we use to select the best attenuation law for each galaxy, we performed the following test: We first fit all galaxies of our sample with the attenuation law of CF00. We then take the best fit values for each filter of each galaxy. Next, we perturb these "best" fluxes (obtained from the fit) using the initial photometry errors to obtain a mock catalog.

This mock catalog was then fitted with: Calzetti law, CF00 law, and LF17 law, in the same way, that the initial real photometry was treated. The reduced χ^2 obtained from those fits are then compared for each source. We show this comparison in Fig. 3.6. The obtained reduced χ^2 for CF00 fits of the mock sample are consistently smaller than that obtained using the two other attenuation recipes. Precisely, 93% of mock galaxies preferred CF00 attenuation law using this test. The other 7% had a reduced χ^2 of ~0.1 lower using the other attenuation laws.

The choice of the best attenuation law that better describes the observed fluxes is crucial for our study. Therefore we used an additional method to reliably attribute the best attenuation law for each galaxy. We introduced perturbations to the fluxes by applying a Gaussian distribution with a standard deviation that corresponds to the uncertainties of each band. To make the calculation time faster – and since the main task was to check the reliability of the best attenuation law for each galaxy – we generated mock fluxes until the mid-IR bands of IRAC. We created ten mock catalogues with this method, and applied the same approach of SED fitting for our original sample to the mock samples. Figure 3.7 shows the ratio of mock fluxes to real fluxes of our sample.

The results of these tests are presented in Table 3.4, where the vast majority of our mock galaxies (> 94%) preferred the same attenuation law of the initial real galaxies. This shows that the usage of the reduced χ^2 in assessing the best attenuation law in our case is valid. This is directly linked with the good S/N ratios of our photometric data, which were shown in Tab 3.1.
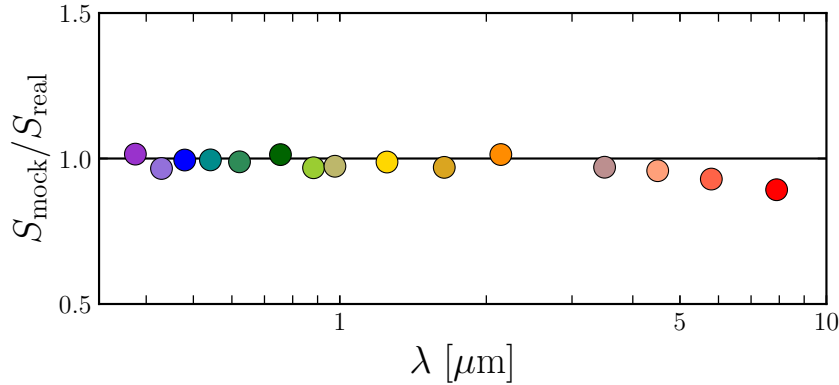
FIGURE 3.7: Ratio of mock fluxes to real fluxes of our sample. The mock fluxes were obtained with perturbations to the initial fluxes of our sample by employing a Gaussian distribution with the standard deviation equal to the errors associated with each flux of every source. This process was repeated ten times to generate ten mock galaxy samples. This figure shows the ratio of the average perturbed fluxes to the fluxes of the real sample.

TABLE 3.4: Summary of the results of the best fits using the same SED method on the fluctuated photometry preferring the same attenuation law (average of ten realizations) and the best attenuation laws for the real galaxies.

RealMock	C00	CF00	LF17
C00	94%	5%	1%
CF00	0%	97%	3%
LF17	0%	3%	97%

An example of a computed SED of our sample is given in Fig. 3.5, where we attenuated the same galaxy in three different ways. In this example, the shallower attenuation of Lo Faro et al., 2017 was preferred since it provided a significantly better fit. To test the reliability of our SED models, using `CIGALE` we generated a mock galaxy sample and fitted SEDs with the same methods applied to our sample. We show the comparison between the real physical properties that we derived for our sample and its mock equivalent in Fig. 4.4.

3.5 Results and discussion

3.5.1 Galaxy properties and dust attenuation

We applied a broad range of attenuation slopes in fitting our sample of DSFGs. The attenuation curve of C00 results in lower stellar masses compared to the ones obtained with the shallower double component attenuation laws of CF00 and LF17 (with a mean stellar mass of $10^{10.87}$ M$_\odot$ for C00, $10^{11.22}$ M$_\odot$ and $10^{11.52}$ M$_\odot$ for CF00 and LF17, respectively). The distribution of the obtained stellar masses was shown in Fig. 3.3 (right panel), with the mean M$_*$ for the whole sample portrayed for every attenuation law used. Stellar masses computed using shallower attenuation slopes are higher than the one produced with steeper curves.

Star formation rates computed from the panchromatic SED fitting using the three aforementioned attenuation laws do not change, which is similar to what was found by Małek

et al. (2018). The mean values of the $\log_{10}(SFR)$ of the sample fitted with C00, CF00, and LF17 are 2.75, 2.63, and 2.60 $M_\odot$ yr^{-1}, respectively, which is of a similar range of galaxies studied in Buat et al., 2019. The dust masses computed with the three attenuation laws are invariant (with a mean of 1.80×10^9 $M_\odot$ for the whole sample). This is mainly due to the strong constrain of the FIR part of the SED provided by the ALMA detections as well as the good fitting of the spectrum.

The significant difference in produced stellar masses using the different attenuation law slopes result in a clear distinction in the "starburstiness" of galaxies and also affects the quiescent systems (Lo Faro et al., 2015). In our sample, the number of starburst galaxies decrease with a shallower attenuation curve (60% for C00, 25% for CF00, and 14% for LF17). Despite its simplicity, the attenuation law given by Calzetti et al. (2000) provided good fits in building the SEDs and was favored over the shallower curves of Charlot et al. (2000) and Lo Faro et al. (2017) in 49% of the whole sample, that is, 61 sources (by comparing the resulting reduced χ^2). This was mainly noticed below redshift of $z = 2$. The attenuation curve adapted by Lo Faro et al. (2017) provided better fits for 38 galaxies in total, but 79% of these galaxies fell in the redshift range of $1.5 < z < 2.5$, which supports the initial tuning of the ISM attenuation at -0.48 (Lo Faro et al., 2017).

We show the preference of the attenuation laws for our sample based on the V band attenuation and the SFR in Figs. 3.8 and 3.9, respectively. We find no clear correlation between the attenuation in the V band and the preference of the attenuation laws in our sample. We also checked the correlation with the stellar masses. However, since these masses are directly a byproduct of the attenuation law used (as shown in Fig. 3.3), we cannot tell if this correlation is physical. Galaxies that are preferring CF00 double-component attenuation law and its shallower version LF17, by construction, result in a significantly higher older stellar population, therefore increasing the stellar mass (e.g., Małek et al., 2018; Buat et al., 2019; Hamed et al., 2021; Figueira et al., 2022).

We also checked the preference of attenuation laws used with SFR for our galaxies. This is shown in Fig. 3.9. We found that towards higher SFRs, there are no preferences in attenuation laws for our sample. However, in the lower limit of SFR, a double-component attenuation was slightly preferred, but still within the error bars. In the sample, we had only 18 galaxies with $\log(SFR) < 2.4$ and 38% of them were fitted with C00 while the rest preferred CF00/LF17. The small statistics at this lower end of SFR for our sample does not allow us to make a strong statement about the correlation of the attenuation laws for low-SFR galaxies.

3.5.2 Stellar vs. dust components

To analyze the energy balance of our sample of DSFGs, especially taking into consideration the available dust and stars emission and images, we followed the method introduced in Małek et al. (2018) and Buat et al. (2019), namely, by dissecting the stellar continuum of our sample of galaxies without taking into account the FIR detections. Equivalently, we also fit the FIR continua of our SFGs.

To model the stellar continuum, we use the photometric bands of CFHT, *Subaru*, *VISTA*, and available IRAC bands. This was done in order to ensure the attenuation curve requirements without adding the energy balance constraint to the global SED fitting method. As shown in, for instance, Buat et al., 2019 and Hamed et al., 2021, the dichotomy between the stellar SED and its dust counterpart is important in testing the validity of the energy balance concept that is the basis of most of panchromatic SED fitting tools. Moreover, this method is critical in cases where the dust continuum maps are not centered on their short-wavelength
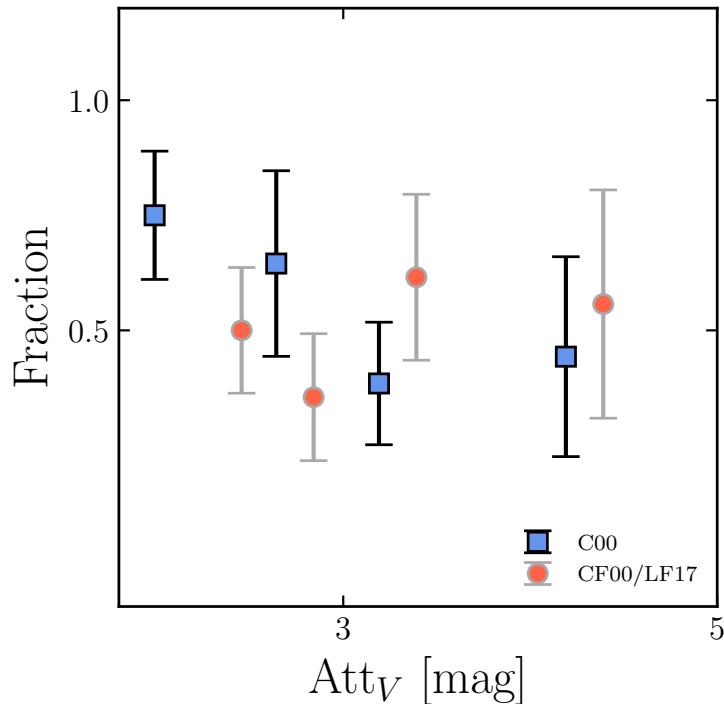
FIGURE 3.8: Preference of attenuation laws of our sample according to the attenuation in the V band. To facilitate the reading of this plot, we shifted the bins of CF00/LF17 slightly to the right (+0.1).

counterparts. When fitting the short wavelength part of the SEDs, we model the stellar light taking into account the delayed SFH boosted by a recent burst, a stellar population library of Bruzual et al. (2003), and dust attenuation laws that (discussed in Sect. 4.4). We also modeled the IR emission using Draine et al. (2014) dust emission templates, but without taking into account the IR photometry, allowing the energy balance to dictate dust luminosities and masses based on the amount of the stellar light that is attenuated. Overall, 61% of our sample (75 sources) provided better fits with the simple power law of C00, whereas a shallower attenuation was needed to reproduce the spectra with the lowest χ^2 for the rest (14% with CF00 and 25% with an even grayer LF17 slope).

The steep law of C00 provided better fits for more galaxies when taking into account the stellar emission only. This result was also found in Buat et al. (2019) for a smaller sample. This tendency will be confirmed in future studies based on the new generation of IR datasets from JWST and well-constrained short-wavelength counterparts from LSST.

Equivalently, we estimated dust luminosities based on the rest frame UV to NIR photometry of our sample, assuming an energy balance between dust absorption and dust emission. We compared these IR luminosities with the ones calculated from the IR photometric points with templates from Draine et al. (2014) . The results are shown in Fig. 3.10.

We confirm the scatter initially found in Buat et al. (2019) and Hamed et al. (2022) with dust-rich galaxies, which significantly differs from the normal SFGs found in Małek et al. (2018). We find that the dust emission evoked from a pure energy balance based on the short wavelength does not always explain the one calculated from the FIR photometry. Galaxies that are fitted with C00 attenuation law are found to inhibit more attenuation and they produce higher L_{IR} from their dust content rather than the stellar parts. The star-to-dust compactness
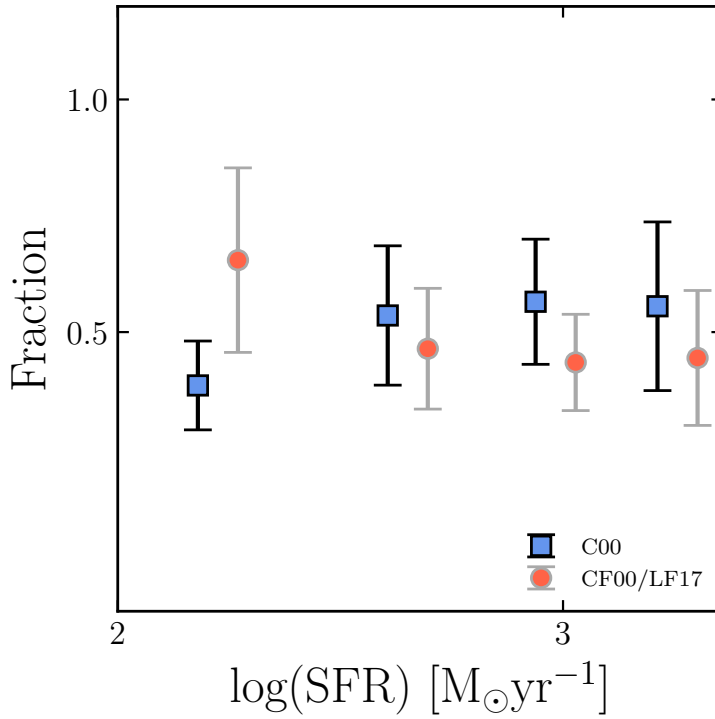
FIGURE 3.9: Preference of attenuation laws of our sample according to the SFR. To facilitate the reading of this plot, we shifted the bins of CF00 and LF17 slightly to the right (+0.1).
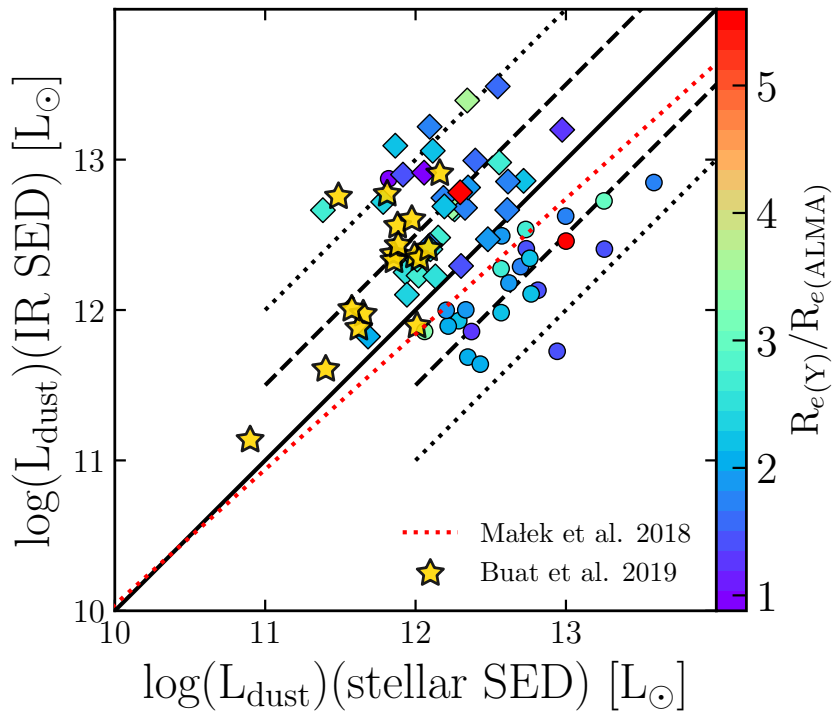
FIGURE 3.10: Infrared luminosities of our sample produced from the IR data alone using the Draine et al. (2014) dust emission templates (*y*-axis) with respect to the IR luminosity evoked indirectly through the energy balance based on the short wavelength data only.

did not seem to play a role in this trend. This shows that the dust luminosity values drawn from the direct and attenuated UV photons based on the energy balance are not enough to reproduce the dust luminosity observed from the actual IR photometry.

3.5.3 Dust attenuation and sizes

We studed the effects of star-to-dust compactness of the unobscured star-forming regions and the stellar population emission to the extent of dust emission detected by ALMA. We defined the ratio of the short wavelength radii to their FIR counterparts as $R_e(UV)/R_e(ALMA)$, where $R_e(UV)$ is the circularized effective radii measured from the HSC Y bands of our sources. The UV radii of our sample decrease with redshift, while the ALMA counterparts are rather constant across the studied redshift range in this work. This is shown in Fig. 3.11 and is explained by the bright IR ALMA-selected sources, and their active star-forming/stellar population regions.
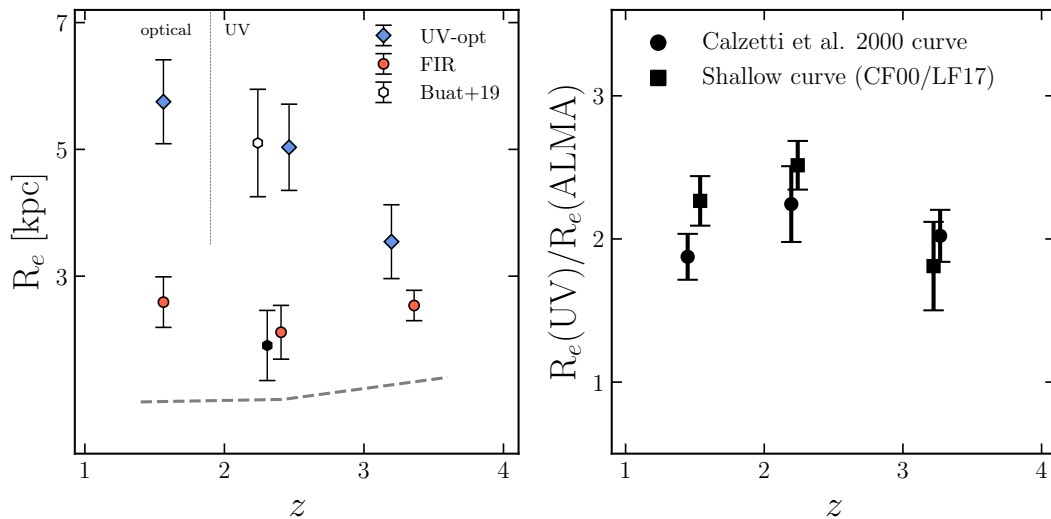
FIGURE 3.11: Redshift evolution of the derived effective radii at two different wavelengths of our sample. The dashed line represents the redshift at which the Y band starts to probe the restframe UV (left). Hexagons show the binned sample of 17 galaxies from Buat et al. (2019) around $z \sim 2$, taken from Elbaz et al. (2018) and Dunlop et al. (2017). Empty hexagons show the rest-frame UV radii while the filled ones show the ALMA detection. The dashed line shows the minimal size that can be measured with ALMA (Gómez-Guijarro et al., 2022). The evolution of $R_e(UV)/R_e(ALMA)$ ratio with redshift in our sample of DSFGs is shown on the right.

Despite the fact that the attenuation curve of Calzetti et al. (2000) managed to fit the largest sub-sample of our DSFGs around the cosmic noon and at lower redshift ranges, the distribution of these galaxies for which a steeper attenuation curve provided the best fit is relatively compact. A relative star-to-dust compactness was found to have an average of 1.7, while for the shallower attenuation curve recipes were found to not follow a specific preference and they are rather scattered across all the studied redshift bins. We show the redshift distribution of the preferred attenuation laws in Appendix 3.7.2. The range of the resulting ($n^{Sérsic}$) was too small (0.4 to 1.6), and in that narrow range we did not find any correlation with other observables. We find that the ratio of $R_e(UV)$ to $R_e(ALMA)$ changes accross the redshift in our sample of ALMA-detected DSFGs. This distribution is found to peak at
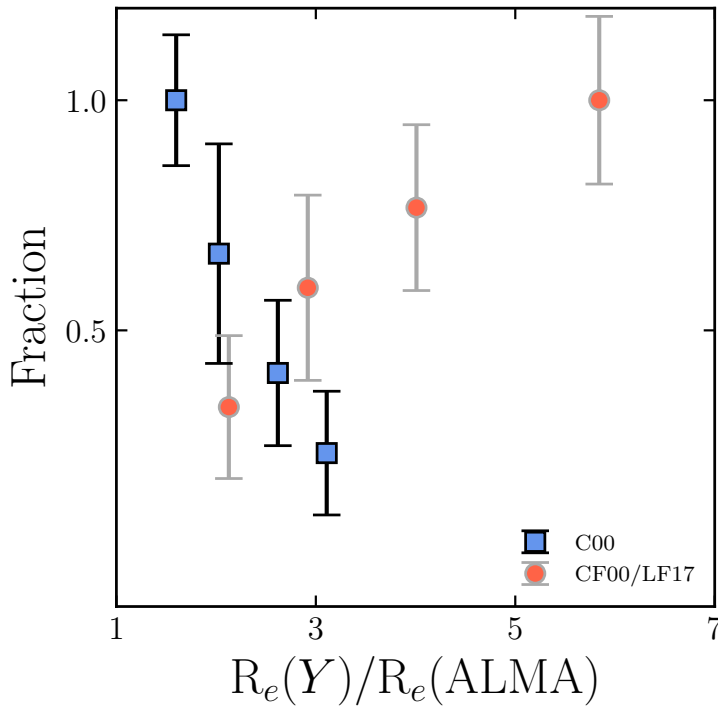
FIGURE 3.12: Preference of attenuation laws of our sample according to the star-to-dust compactness. To facilitate the reading of this plot, we shifted the bins of CF00/LF17 slightly to the right (+0.1).

$z = 2$ around the cosmic noon (as shown in the right panel of Fig. 3.11). This change is more prominent at higher redshift with the decrease of the star-to-dust compactness is directly connected to the rapidly decreasing rest-frame UV sizes of these DSFGs at higher redshift. This might be explained by the more intense star formation around that cosmic epoch, especially that DSFGs contributed significantly to the total star formation activity in the Universe. Moreover, this peak is found to be stronger for galaxies that require a shallower attenuation curve. This might correlate with the higher need of cold star forming regions in these galaxies to explain the higher SFRs. This result shows that dust attenuation and the star-to-dust compactness of dust in DSFGs might be correlated with the cosmic SFR density.

These findings partly agree with the smaller sample size studied in Buat et al. (2019). However, our statistically larger sample size allows for an extrapolation of this correlation not only at different redshift ranges, but also showed that shallower attenuation curves do not favor higher star-to-dust compactness, but rather a scattered trend was found, unlike the steeper curves which clearly preferred relatively smaller $R_e(UV)/R_e(ALMA)$ (~ 2) at different redshift ranges. One possible explanation for this can be the fact that for galaxies with relatively smaller sizes of their unobscured star-forming regions and their dust content might be translated by a screen model of attenuation, due to a non-effective mixing of stars and dust. On the other hand, a very compact dust emission requires a more complex mixing of dust and stars which is translated in a shallower attenuation curve. A correlation is visible between the fraction of our sample that is fitted with a specific attenuation law and the relative compactness, as we show in Fig. 3.12.

We find that the galaxies with smaller optical and UV sizes relative to dust radii largely prefer the C00 attenuation law in our sample. For larger $R_e(Y)/R_e(ALMA)$ ratio (>3) only

CF00 and its shallower modification LF17 fitted the galaxies better. This shows that taking relative compactness into account is highly important when performing SED fitting. We can infer the most likely attenuation law for a given galaxy by taking into account its sizes in the unattenuated SF region and the dust continuum. This, in turn, enables a reliable procedure for fitting its SED.
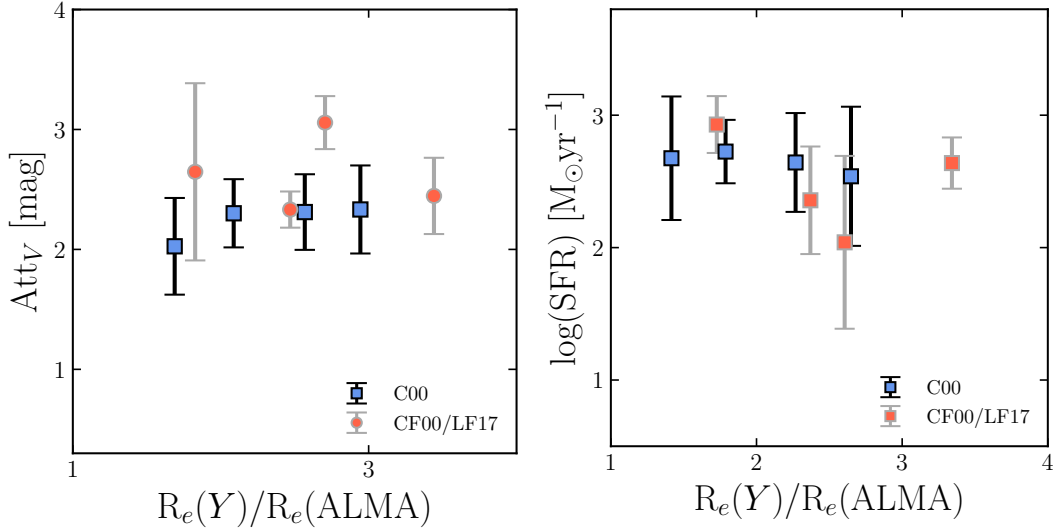
FIGURE 3.13: Variation in the V band attenuation (left) and in the SFR (right) with star-to-dust compactness.

3.6   Summary

In this paper, we studied a statistical sample of 122 DSFGs that are not host to AGN, across a wide range of redshift ($1 < z < 4$). We derived their circularized effective radii in two different bands, HSC's Y band when available, and, equivalently, their dust components' radii with ALMA detections. On the other hand, we carefully analyzed their SEDs, modeling them with varied dust attenuation laws, particularly that of Calzetti et al. (2000) and the shallower curves of Charlot et al. (2000) as well as their recipes.

We also dissected the stellar SEDs alone and their IR counterparts (as in, e.g., Buat et al., 2019; Hamed et al., 2021) to investigate the validity of the energy balance when taking into account the ALMA detections of our sources. We found that even if most of our sources seem to produce the same dust emission when relying on an energetic balance from the short wavelengths (and when fitting the IR photometry separately), some galaxies expressed dimmer star formation when the Calzetti et al. (2000) attenuation law was favored. This was translated into an under-supply of dust emission from the stellar population alone.

We found that knowing the information of the sizes of DSFGs (especially their stellar and dust contents) in the analysis constrains the used attenuation curves to fit the photometry of these galaxies. We found that a starburst curve of Calzetti et al. (2000) was favored in the reproduction of the SEDs of DSFGs with comparable star-to-dust radii ratios, precisely at $1.2 < R_e(UV)/R_e(ALMA) < 2.5$. However, despite the seemingly irrelevant star-to-dust ratios with the attenuation curves of Charlot et al. (2000) and the shallower version (Lo Faro et al., 2017), we found that compact dust emission and extended stellar radii needed shallow curves and double exponential attenuation laws to account for the missing photons absorbed

by dust. This shows that when fitting SEDs using broad band photometry, a careful analysis of the radii of different components should be taken into account, before using a unique attenuation law which will result in wrongly estimated stellar masses.

We stress that recent ALMA studies of smaller samples of z~2 galaxies suggested that compact IR sizes could be connected to rapid growth of supermassive black holes during the SMG star formation phase (Ikarashi et al., 2017). Semi-analytical models (i.e., Lapi et al. 2018) have predicted that such sources would experience ongoing or forthcoming AGN feedback, which is thought to trigger the morphological transition from star-forming discs to early-type galaxies. However, our galaxies do not show AGN activity, and are suggestive of SF galaxies caught in the compaction phase characterized by clump or gas migration toward the galaxy center, where highly intense dust production takes place and where most of the stellar mass is accumulated (Pantoni et al. 2021b and Pantoni et al. 2021a). Interestingly, the dust compaction phase is suggested to play role in metallicity enrichment efficiency, which further affects dust growth in ISM (Pantoni et al., 2019; Donevski et al., 2020). We expect that our dusty galaxies have relatively wide range of gas metallicities and dust growth efficiencies, which would reflect on different attenuation slopes, rather than favoring the single one. This expectation is also in line with results from recent cosmological simulations that found dependence of attenuation on dust compactness and/or geometry (e.g., Schulz et al., 2020) as well as on the ratio between the small and large dust grains (e.g., Hou et al., 2019).

In our sample, we have observed that the C00 attenuation law is mostly favored by galaxies with opt/UV sizes that are two times as large than the dust radii. However, for galaxies with $R_e(Y)/R_e(ALMA) > 3$ the CF00 (and its shallower modification LF17) was found to provite a better fit. These findings suggest significant importance of considering the relative compactness when conducting SED fitting. By taking into account the sizes of a galaxy in the unattenuated SF region and the dust continuum, we can deduce the most probable attenuation law for that galaxy, thus providing a dependable approach for fitting its SED.

We conducted a test to ensure that the trend observed between the preferred attenuation law and relative compactness is not influenced by other physical properties. Specifically, we investigated the potential relationship between the relative compactness and two other properties: attenuation in the V band and SFR (Figs. 3.8 and 3.9). Figure 3.13 presents the results of this analysis. We find no significant correlation between these properties and relative compactness. This finding supports the conclusion that the observed trend between relative compactness and preferred attenuation law can be robust and not influenced by these physical properties.

We find that the star-to-dust compactness of the unobscured star-forming regions and stellar population regions to dust emission of these DSFGs peaks around the cosmic noon (z~2). This is especially notable at higher redshifts. A possible correlation might be with the cosmic SFR density for which the DSFGs were a major contributor in the early Universe. These results are promising in the era of highly resolved deep-field detections with the LSST and JWST, where dust attenuation and size measurements are becoming more precise. Combining these detections with the FIR information, especially with ALMA, is unparalleled when dealing with the dust attenuation curve problem at different redshift ranges.

3.7 Appendices

3.7.1 Choice of SFH and its parameters

We tested several SFH models in order to find a proper set of templates that are not only able to fit the data, but that also are physically motivated. Those models include the simple delayed SFH, which did not succeed in fitting the photometry of the majority of our sample. We therefore added an exponential recent burst. This delayed SFH with an exponential burst fitted the UV part of our SEDs the best (provided significantly better reduced χ^2). We also tested the need to include a recent quench episode in our models, by using a truncated SFH (Ciesla et al., 2017) that allows a recent burst or a recent quench episode. This was motivated by previous studies that suggested that SFGs can have significantly low molecular gas masses and therefore might be experiencing a drop in their star formation activity (e.g., Elbaz et al., 2018; Falkendal et al., 2019; Hamed et al., 2021) and rapidly transitioning to the red sequence.

The truncated SFH did not provide any improvement of the SEDs nor did it change the estimated stellar masses and the SFRs, and there was no evidence of recent quenching episode for the whole sample. Our analysis suggests a strong dependence of the instantaneous SFR on the choice of the age of recent burst episodes. This was characterized in extremely huge values of derived SFRs (>10000 M$_\odot yr^{-1}$) for some of our galaxies when a lower value of burst age was preferred (<5 Myr). Hence, we chose a lower limit of the recent burst of 5 ± 1 Myr.

3.7.2 Redshift distribution of attenuation preference

In Fig. 3.14, we show the distribution of the relative compactness distribution of our sample based on the preferred attenuation law for each galaxy – even though the C00 attenuation curve seems to fit the sample better when the R$_e$(Y)/R$_e$(ALMA) $\sim$ 2. However, shallow attenuation curves do not seem to have a redshift preference. Despite the fact that we have a large sample that covers a wide redshift range, our sample did not cover a wide range statistically in terms of star-to-dust compactness.

3.7.3 Size evolution with physical properties

Here, we show the evolution of the derived effective radii of DSFGs with the physical properties of DSFGs, in particular, their dust luminosities and the stellar masses. The calculated radii using the two measured bands (when available) seem to be constant at different L$_{IR}$ (Fig. 3.15) and stellar masses (Fig. 3.16) These results agree with Fujimoto et al. (2017), although the mean value of FIR effective radii of our sample are ~16% higher than that of Fujimoto et al. (2017). This difference is due to the different method in calculating these radii in the *uv* planes, the angles of their fits are similar to the values given the literature at different redshift ranges. Our results also show that $R_{e_{(FIR)}}$ are smaller than $R_{e_{(UV,opt)}}$ for SFGs (Ichikawa et al., 2012; Fujimoto et al., 2017).
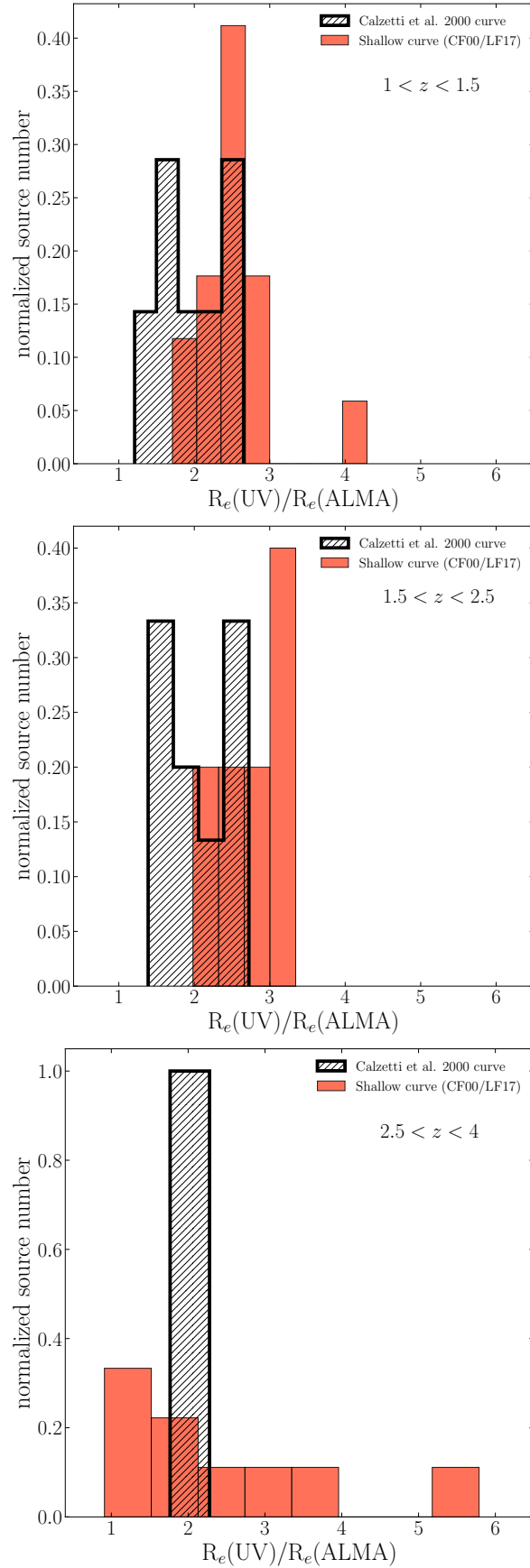
FIGURE 3.14: Histogram of the ratio of HSC's *Y* band radius to the ALMA radius. The red-filled histograms at different redshift ranges represent galaxies for which a shallow attenuation curve of CF00 or LF17 was critical in order to reproduce the observed stellar light and resulted in better fits. The dashed histogram shows galaxies for which the C00 attenuation curve gave a satisfying fit.
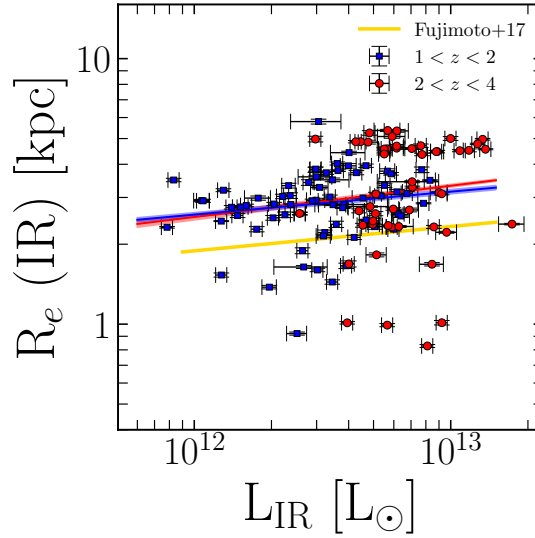
FIGURE 3.15: Effective radii of the UV and ALMA detections of our sources, with respect to the IR luminosities obtained from the best fits using `CIGALE`. The yellow line shows the trend found in Fujimoto et al. (2017).
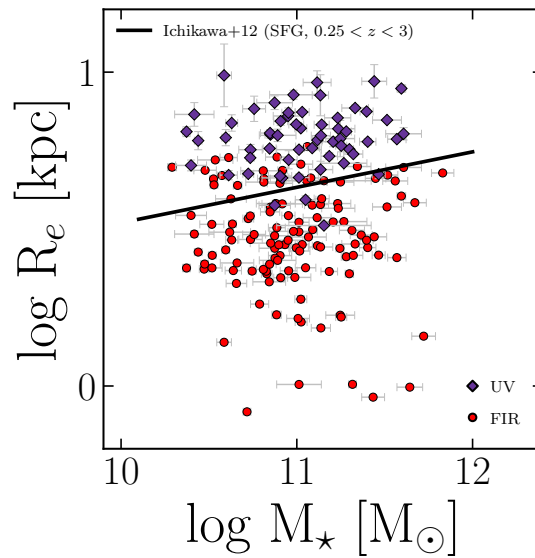
FIGURE 3.16: Effective radii of the UV and ALMA detections of our sources, with respect to the stellar masses obtained from the best fits using `CIGALE`.

3.7.4 CIGALE mock analysis

In Fig. 4.4, we show the mock analysis of the physical parameters generated by `CIGALE`, as well as the input parameters that we used in the SED fitting technique.
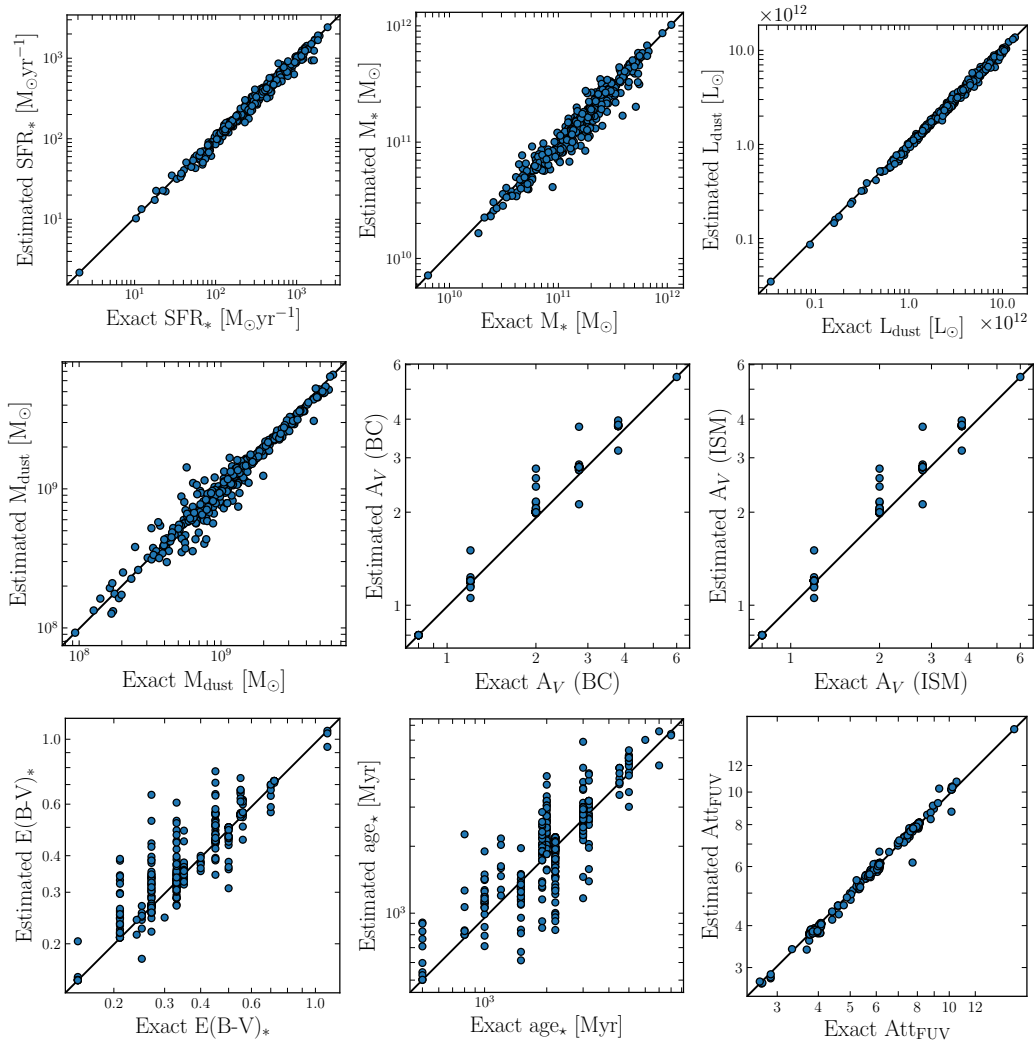
FIGURE 3.17: Comparison between the true parameters of the mock SEDs and the results from the SED modeling with CIGALE (from top left panel) for the SFR, stellar mass (M_*), dust luminosity (L_{dust}), dust mass (M_{dust}), attenuation in the V band (Att_V) of the birth clouds and the ISM, color excess (B-V), age of the main stellar population ($age_\star$), and the attenuation in the FUV (Att_{FUV}). A parameter is considered to be well estimated and constrained when there is a one-to-one relation between the two.

Summary of the third chapter

- In this work, the largest sample of dusty star-forming galaxies was studied from the aspect of dust attenuation. These galaxies have ALMA detections of their dust continua and their rest-frame UV/optical wavelengths detected with HSC *Y* band. This makes it the perfect sample to study dust attenuation and morphological extensions of dusty star-forming galaxies.

- This study analyzed the spectral energy distributions of dusty galaxies and modeled them with different dust attenuation laws. The attenuation laws used were that of Calzetti et al. (2000) and Charlot et al. (2000), along with the shallower version of the latter, as proposed by Lo Faro et al. (2017).

- This study found that knowing the sizes of dusty star-forming galaxies is important for selecting the appropriate attenuation curve to fit their photometry. More precisely, knowing the relative spatial extent of the emission coming from the stellar population/star-forming regions, to that of the dust, is crucial in determining the dust attenuation curve.

- A starburst curve of Calzetti et al. (2000) was favored for galaxies with relatively compact star-to-dust radii ratios. Compact dust emission and extended stellar radii needed shallow curves and double exponential attenuation laws to account for the missing photons absorbed by dust.

- The star-to-dust compactness of the unobscured star-forming regions and stellar population regions to dust emission of these dusty star-forming galaxies peaks around the cosmic noon ($z \sim 2$).

- The study investigated the energy balance between the stellar emission and their infrared counterparts. Most of the sources produced the same dust emission when relying on an energetic balance from short wavelengths. Some galaxies expressed dimmer star formation when the Calzetti et al. (2000) attenuation law was used.

- These results are promising in the era of large surveys of deep field observations of JWST and the upcoming LSST. With highly-resolved high redshift observations in the short and mid infrared wavelengths, one could generalize these findings over a larger statistical sample of galaxies.

4

Decoding the IRX-β dust attenuation relation in star-forming galaxies at intermediate redshift

4.1   Abstract

We aim to understand what drives the IRX-β dust attenuation relation at intermediate redshift ($0.5 < z < 0.8$) in star-forming galaxies. We investigate the role of various galaxy properties in shaping this observed relation. We use robust [O II] $\lambda3727$, [O III] $\lambda\lambda4959, 5007$, and Hβ line detections of our statistical sample of 1049 galaxies to estimate the gas-phase metallicities. We derive key physical properties that are necessary to study galaxy evolution such as the stellar masses and the star formation rates using the spectral energy distribution fitting tool CIGALE. Equivalently, we study the effect of galaxy morphology (mainly the Sérsic index n and galaxy inclination) on the observed IRX-β scatter. We also investigate the role of the environment in shaping dust attenuation in our sample. We find a strong dependence of the IRX-β relation on gas-phase metallicity in our sample, and also a strong correlation with galaxy compactness characterized by the Sérsic indexes. A less strong correlation is seen with stellar masses, specific star formation rates, and the stellar ages of our sources. Metallicity is one of the drivers of the dust attenuation scatter, this also results from the older stars and higher masses at higher β values. The correlation with specific dust mass is strong in shifting the galaxies away from the IRX-β relation towards lower β values. We find that more compact galaxies witness a larger amount of attenuation than less compact galaxies. There is a subtle variation in the dust attenuation scatter between edge-on and face-on galaxies, but the difference is not statistically significant. Galaxy environments do not significantly affect dust attenuation in our sample of star-forming galaxies at intermediate redshift.

4.2   Introduction

Extragalactic astronomy witnessed major development in the last few decades with regard to observation and understanding of the physical and chemical processes that control the evolution of galaxies. This understanding was a result of interpreting the ever-growing plethora of panchromatic data, that provided unprecedented constraints on the interplay between the

different components that galaxies exhibit. With powerful infrared (IR) telescopes such as the *Herschel* Space Observatory, it has become possible to better constrain the direct and indirect stellar emission of galaxies at higher redshifts, expanding our knowledge beyond the highly-resolved local Universe.

In complex systems like galaxies, different components interact with each other on different timescales. Such interaction includes the interplay between stars and dust, which influences the total spectra of galaxies. Dust affects the shape of the spectral energy distribution (SED) like no other component, despite its low contribution to the overall mass of the baryonic matter. Interstellar dust absorbs a significant amount of the ultraviolet (UV) and optical radiation, heats up and re-emits it at longer wavelengths, mostly in the far-infrared (FIR). As a consequence, part of the stellar UV emission gets extinct, making it necessary to account for the missing radiation especially when estimating key properties that describe the evolution of galaxies such as star formation rates (SFRs). The derivation of SFR should rely on both UV-optical measurements and on the FIR emission (e.g., Blain et al., 2002; Chapman et al., 2005; Takeuchi et al., 2005; Hopkins et al., 2006; Madau et al., 2014; Magnelli et al., 2014; Bourne et al., 2017; Whitaker et al., 2017; Gruppioni et al., 2020). Dust attenuation laws are used to correct the absorption of the short wavelength photons in order to recover fundamental properties of galaxies. This is typically done by assuming certain dust distribution relative to the dimmed stellar populations. Attenuation laws rely on the well studied dust extinction in nearby galaxies (e.g., Calzetti et al., 1994, 2000; Charlot et al., 2000; Johnson et al., 2007), and they are widely applied when reproducing the UV-optical spectra at different redshifts (for an extensive review on attenuation laws see Salim et al., 2020).

At higher redshifts, the challenging measurements of FIR emission are overpowered by the easily available rest-frame UV emission (e.g., Burgarella et al., 2007; Daddi et al., 2007; Bouwens et al., 2012). This in turn limits the wavelength range from which the physical properties are inferred, therefore, a correct understanding of physical processes that prevail in short wavelength domain, like dust attenuation, becomes critical. Calzetti et al. (1994) showed a correlation between the UV spectral slope β, which is indicative for attenuation, measured with different spectral windows, and the Balmer optical depth of local starburst galaxies. Using the same sample, Meurer et al. (1995) and Meurer et al. (1999) found a tight relation between the heavily-attenuated β and the IR excess (IRX) of galaxies defined as the ratio between the IR and UV luminosities (L_{IR}/L_{UV}). This became known as the IRX-β relation and it was well observed subsequently in numerous studies at low and high redshift (e.g., Overzier et al., 2011; Boquien et al., 2012; Buat et al., 2012; Takeuchi et al., 2012; Cullen et al., 2017; Calzetti et al., 2021; Schouws et al., 2021).

Ideally, such a relation can be used to infer the FIR luminosity and affiliated properties of galaxies from lone UV observations. However, outliers of the IRX-β relation were found in several samples at different redshift ranges (e.g., Casey et al., 2014; Álvarez-Márquez et al., 2016; McLure et al., 2018). These outliers are typically Ultra Luminous IR Galaxies (ULIRGs) and populate the region of higher IRX and lower β values. Moreover, in older works β tends to be biased towards lower values due to the underestimated UV fluxes from the small aperture of *International Ultraviolet Explorer* (IUE), and this relation was therefore revisited using the fluxes from the *Galaxy Evolution Explorer* (GALEX) (Takeuchi et al., 2010; Takeuchi et al., 2012), moving it to higher β. Furthermore, the interpretation of this relation is not fully understood, despite the numerous attempts that tried to unveil the factors upon which it relies. The attenuation curve used to reproduce the observed short wavelengths, as well as the dust geometry model used to attenuate, were found to strongly affect the IRX-β scatter (Boquien et al., 2009; Casey et al., 2014; Salmon et al., 2016). This non-universality of dust attenuation laws is a known feature of dust obscuration at different

redshift ranges (e.g., Kriek et al., 2013; Buat et al., 2018, 2019; Hamed et al., 2021). Other dependencies of the IRX-β relation are the age of stellar populations (Popping et al., 2017; Reddy et al., 2018), the molecular gas mass (Ferrara et al., 2017), and on gas-phase metallicity (Reddy et al., 2018; Shivaei et al., 2020).

The IRX-β relation was well studied in the local Universe and at high redshift. In this work, we aim to answer the key question of what drives the IRX-β relation at intermediate redshift for star-forming galaxies, putting the evolution of such relation in the context of galaxy evolution. We make use of robust metallicity estimations, galaxy morphological quantities, and other physical properties such as stellar mass, in order to understand the attenuation scatter and therefore better understanding this relation at intermediate redshift, an area that otherwise remains poorly studied.

This paper is structured as follows: in Section 4.3 we describe the data used in this work. In section 4.4 we discuss the SED fitting procedure and the derivation of key physical properties that govern galaxy evolution. In section 4.4.4 we discuss the quality of our SED fitting procedure. In section 4.6 we show the IRX-β relation of our sample with its fit. We derive the gas-phase metallicities of our sample and discuss its effect on the IRX-β scatter in section 4.5. In section 4.7 we discuss different physical properties that drive the IRX-β scatter, with the dependence on the galaxy environment in section . The conclusions are presented in section 4.9. Throughout this paper, we adopt the stellar IMF of Chabrier (2003) and a ΛCDM cosmology parameters (WMAP7, Komatsu et al., 2011): $H_0 = 70.4$ km s^{-1} Mpc^{-1}, $\Omega_M = 0.272$, and $\Omega_\Lambda = 0.728$.

4.3 Data

4.3.1 Spectroscopic data

The data used in this work are from the VIMOS Public Extragalactic Redshift Survey (VIPERS, Garilli et al., 2014; Guzzo et al., 2014; Scodeggio et al., 2018). VIPERS used the VIMOS spectrograph at the Very Large Telescope to measure redshifts for a statistical number of galaxies ($\sim$90 000) in a large field of a total of ~ 24 deg^2 at $0.5 \leq z \leq 1.2$. The VIPERS sample has a limiting magnitude of $i_{AB} \leq 22.5$ mag to maximize the signal-to-noise of the spectra and to select galaxies below $z = 1.2$ (Le Fèvre et al., 2003). Moreover, a color selection based on the u,g,r,i bands allowed the survey to focus on removing the galaxies below $z = 0.5$, with median redshift 0.7 (Guzzo et al., 2014).

Spectroscopic observations of VIPERS were collected using the low-resolution red (LR-Red) grism ($\sim$ 5500-9500Å) and a spectral resolution R $\sim$ 220 (Scodeggio et al., 2018). VIPERS data reduction was performed via a fully automated pipeline (Garilli et al., 2014). Redshifts were estimated using the EZ code (Garilli et al., 2010) based on the software and the visual inspection. The redshift quality flag, described in detail in Garilli et al., 2014 and Guzzo et al., 2014, has tentative (flag 1) to highly secure (flags 2 to 4, with at least 95% of confidence) redshift measurements.

For reliable redshift estimations (Scodeggio et al., 2018), we selected galaxies for which the redshift flag was $3.0 \leq z_{flag} \leq 4.5$, where the decimal part of the flag indicates the consistency with photometric redshifts. We also selected the VIPERS sample with a flag that provides measurements with high S:N the quality of the measurement of emission lines. This flag is a goodness of fit assessment (a thorough description is detailed in Figueira et al., 2022; Pistis et al., 2022). The flags of emission lines are well-checked to deliver good estimations of the line profile. This is done through certain criteria such as minimizing the distance between the peak of the fit and the brightest pixel, and constraining the fit amplitudes to not differ significantly from the observed emission (Pistis et al., 2022).
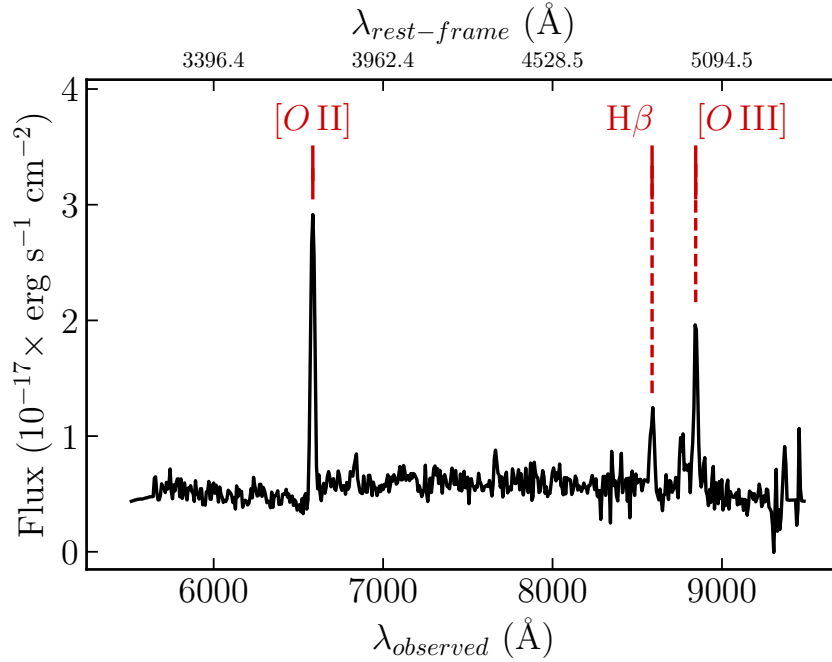
FIGURE 4.1: Spectrum of a source from our sample (VIPERS ID: 105161086; HELP ID: J021747.792-055145.509) at z_{spec} = 0.766, highlighting the [O II] $\lambda 3727$, [O III] $\lambda 4959, \lambda 5007$, and H$\beta$ lines.

TABLE 4.1: Signal-to-noise ratios of detected lines of our sample.

Line	Median S:N
[O II] $\lambda 3727$	21.79
Hβ	9.26
[O III] $\lambda 4959$	8.12
[O III] $\lambda 5007$	3.38

Finally, the Hβ line was corrected for stellar absorption following Hopkins et al. (2003):

$$S = \frac{EW + EW_C}{EW} \, F, \tag{4.1}$$

where S is the stellar-absorption-corrected line flux, EW is the equivalent width of the line, EW_C is the correction for stellar absorption, and F is the extinction-corrected line flux. We adopted an EW_C value of 2Å, which is commonly used in the literature (i.e., Goto et al., 2003).

We used the penalized pixel fitting code (pPXF) (Cappellari et al., 2004) to model the VIPERS spectra by fitting stellar and gas templates from the MILES library (Vazdekis et al., 2010), as described in Pistis et al. (in prep.). A single Gaussian was used to fit each emission line of the gas component, yielding integrated fluxes and errors. Table 4.1 shows the median signal-to-noise ratios (S:N) of the resulting four emission lines of our sample of galaxies. An example of the spectrum of a galaxy from our sample is shown in Fig. 4.1. Equivalent widths (EWs) and their errors were also computed.

4.3.2 Photometric data

The fields surveyed by VIPERS were previously mapped by the Canada-France-Hawaii Telescope Legacy Survey (CFHTLS), in the optical range, with the Wide photometric catalog T0007 release (Hudelot et al., 2012). The T0007 catalog with *ugriz* detections is an improvement of the initial T0005 and T0006 catalogs (Guzzo et al., 2014). In this newer catalog, the apparent magnitudes are given in the AB system, and were corrected for Galactic extinction, with an extinction factor derived at the position of each galaxy using the dust maps of Schlegel et al. (1998). Near-infrared magnitudes come from the *Ks* band detection of CFHT/WIRCam.

We required our sample to have detections in the FUV and NUV bands of the GALEX deep imaging survey. In the catalog of Moutard et al. (2016), GALEX data towards the CFHTLS-VIPERS fields were gathered, to measure the physical properties (e.g., SFR, stellar masses) of all galaxies in the VIPERS spectroscopic survey. The CFHTLS-T0007 maps were used as a reference to measure the Ks-band photometry, and the *u* band-selected sources were used as priors in estimating the redshift, as well as the FUV and NUV photometry.

Additionally, we extended the wavelength coverage to the FIR by cross-matching with the *Herschel* Extragalactic Legacy Project (HELP, Shirley et al., 2021) catalog, which provides unique statistical data of IR detection of millions of galaxies detected at long wavelengths with *Herschel*, constructed homogeneously. To achieve the HELP catalog, *Herschel* fluxes were estimated using XID+ pipeline (Hurley et al., 2017), a probabilistic deblender of SPIRE maps which takes into account the positions of sources detected with *Spitzer* at 24 μm (Duncan et al., 2018) from the Multiband Image Photometer (MIPS, Rieke et al., 2004). Detections from IRAC at its four channels from *Spitzer* were added to our data. We used data from the PACS instrument at 100 and 160 μm, and from SPIRE at 250, 350, and 500 μm.

4.3.3 Final sample

Apart from the redshift flag selection, as discussed in Section 4.3.1, we also restrain our sample to star-forming galaxies using the modified Baldwin, Phillips & Terlevich diagrams (BPT, Baldwin et al., 1981) by Lamareille (2010). This modified BPT diagram allows us to use the lines available in VIPERS, to discard active galactic nuclei (AGNs), low ionization nuclear emission regions (LINERs), and Seyfert sources.

The above-described selection yields a sample of 1 049 galaxies, with their photometric S:N described in Table 4.2, covering a redshift range of $0.5 < z < 0.8$. A total of 592 galaxies in our sample have FIR detections from the HELP catalog. All of the galaxies in our sample have spectroscopic redshifts. Table 4.2 shows the photometric bands used for our data and the associated S:N for our final sample.

4.4 Estimating physical properties from spectral energy distribution

To model the spectra of our galaxies, we first assumed a stellar population. We then attenuated this stellar population with dust, assuming different dust and stars distribution. Also, we included the line measurements from the [O II] $\lambda 3727$, [O III] $\lambda 4959, \lambda 5007$, and H$\beta$ lines in the SED fitting procedure in `CIGALE` as done in Villa-Vélez et al. (2021). In the following subsections, we describe the different aspects of our SED fitting strategy and the motivation of our choice of certain templates and parameters.

TABLE 4.2: Summary of photometric data in each band with its centered wavelength, the mean of S:N, and the number of detections in our sample.

Telescope/ Instrument	Band	λ (μm)	Median S:N	Nº of detections
GALEX	FUV	0.15	5.45	1049
	NUV	0.23	9.78	1049
CFHT/	u	0.38	31	1049
MegaCam	g	0.49	61.69	1049
	r	0.63	50.62	1049
	i	0.76	78.69	1049
	z	0.89	40.90	1049
CFHT/WIRCam	Ks	2.14	25.25	1049
Spitzer/	ch1	3.56	27.66	710
IRAC	ch2	4.50	19.56	471
	ch3	5.74	10.43	112
	ch4	7.93	13.25	112
Spitzer/MIPS	MIPS1	24	15.90	116
	MIPS2	70	10.23	18
	MIPS3	160	6.19	3
Herschel/	100 μm	102.62	1.30	592
PACS	160 μm	167.14	1.38	592
Herschel/	250 μm	251.50	2.63	592
SPIRE	350 μm	352.83	1.51	592
	500 μm	511.60	1.05	592

4.4.1 Stellar population and its formation history

To model the stellar emission and the spectral evolution of galaxies, we considered stars with different ages and a certain metallicity. In this work, we use the stellar population library of Bruzual et al., 2003, a solar metallicity and an IMF of Chabrier, 2003, which takes into account a single star IMF as well as a binary star system. In terms of modeling, star formation histories (SFH) are very sensitive to many complex factors including galaxy environments, merging, gas accretion and its depletion (e.g. Elbaz et al., 2011; Ciesla et al., 2018; Schreiber et al., 2018b; Pearson et al., 2019). The SFHs have a significant effect on fitting the UV part of the SED, consequently affecting the derived physical parameters such as the stellar masses and the SFRs. Initially, we tested different SFH models to fit the observed short-wavelength photometry of our sources. These include a simple exponentially decreasing star formation characterized by an e-folding time τ, and a similar delayed model with a recent exponential burst or quench episode (Ciesla et al., 2017). In our models, we gave the e-folding time of the main stellar population (τ_{main}) a wide range of variation. Our initial results did not favor a recent burst in our sample, therefore we proceeded to use the simpler delayed SFH. In such a star formation scenario, a galaxy has built the majority of its stellar population in its earlier evolutionary phase, then the star formation activity slowly decreases over time. The SFR evolution over time is hereby modeled with:

$$\text{SFR}(t) \; \propto \; \frac{t}{\tau^2} \, e^{-t/\tau} \tag{4.2}$$

TABLE 4.3: Input parameters of the important physical models used to fit the SEDs of our sample with `CIGALE`.

Parameter	Values
Star formation history	
delayed	
Stellar age [Gyr]	equally-spaced 32 values in [0.5, 8]
e-folding time (τ) [Gyr]	equally-spaced 22 values in [0.5, 6]
Dust attenuation laws(a)	
(Calzetti et al., 2000)	
Colour excess of young stars E(B-V) mag	10 values in [0.1, 1]
Color excess of old stars (f_{att})	0.1, 0.3, 0.5, 0.8, 1.0
(Charlot et al., 2000)	
V-band attenuation in the ISM (A_V^{ISM}) mag	30 values in [0.3 - 3]
$Av_V^{ISM} / (A_V^{BC} + A_V^{ISM})$	0.1, 0.3, 0.5, 0.8, 1
Power law slope of the ISM	-0.7
Power law slope of the BC	-0.7
Dust emission	
(Draine et al., 2014)	
Mass fraction of PAH	1.12, 2.50, 3.90, 5.26, 6.63
Minimum radiation field (U_{min})	1, 5, 15, 25, 35
Power law slope (α)	2
Dust fraction in PDRs (γ)	5 values in [0.01, 0.2]

a) One attenuation law was used at a time in the SED fitting procedures. Both approaches were used in order to derive accurate physical properties.

where it translates into a delayed SFH slowed by the factor of τ^2, the e-folding time of the main stellar population, and extended over the large part of the age of the galaxy. This SFH provided better fits compared to the one with the recent burst. We vary τ as shown in Table 4.3, to give a comprehensive flexibility of the delayed formation of the main stellar population.

4.4.2 Dust attenuation

Modeling dust attenuation is an indispensable priority in any panchromatic SED fitting in order to reproduce the short wavelength photometry and therefore to extract accurate physical properties.

In this work, we used two contrasting approaches of attenuation laws for our SED fitting: the approach of Calzetti et al. (2000) and that of Charlot et al. (2000). While these two attenuation approaches are relatively simple, they differ in how to attenuate a given stellar population. Recently, Buat et al. (2019) and Hamed et al. (2021) showed that for statistical samples, it is necessary to use these two attenuation laws in order to recover the physical properties of galaxies, and chose the best-fit model among the two.

The attenuation curve of Calzetti et al. (2000) is a screen dust model. It was tuned to fit a sample of starbursts in the local Universe, which represent high redshift UV-bright galaxies.

This curve attenuates a stellar population with a simple power-law:

$$k(\lambda) = \frac{A(\lambda)}{E(B-V)}, \tag{4.3}$$

where k(λ) is the attenuation curve at a certain wavelength, A(λ) is the extinction curve, and $E(B-V)$ is the color excess between the B and V bands.

Despite its simplicity, this attenuation curve is widely used in the literature (e.g. Burgarella et al., 2005; Buat et al., 2012; Małek et al., 2014, 2017; Pearson et al., 2017; Buat et al., 2018; Elbaz et al., 2018; Ciesla et al., 2020). However, it does not always succeed in reproducing the UV extinction of galaxies at higher redshifts (Noll et al., 2009; Lo Faro et al., 2017).

Another approach is to consider the dust spatial distribution relative to the stellar population. This is the core of the attenuation curve of Charlot et al. (2000). In this approach, dust is considered to attenuate the dense and cooler stellar birth clouds (hereafter BCs) differently than ambient diffuse interstellar media (ISM). This configuration is expressed by two independent power-laws:

$$A(\lambda)_{\text{ISM}} \propto \left(\frac{\lambda}{\lambda_V}\right)^{\delta_{ISM}} \text{ and } A(\lambda)_{\text{BC}} \propto \left(\frac{\lambda}{\lambda_V}\right)^{\delta_{BC}}, \tag{4.4}$$

where δ_{ISM} and δ_{BC} are the slopes of attenuation in the ISM and the BCs respectively. Young stars that are in the BCs will therefore be attenuated twice: by the surrounding dust and additionally by the dust in the diffuse ISM. CF00 found that $\delta_{ISM} = \delta_{BC}$ = -0.7 satisfied dust attenuation in nearby galaxies, however, this curve is frequently used at higher redshifts (e.g. Buat et al., 2018; Małek et al., 2018; Donevski et al., 2020; Salim et al., 2020; Hamed et al., 2021). By attenuating at higher wavelengths (until the NIR) more efficiently than the recipe of Calzetti et al. (2000), this approach considers a more attenuated older stellar population. To model dust attenuation of the galaxies of our sample, we use the aforementioned laws, with the parameters presented in Table 4.3.

4.4.3   Dust emission

Modeling dust emission of our sample is not only crucial to derive the key observables that govern galaxy evolution such as the SFRs, but it is a cornerstone in correctly deriving IR luminosities which in turn might affect the estimation of the IRX. To reproduce the IR emission in our SED models, we use the templates of Draine et al. 2014. These templates take into consideration different sizes of grains of carbon and silicate, hence, allowing different temperatures of dust grains. They rely on observations and are widely used in the literature to fit FIR SEDs (e.g., Buat et al., 2019; Burgarella et al., 2020; Hamed et al., 2021).

Given that ~56% of our sample possess FIR data from the HELP catalog, we fit these IR-detected galaxies with Draine et al. (2014) dust templates, with and without IR data. That is, in one fitting, we used the full available panchromatic photometric coverage from FUV to 500 μm, using a stellar population library, SFH, dust attenuation, and dust emission templates. In another fitting procedure, we fit with the same templates only the selected range of photometry from FUV to IRAC4 band (8 μm). We then compare dust luminosities estimated using these two techniques, this comparison is provided in Figure 4.2.

The obtained IR luminosities with the aforementioned techniques correlated with a Pearson coefficient of $\rho = 0.96$. We then proceeded with fitting the photometry of galaxies that do not possess IR observations in the HELP catalog (457 galaxies out of 1049) with the same input parameters of Draine et al. (2014) templates, computing the IR luminosities based on the energy balance applied in the SED fitting using the short wavelength data. This allows for

$$y = 0.96x + 0.41$$
$$y = x$$
$$\rho = 0.96$$

sub-sample with *Herschel* data
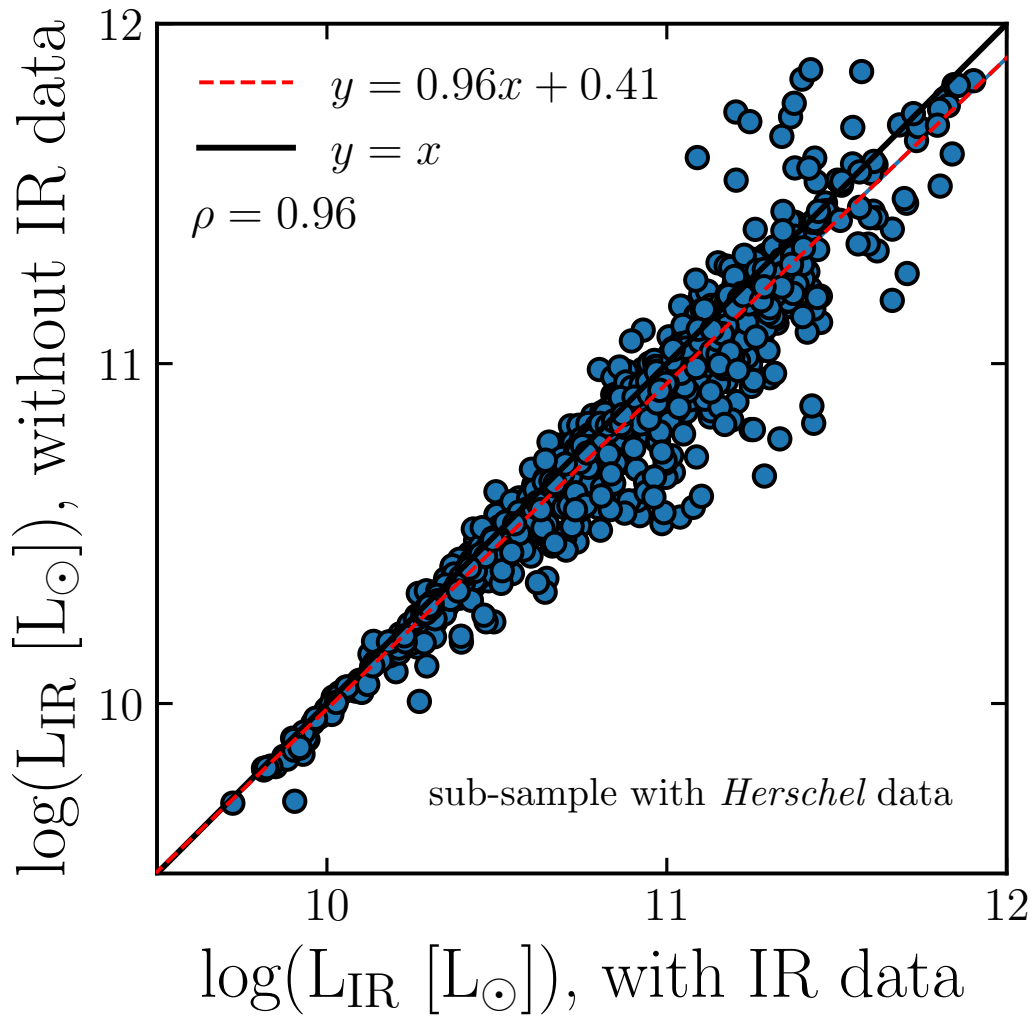
FIGURE 4.2: Dust luminosities estimated for the IR-detected sub-sample (592 galaxies out of 1049), with and without IR data. The solid black line shows the one-to-one relation. The dashed red line shows the best fit of this comparison, and ρ is the Pearson coefficient.

a reliable estimation of IR luminosities. We show the star-forming galaxy main sequence of our sample in Figure 4.3. Our fitting technique provided overall low uncertainty of physical properties, such as the stellar masses and the SFR.

4.4.4   SED quality, model assessment

To test the reliability of our SED models, with `CIGALE` we generated a mock galaxy sample and fitted SEDs with the same methods applied to our sample. We build the mock catalog by perturbing the fluxes of our best SEDs with errors sampled from a Gaussian distribution with a standard deviation equivalent to the uncertainty observed in the real fluxes. We show the mock analysis of the important estimated quantities in Figure 4.4, where we show the comparison between the real physical properties that we derived for our sample and its mock equivalent. The mean $\chi^2_{reduced}$ of our sample was 8.6. For each galaxy, we selected the attenuation law that best describes its observed photometry by comparing their χ^2, as in Buat
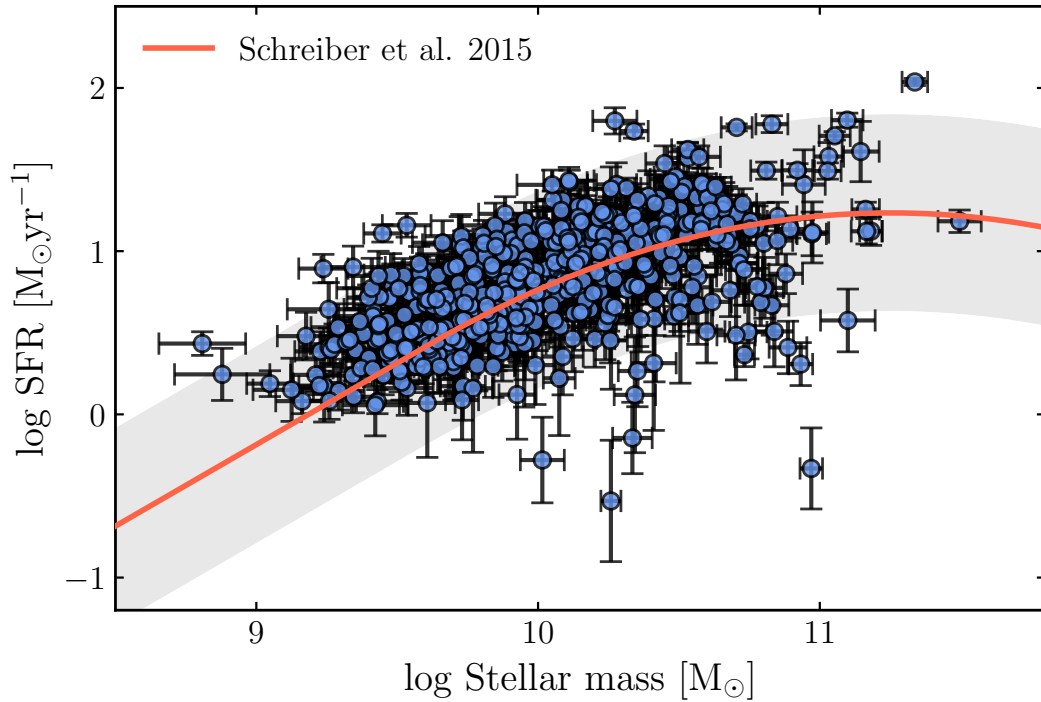
FIGURE 4.3: Star formation rates of our sample fitted with the best attenuation curve against stellar masses. The red line shows the main sequence of star-forming galaxies from Schreiber et al. (2015) at $z = 0.6$ (the median of our sample).

et al. (2019) and Hamed et al. (2021).

To estimate β for each galaxy in our sample, we fit a power-low function to the SED of each galaxy between the rest-frame ranges 0.126 μm and 0.260 μm. IRX was estimated directly from the SED fitting process, by dividing the IR luminosity by the FUV luminosity for each source, that is, IRX $=\log(L_{IR}/L_{FUV})$.

We also compared the SFRs derived using the spectroscopic lines, notably the Hβ and [O II] lines, with the ones obtained using SED of the photometry. We show this comparison in Appendix 4.10.1. This ensures a coherent interpretation of the SFR using the different methods. Overall, the mock analysis showed that our estimations of the physical observables, such as dust luminosities, SFRs, stellar masses, and IRX and β, are reliable.

4.5   Estimating the metallicity

Different calibrations are often used in the literature to measure the gas phase metallicity based on different line ratios (Pilyugin, 2001; Tremonti et al., 2004; Nagao et al., 2006; Curti et al., 2016). Making use of the robust oxygen emission lines along the Hβ line, we measured the gas phase metallicity using the ratio

$$R_{23} = \frac{[\text{O \textsc{ii}}]\,\lambda 3727 + [\text{O \textsc{iii}}]\,\lambda\lambda 4959, 5007}{\text{H}\beta}. \tag{4.5}$$

The R_{23} ratio was initially proposed in Pagel et al. (1979), and since then its tuning to oxygen abundance was improved by various photoionization models (Nagao et al., 2006). To derive the metallicity of our galaxies, we used the calibration proposed by Tremonti et
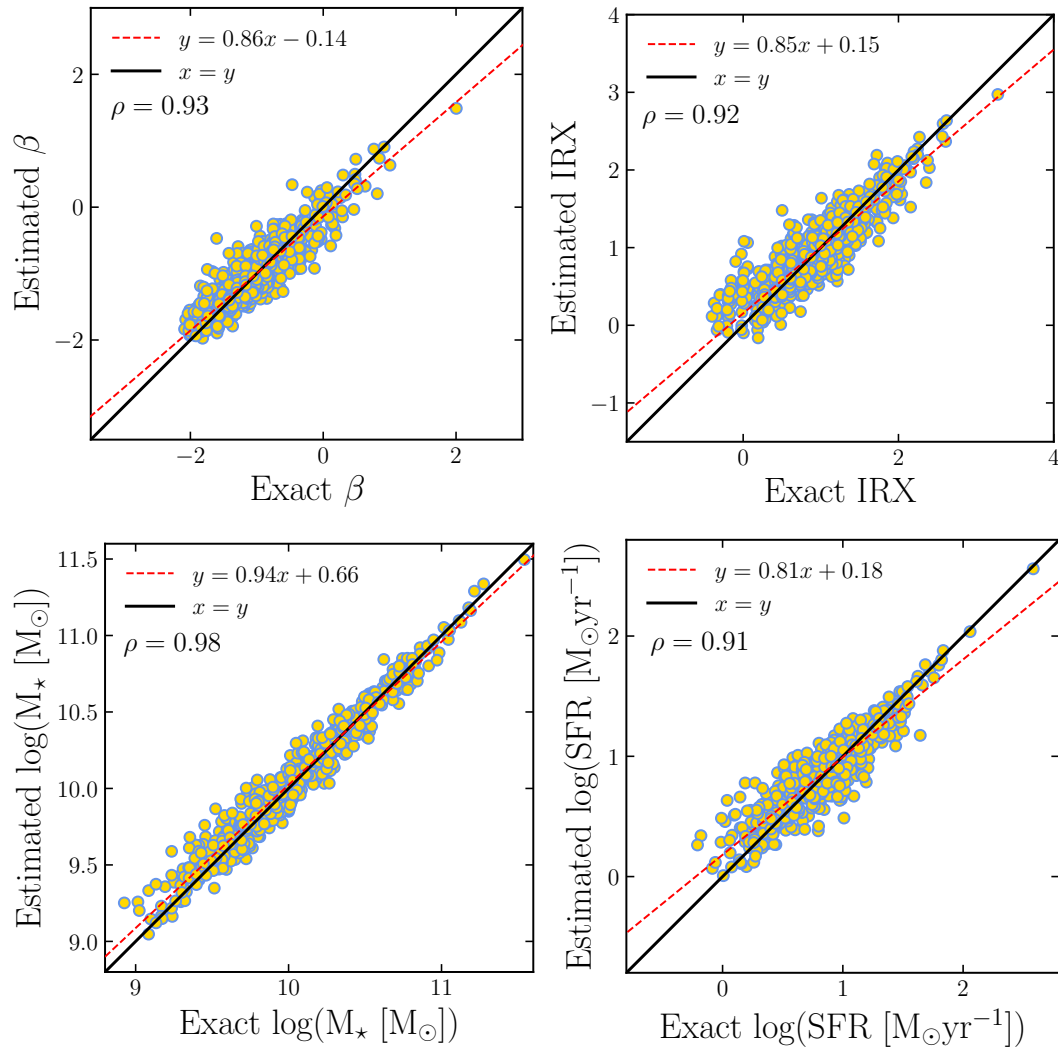
FIGURE 4.4: Comparison between some of the true parameters of the mock
SEDs and the results from the SED modeling with CIGALE. The "exact"
values are from mock models. ρ is the Pearson coefficient.

al. (2004), which is based on the R_{23} ratio of star-forming galaxies of double-valued R_{23}-abundance ratios. Following Nagao et al., 2006 we verified if our sample is in the upper branch ([O III] $\lambda 5007$/ [O II] $\lambda 3727 < 2$), and found that all data of our sample belong to the upper branch. Additionally, we removed all the sources that fall below the calibration limit of $12 + \log{(O/H)} \leq 8.4$, since this metallicity calibration is valid for values above that threshold. This discarded 47 galaxies, and left a total of 1002 galaxies for which valid metallicity estimation was calculated.

The calibration proposed by Tremonti et al. (2004) estimates the metallicity from theoretical model fitting of emission-lines. The model fits are calculated combining SSP synthesis models from Bruzual et al., 2003 and CLOUDY photoionization models (Ferland et al., 1998). The relation between metallicity and R_{23} is given by :

$$12 + \log{(O/H)} = 9.185 - 0.313x - 0.264x^2 - 0.321x^3, \tag{4.6}$$

where $x \equiv \log R_{23}$.

4.6   IRX-β relation of our sample

We show the scatter of IRX-β of our sample of star-forming galaxies in Figure 4.5. This scatter is observed to be higher than the relation fitted on the sample of local starburst galaxies by Meurer et al. (1999). We fit the scatter of our sample in the IRX-β diagram following the same method presented in Hao et al. (2011) and used similarly in Boquien et al. (2012).

To separate the influence of the SFH from the attenuation, we connect the attenuation to β:

$$A_{\text{FUV}} = (\beta - \beta_0) \times c_\beta, \tag{4.7}$$

where A_{FUV} is the attenuation in the FUV band, β_0 is the intrinsic UV slope (without dust), and c_β is the attenuation constant connecting both sides of the equation. The former can be seen as the degree to which the attenuation in the FUV band is influenced by the reddening caused by dust. On the other hand, IRX can be linked with dust attenuation via:

$$A_{\text{FUV}} = 2.5 \times \log(1 + c_{\text{IRX}} 10^{\text{IRX}}), \tag{4.8}$$

where c_{IRX} is the proportion of emission in the FUV band relative to the attenuation observed in other bands (Meurer et al., 1999; Boquien et al., 2012). Equations 4.7 and 4.8 can be integrated as in Hao et al. (2011):

$$\text{IRX} = \log\left(\frac{10^{0.4 \times (\beta - \beta_0)c_\beta} - 1}{c_{\text{IRX}}}\right). \tag{4.9}$$

which, for our sample, gives the following equation:

$$\text{IRX} = \log[(10^{0.91\beta + 2.02} - 1)/0.67]. \tag{4.10}$$

4.7   Results & Discussion: What drives the IRX-β relation?

4.7.1   Dependence on metallicity

A correlation between dust reddening and gas-phase metallicity is expected, as metals in the ISM will be depleted onto the same dust grains that attenuate the young stars and their emission lines. This means that the more metal content there is in the ISM, the more dust grains will be formed. Our findings suggest that metallicity is a significant contributing factor to the variability observed in the IRX-β relation, as shown in Figure 4.6. Metallicity is indicative of the characteristics of small dust particles that affect the attenuation curve (Zelko et al., 2020). Lower gas-phase metallicity results in stronger UV radiation in the ISM, leading to the breaking down of larger dust grains into smaller particles, assuming the conservation of the mass of dust. This results in an increase of the overall attenuation (Shivaei et al., 2020). Other works (e.g., Conroy et al., 2010; Wild et al., 2011) have also found that higher gas-phase metallicity is indicative of higher dust attenuation.

Dust-to-metal ratio (e.g., Wiseman et al., 2017; Li et al., 2019a) can also affect the scatter of galaxies in the IRX-β diagram. However, we did not find a strong correlation between the dust mass and the position of our sample with respect to the IRX-β relation. Although higher dust-mass galaxies occupied the upper part of the scatter, the correlation was not net as with the metallicity. Therefore dust mass was not found to be a key factor in the diagram. However, we found that dust-to-star geometry was strongly responsible for moving the scatter
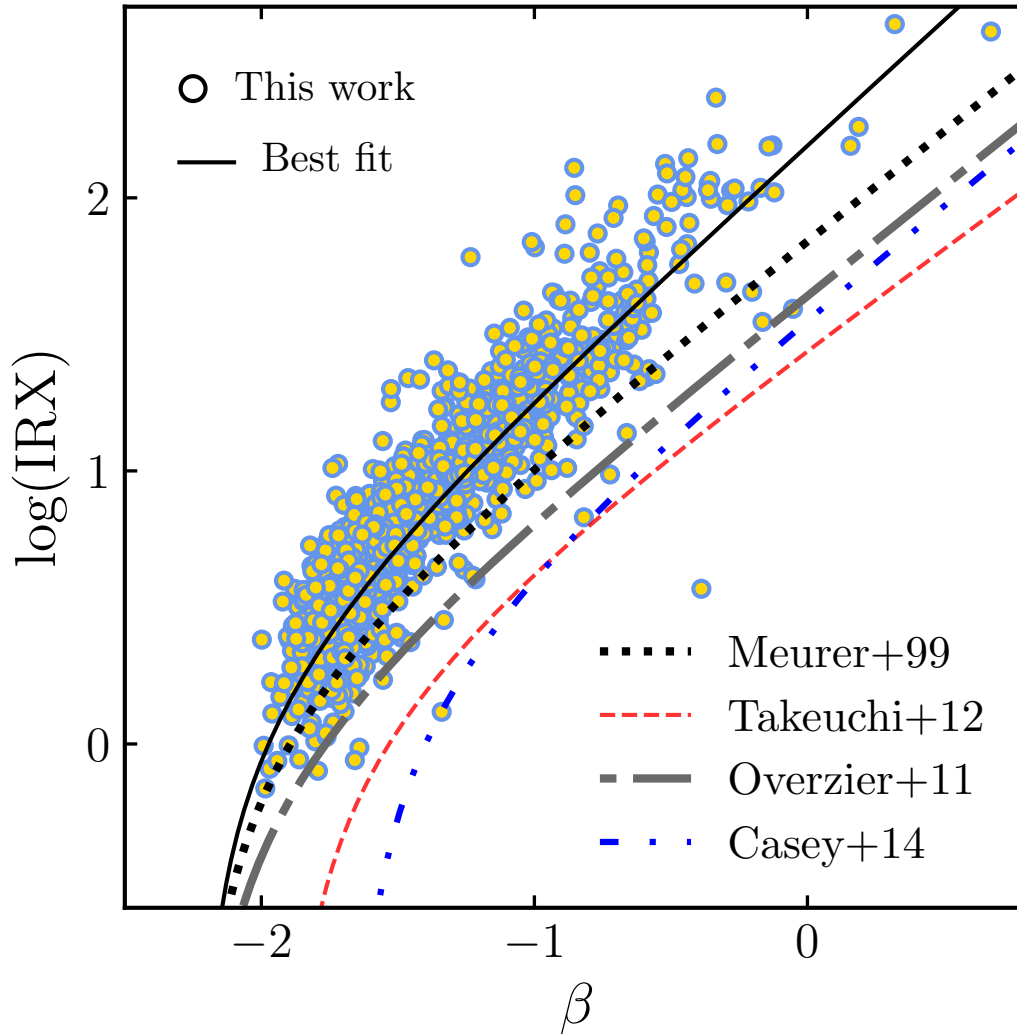
FIGURE 4.5: IRX-β scatter of our sample. The original Meurer et al. (1999) fit is shown in a dotted line. We also compare with fits from Overzier et al. (2011), Takeuchi et al. (2012), and Casey et al. (2014), denoted with grey dash-dotted, red dashed, and dash-double dotted lines, respectively. The solid black line shows Equation 4.10, describing our sample.

to the right (Popping et al., 2017). Galaxies that preferred the attenuation curve of CF00 were located towards redder β (higher β values).

4.7.2 Dependence on galaxy properties

We show the dependence of the IRX-β relation with the physical properties of our sample in Figure 4.7. Higher mass galaxies with older stellar populations occupy the higher IRX and β values of the diagram. The Pearson coefficients between the stellar mass and IRX and β are found to be $\rho = 0.96$ and $\rho = 0.98$ respectively for our sample, signifying a strong correlation. This almost linear scaling between the stellar mass and IRX and β was also found at different redshift ranges (e.g., Koprowski et al., 2018; Shivaei et al., 2020).

On the other hand, the specific SFR (sSFR = log SFR/$M_\star$) is found to decrease at higher β. This decrease is found to be stronger with β rather than IRX. The sSFR can be seen as a competition between the SFR and the stellar mass. At higher β values, the sharper increase of the stellar mass overcomes the slow increase in the SFR of our sample. Generally, high SFR in galaxies, with higher dust masses, results in a larger fraction of young massive stars in the stellar population, which increases the UV radiation. This UV radiation is absorbed by dust, which re-emits in the IR causing a higher IRX value.

The attenuation in the V band shows a strong trend in the diagram, with more optically attenuated galaxies located in the higher IRX and high β values. The specific dust mass ($M_{dust}/M_\star$) correlation with IRX-β is shown in Figure 4.7 (middle right panel). With higher specific dust mass, galaxies move away from the fitted relation towards lower β values.

4.7.3 Dependence on morphology

The morphological parameters of our sample were estimated using `GALFIT` in Krywult et al. (2017) where they applied Sérsic profiles fitting over the i-band of CFHT in their sample of VIPERS galaxies. A full description of the methodology used in deriving morphological parameters is detailed in Krywult et al. (2017). We notice a strong correlation between the Sérsic index (n) and the distribution of our sample in the IRX-β diagram. the Sérsic index
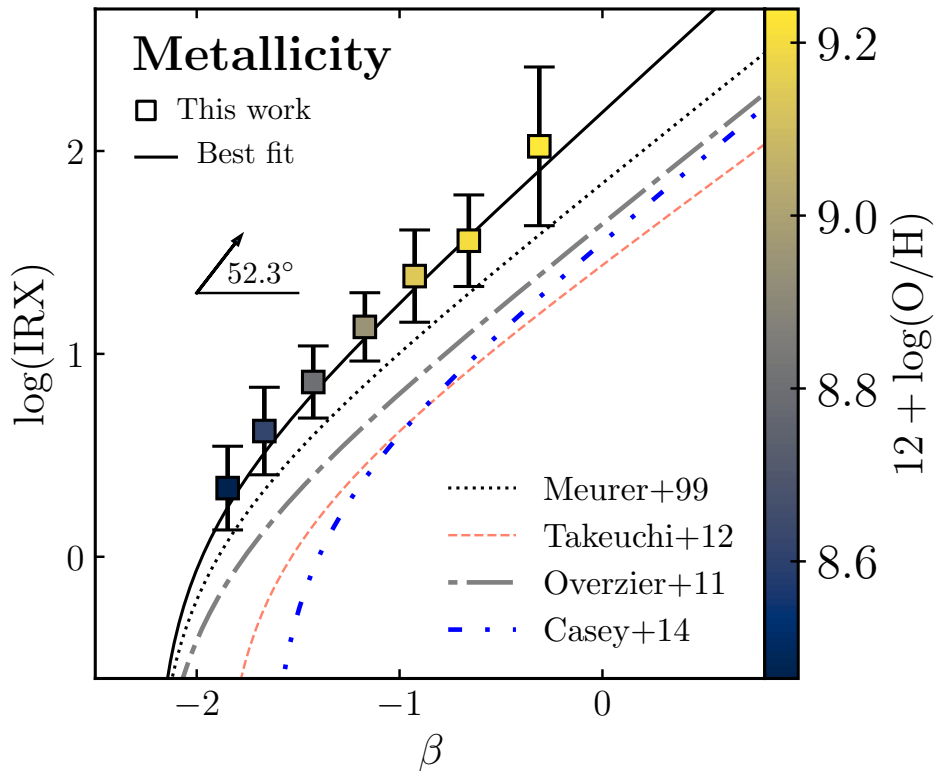
FIGURE 4.6: IRX-β scatter of our sample color-coded with metallicity. Points denote the VIPERS sample binned by β, every bin contains the same number of galaxies (160 galaxies) except the last bin which contains 89 galaxies. The best fits from the literature and the best fit of our sample are also shown. The colors and line-styles of these fits are the same as in Fig. 4.5. The arrow represents the trend of the metallicity, based on the scattered distribution. The angle is between the arrow and the x-axis.
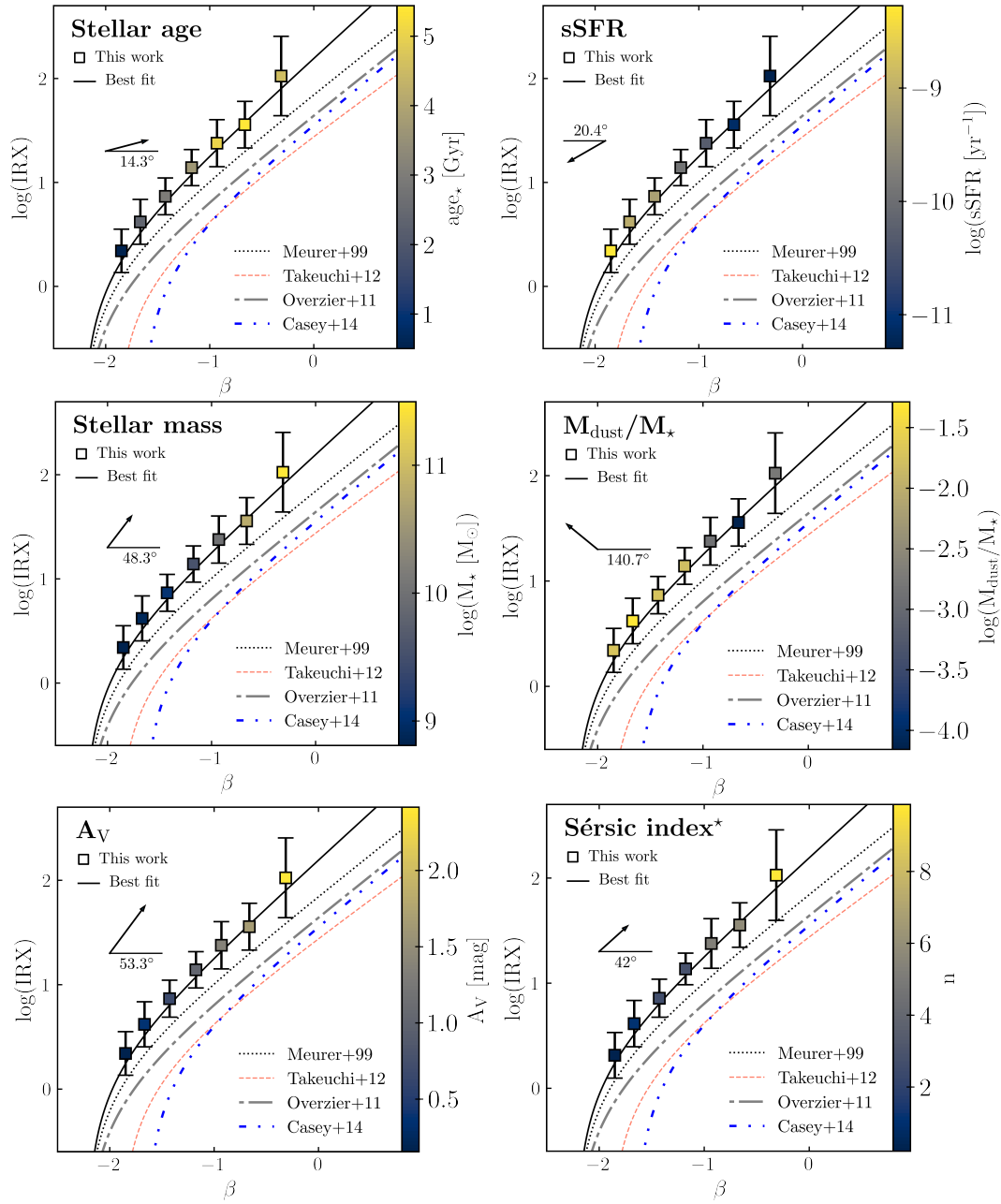
FIGURE 4.7: IRX-β binned scatter of our sample color-coded with different physical properties. Squares denote the VIPERS sample binned by β, every bin contains the same number of galaxies (160 galaxies) except the last bin which contains 89 galaxies. The original Meurer et al. (1999) fit is shown in a dotted line. We also compare with fits from Overzier et al. (2011), Takeuchi et al. (2012), and Casey et al. (2014), denoted with grey dash-dotted, red dashed, and dash-double dotted lines, respectively. The solid black line shows Equation 4.10, describing our sample. The arrows represent the trend of the physical properties, describing the direction of their scattered evolution. *In the lower right Figure with the Sérsic index, a total of 823 galaxies (instead of 1049) are binned, due to GALFIT flag selection, based on Krywult et al. (2017). The angles are between the arrows and the x or y-axis.

gives a Pearson coefficient of 0.95 with both IRX and β separately. We show the correlation with the Sérsic index in Figure 4.7 (lower right panel). The number of sources in this particular plot is less than the other plots of IRX-β, because we applied the most secure flag of Sérsic profiles fitting. This flag discards the galaxies for which `GALFIT` reported converge problems and keeps galaxies that had $0.2 < n < 10$. Our results show a strong correlation between the loci of our galaxies in the IRX-β diagram with galaxy compactness in the optical band.

Equivalently, we studied the dependence of the scatter we observe with galaxy inclination as in Wang et al. (2018). We use the same definition of disk galaxy inclinations as in the literature: galaxies for which the ratio of minor to major axis $(b/a) > 0.5$ are classified as face-on galaxies. On the other hand, galaxies whose $b/a \leq 0.5$ are considered edge-on galaxies. These definitions are valid for disk sources $(n < 2)$. In our analysis, we also adopt the same notion of compact galaxies, as those for which $n > 2$ (Wang et al., 2018). We show the IRX-β distribution of our sample based on galaxy morphology in Figure 4.8, where every bin contains the same number of galaxies ($\sim$ 110 galaxies).

We find that compact galaxies $(n > 2)$ occupy the higher IRX values relative to the less compact ones. This is shown using the whole sample in Figure 4.7 (lower right panel). However, for the disk galaxies, we find a subtle spread in the IRX-β scatter between the edge-on and face-on galaxies. Even though edge-on galaxies are found to have higher IRX with respect to the face-on galaxies, the difference was not found to be significant taking into account the large error bars. The slightly higher IRX values for edge-on galaxies, might be caused by the increase of the optical depth in these sources compared to the face-on galaxies
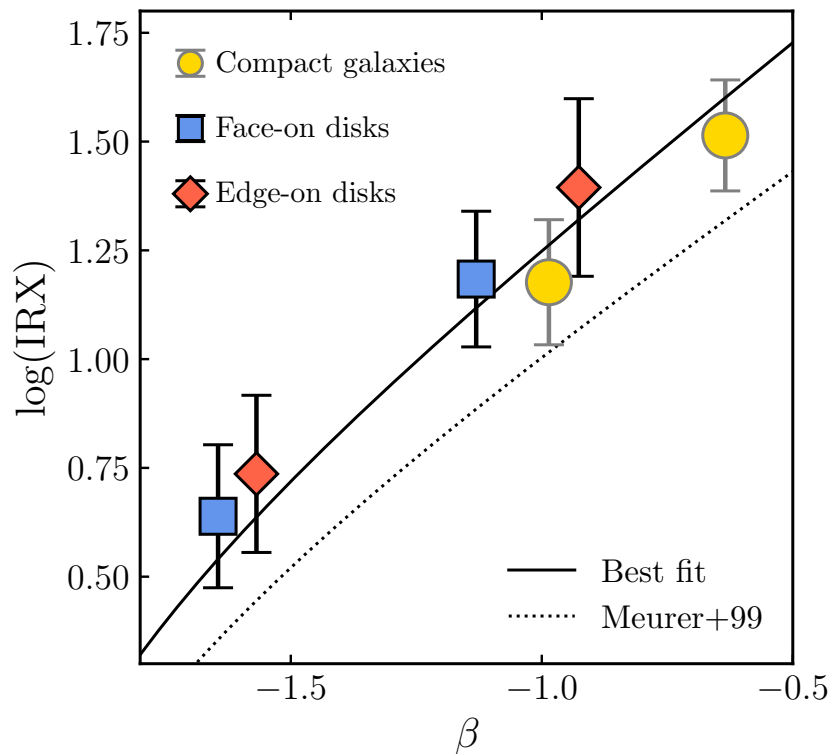
FIGURE 4.8: Our sample binned by β. Yellow circles represent compact galaxies $(n > 2)$. Blue squares show face-on disks $(b/a > 0.5$ and $n < 2)$. Red diamonds represent edge-on disk galaxies $(b/a < 0.5$ and $n < 2)$.
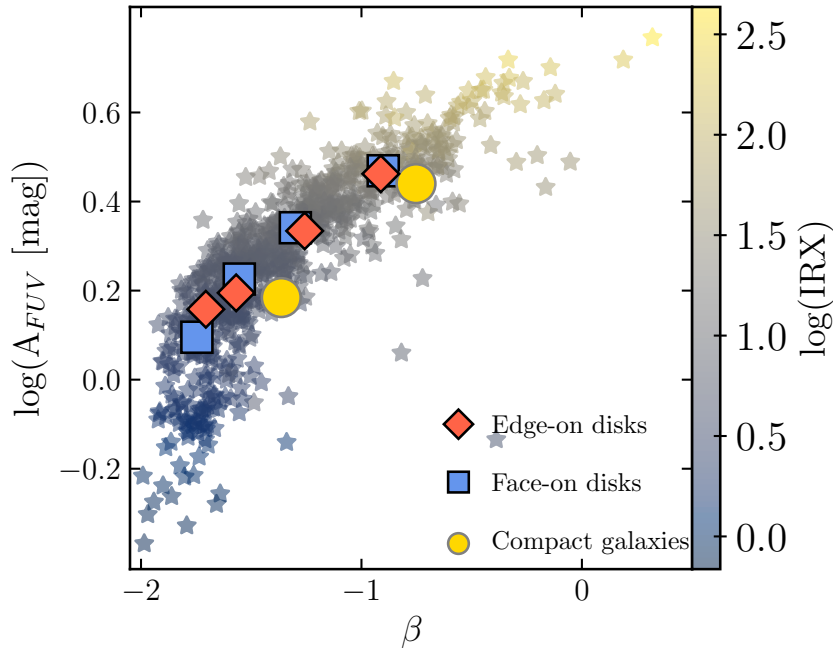
FIGURE 4.9: Variation of the attenuation in FUV with β, color-coded with
log(IRX). Edge-on disks have $b/a < 0.5$ and $n < 2$, while face-on disks
have $b/a > 0.5$ and $n < 2$. Compact galaxies are those for which $n > 2$.

(Wang et al., 2018).

In Figure 4.9 we show the variation of the attenuation in FUV with β for the different morphological classifications. For a fixed β value, we find no difference in attenuation between edge-on and face-on galaxies. This suggests that the inclination of galaxies does not affect the IRX-β scatter. A similar conclusion was also found in Wang et al. (2018).

4.8 Dust attenuation and galaxy environment

The density field of VIPERS data was computed by Cucciati et al. (2017), where they estimated the local environment around the galaxies. In their work, they computed the galaxy density contrast between the local density at a comoving distance around each source, and the mean density at a given redshift. The mean density was achieved using mock catalogs. The local density of each galaxy was measured based on its fifth nearest neighbor.
The local density contrast is defined as (e.g., Siudek et al., 2022):

$$\delta(RA, DEC, z) = \frac{\rho(RA, DEC, z) - \overline{\rho(z)}}{\overline{\rho(z)}}, \tag{4.11}$$

where $\rho(RA, DEC, z)$ is the local density of a given galaxy, and $\overline{\rho(z)}$ is the mean density at a redshift z.

We separate galaxies that reside in overdense and under-dense regions, defined as the 5th and 95th percentiles of the $\log(1+\delta)$ distribution, respectively (shown in Fig. 4.10, left panel). We do this in order to see the subtle difference in the IRX-β diagram (Figure 4.10 right panel).
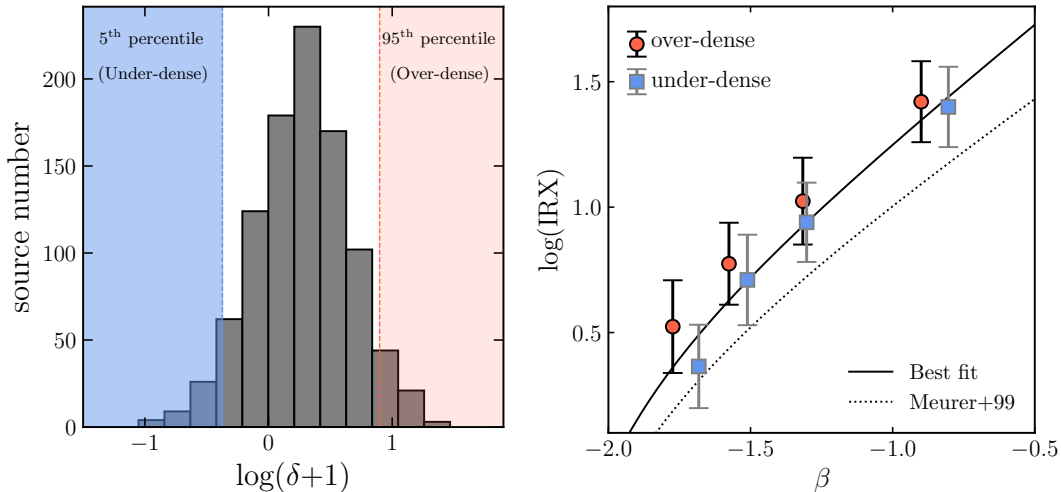
FIGURE 4.10: *Left panel:* Distribution of galaxy overdensity log(δ+1). In the blue region we show the selection of the 5th percentile of the overdensity (the galaxies residing in less-dense environments), and in the red region the selection of the 95th percentile of the distribution (galaxies residing in over-dense regions). *Right panel:* The 5th percentile and the 95th percentile of the selection from the left panel of this figure, in the IRX-β scatter.

We find no significant correlation with the IRX-β relation. Even though the galaxies that reside in less dense environments are slightly shifted towards the higher β values, for a given β, IRX is similar in the two galaxy groups within the error bars.

We analyzed the attenuation in FUV bands of the galaxies from our sample with their environment overdensities. We show this in Figure 4.11. We find no relation between the environmental overdensities and dust attenuation. Galaxies' environments strongly affect their physical properties (e.g., Peng et al., 2010), however, it is not understood how it might affect dust attenuation in galaxies. Shivaei et al. (2020) concluded similarly that environment does not seem to correlate with dust attenuation and consequently with the IRX-β relation. We extend this conclusion from the high redshift in their work down to intermediate redshift, showing that the variation of the A_{FUV} with galaxy overdensities is absent.

To quantify the degree of correlation in the IRX-β diagram, we show in Figure 4.7 the angles of the distribution of each physical property. We find that the most correlated quantities with the IRX-β plane, are the metallicities, galaxy compactness, and stellar mass.

4.9   Conclusions

In this work, we dissected the IRX-β dust attenuation relation for a large sample of 1049 galaxies at intermediate redshift (0.5 < z < 0.8). Having robust emission lines measurements, specifically the Hβ, [O II] and the double [O III] lines, we estimated the gas-phase metallicities of 1002 sources in our sample using Tremonti et al. (2004) calibration. Additionally, having full FUV to FIR detections of ~ half of our sample, we computed reliably the SEDs of the galaxies. We showed that for galaxies that do not possess FIR detections, we can reliably estimate the dust luminosity based on the SED energy balance principle.
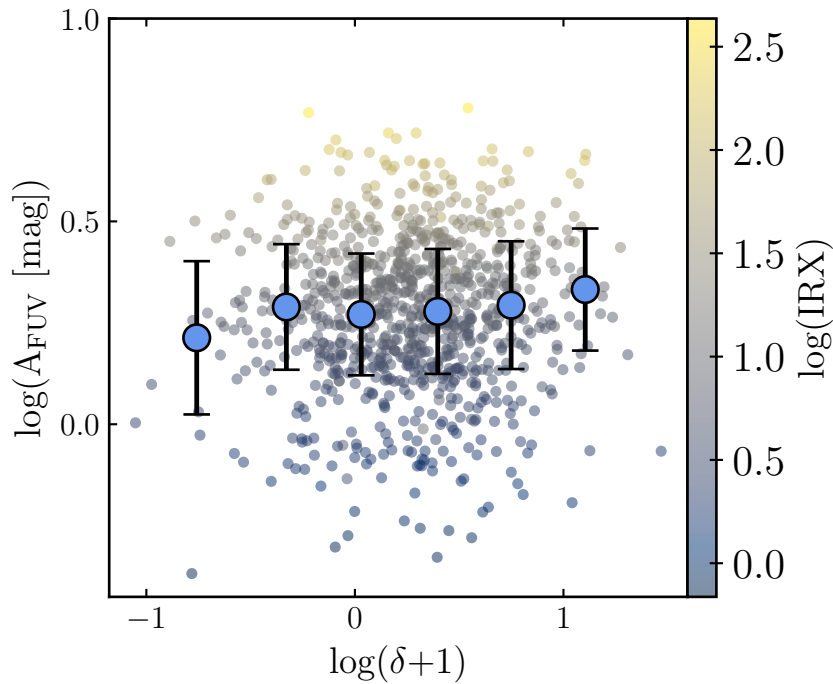
FIGURE 4.11: Attenuation in the FUV band, as a function of galaxy overdensities. The scatter represents the galaxies color-coded with IRX. We show the binned values for the whole sample (170 galaxies per bin).

Among the tested physical properties of our sample in the IRX-β relation, gas-phase metallicity correlated the most with the loci of the galaxies within this diagram, as was shown in Figure 4.6. A strong trend was also found with the stellar masses of our galaxies, and the age of their main stellar population. We conclude that metallicity is one of the drivers of the dust attenuation scatter, which is translated by the older stars and higher masses. The sSFR was found to decrease at lower β values, due to the competition between SFR and stellar mass where the SFR was not high enough to compensate for the clear increase of the stellar mass at higher IRX values. Similar results were achieved in the literature (e.g., Boquien et al., 2012; Koprowski et al., 2018; Shivaei et al., 2020). Our results suggest that at intermediate redshift, where earlier star-forming galaxies evolve, the dependence of the IRX-β scatter on these physical properties remains a key factor in shaping the dust attenuation curve.

We notice that the correlation with the specific dust mass is strong in shifting the galaxies farther away from the IRX-β relation towards lower β values. This is due to the strong increase in the relative mass of dust compared to the stellar mass, leading to higher IR luminosities.

Having the morphological parameters of our sample (Krywult et al., 2017), we analyzed the effect that certain morphological properties have on the location of galaxies in the IRX-β plane. We find a strong correlation with the Sérsic index n, that is, with higher IRX and β values, galaxy compactness seems to increase at the same rate. Morphologically, we find that more optically-compact objects (compact stellar population regions), witness a larger amount of attenuation than less compact galaxies.

We also tested the effect of galaxy inclination in the observed IRX-β scatter, by separating our sample into edge-on disks, face-on disks, and compact galaxies. There is a subtle

variation in the dust attenuation scatter between the edge-on and face-on galaxies. Although the edge-on galaxies show slightly higher IRX values than the face-on galaxies at a given β, this difference was not statistically significant considering the large error bars. The slight increase in IRX values for edge-on galaxies could be attributed to the higher optical depth in these galaxies as compared to the face-on galaxies, as suggested by Wang et al. (2018). Checking the variation of the attenuation in the FUV band with β, we found no difference in the amount of attenuation and β with IRX, as was shown in Figure 4.9.

We studied the effect of galaxy environments on dust attenuation in Section 4.8. To do so, we took the 5th percentile and the 95th percentile of the distribution of our sample's overdensities (computed in Cucciati et al. 2017). By this, we checked the loci of galaxies that most reside in less-dense environments and overdense ones. We found subtle differences in this relation, galaxies in over-dense environments were above the fitted IRX-β relation (Equation 4.10), and galaxies in under-dense regions were below this fit. However, given the large error bars, this difference was not robust. Similarly, we tested the attenuation in the FUV bands of our galaxies depending on the overdensity of their environments in Figure 4.11. We conclude that the environment does not affect dust attenuation of our sample of star-forming galaxies at intermediate redshift, despite the known effect the environment has on main galaxy properties such as the SFRs (Peng et al., 2010). Similar results were found by Shivaei et al. (2020) around the cosmic noon.

4.10 Appendices

4.10.1 Comparison of SED-computed SFRs with tracers

We show in Figure 4.12 the comparisons between the SFRs computed using `CIGALE` and those computed using the emission lines Hβ and [O II]. The correlation between all these estimators demonstrate the effectiveness of the derived SFRs using panchromatic SED fitting.
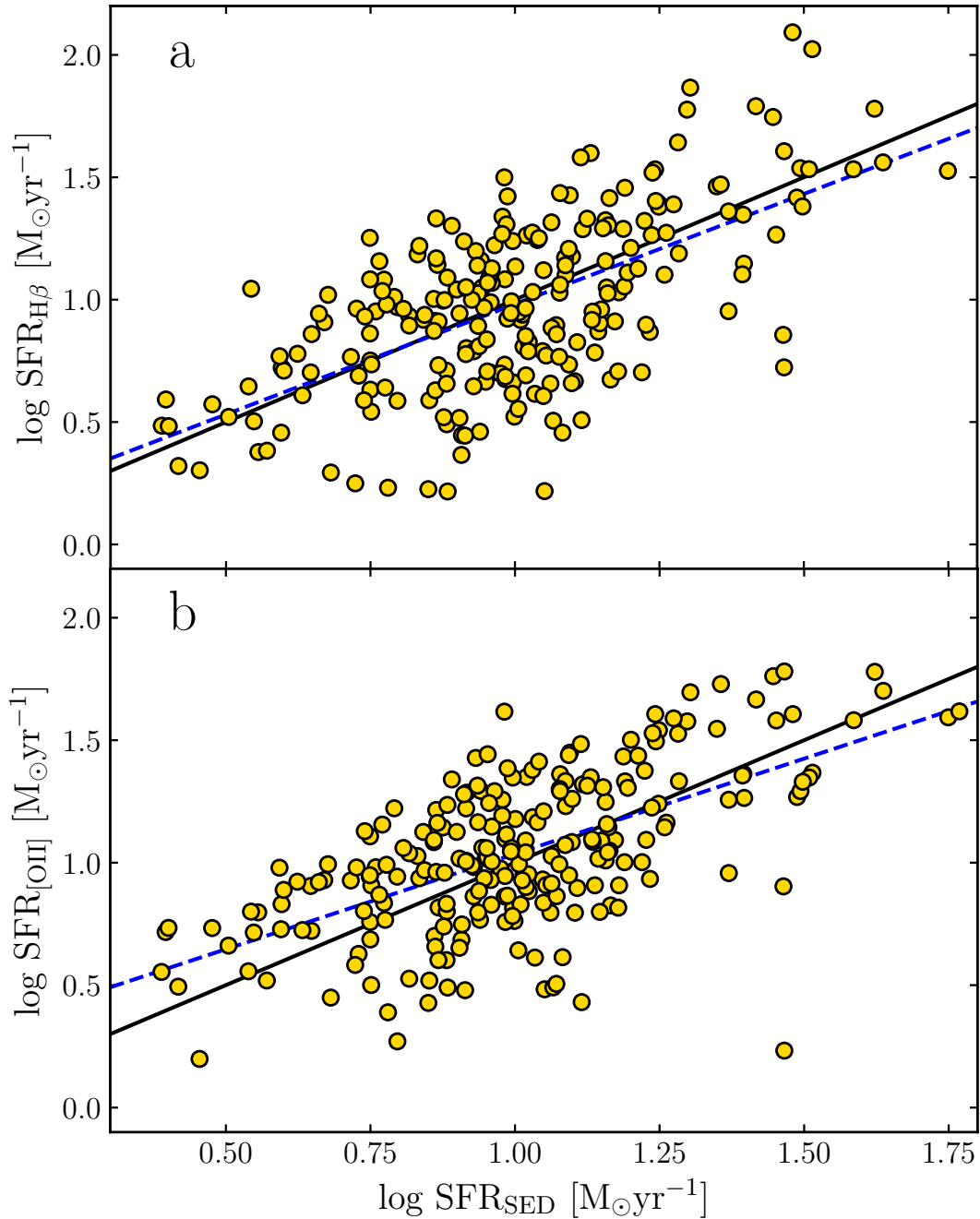
FIGURE 4.12: Star formation rates derived with (a): Hβ and (b): [O II], compared with the SFRs derived with the full SED.
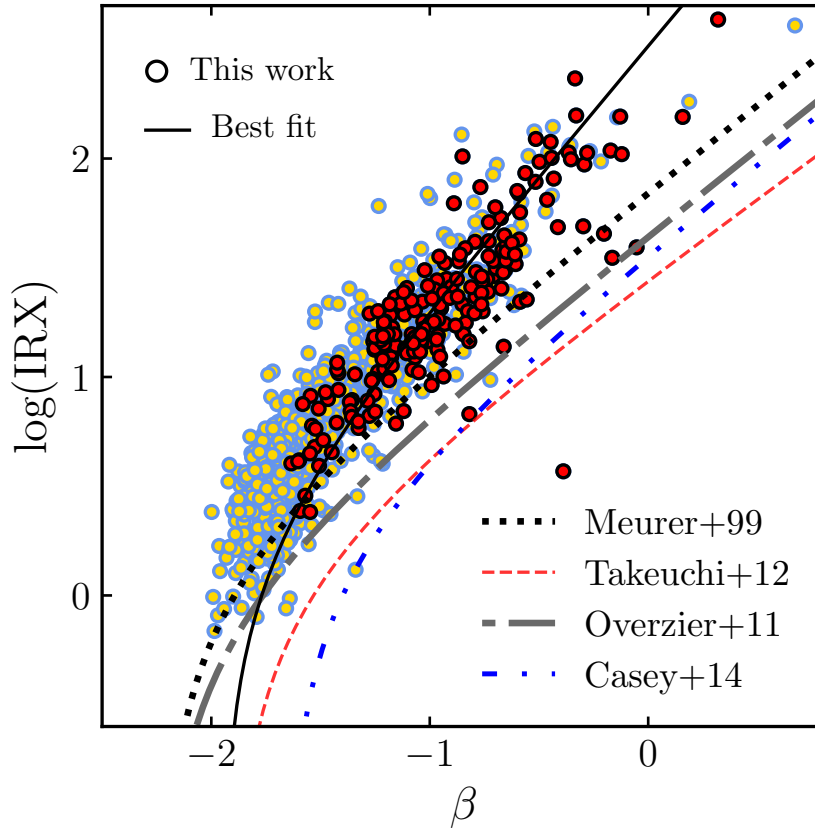
FIGURE 4.13: IRX-β scatter of our sample. The original Meurer et al. (1999) fit is shown in dotted line. We also compare with fits from Overzier et al. (2011), Takeuchi et al. (2012), and Casey et al. (2014), denoted with grey dash-dotted, red dashed, and dash-double dotted lines, respectively. The solid black line shows Equation 4.12, describing our mass-complete sample.

4.10.2   Mass-complete sub-sample

We also derive the IRX-β relation for our mass-complete sub-sample. To achieve the mass-complete sub-sample, we select galaxies for which $\log(M_\star) \geq 10.18$ M$_\odot$ for $z \leq 0.6$, and $\log(M_\star) \geq 10.47$ M$_\odot$ for $z \leq 0.8$, following Davidzon et al. (2016) selections for VIPERS.

These selections result in only 258 galaxies from our initial sample. The IRX-β fit for this sub-sample is then given by:

$$\mathrm{IRX} = \log[(10^{2.98\beta+1.95} - 1)/0.64]. \tag{4.12}$$

We show the fit for the mass-complete sub-sample in Figure 4.13. The mass-complete sample is statistically less important than our full sample, and it lacks data in the lower IRX and β values, therefore it must be considered with caution.

Summary of the fourth chapter

- In this work, the IRX-β dust attenuation relation was achieved at intermediate redshift (0.5 < 0.8) with a large sample of more than 1 000 star-forming galaxies. Gas-phase metallicity was estimated for this sample, having the emission lines of Hβ, [O $\textsc{ii}$], and [O $\textsc{iii}$]. Spectral energy distributions of these galaxies were also achieved.

- Almost half of the sample had detections in the far infrared range of *Herschel*. Dust luminosity for the whole sample was estimated, but for the galaxies without far infrared detections, dust luminosity was estimated based on the energy balance principle of the spectral energy distribution.

- Gas-phase metallicity was found to be the strongest correlate with the loci of the galaxies in the IRX-β diagram.

- Strong trends were also found with the galaxies' stellar masses and the age of their main stellar population. Metallicity is one of the drivers of the dust attenuation scatter, which is translated by the older stars and higher masses.

- The specific star formation rate was found to decrease at lower β values due to the competition between star formation rates and stellar mass. Specific dust mass was found to be strongly correlated with shifting galaxies away from the IRX-β relation towards lower β values. Morphological parameters of the sample were analyzed, and a strong correlation was found with the Sérsic index. More optically-compact objects witness a larger amount of attenuation than less compact galaxies. The effect of galaxy inclination on the observed IRX-β scatter was tested, but no statistically significant difference was found.

- No difference in the amount of attenuation and β with IRX was found in the far ultraviolet band. The effect of galaxy environments on dust attenuation was studied, but no significant difference was found. Galaxies in overdense environments were above the fitted IRX-β relation, while galaxies in under-dense regions were below it, but this difference was not robust. The environment does not affect dust attenuation of the sample of star-forming galaxies at intermediate redshift.

- The study supports the idea that at intermediate redshift, the dependence of dust attenuation on physical properties, especially metallicity and morphology, remains a key factor in shaping the dust attenuation curve.

5

Summary and perspectives

In this thesis, and through three interconnected complementary works, I investigated dust attenuation in different galaxies at different redshifts, with varied characteristics. Several important results were achieved. This chapter is a summary of these works, accompanied by some perspectives.

Galaxies are the key to understanding the evolution of the Universe. To understand the evolution of galaxies, it is essential to study the dust component of the ISM, since dust is a main driver of the star formation in the Universe. Observations of galaxies have revealed that their properties, such as stellar masses and SFRs, are affected by interstellar dust. Interstellar dust absorbs and scatters light, causing reddening and dimming effects that can obscure and alter our observations of galaxies. Therefore, it is crucial to correct dust attenuation to obtain accurate measurements of galaxy properties. To account for dust absorption of the stellar light, it is necessary to use a dust attenuation law in order to reproduce the observed photometry of galaxies. Many works that use attenuation laws do not apply different attenuation recipes, despite the fact that it is known already that dust attenuation curves are not universal. We still lack complete knowledge of what is the main driver of the attenuation curve in galaxies at different redshifts.

In my first work (i.e., Hamed et al., 2021), I investigated a system of galaxies at the cosmic noon ($z \sim 2$). During this epoch, the star formation rate density peaked in the Universe. One of the galaxies I investigated is a supermassive extremely attenuated by dust, star-forming galaxy. The ALMA detection of its CO molecule emission allowed us to estimate its molecular hydrogen reservoir. Having the full panchromatic coverage of this object, the SFR was reliably estimated. The gas reservoir of this galaxy was found to be not enough to sustain the current rate of the star formation activity, giving it a depletion time of 0.22 ± 0.07 Gyr, which is similarly found in extreme starburst galaxies. However, this galaxy is residing in the main sequence of star-forming galaxies. This starburst-like star formation activity on the main sequence was found for massive compact galaxies in post-starburst episodes, confirming that the massive ALMA- detected IR galaxy is caught in the middle of quenching following an earlier starburst activity. The less massive companion of this galaxy was found to be dust-poor and exhibiting a starburst phase in its star formation. This work highlighted the importance of the assumed dust attenuation law when building the SED of galaxies, especially since different attenuation laws might result in significantly different derived stellar masses. Additionally, I found that the morphological aspects of DSFGs are equivalently crucial and interesting when dissecting galaxies in different wavelengths and deriving physical parameters.

In the second work (i.e., Hamed et al., 2023), I generalized what I found in the first work and in previous recent literature, with regards to dust attenuation. These older works have dealt with low samples of galaxies. In this work, I sampled high signal-to-noise panchromatic coverage of 122 galaxies detected from the UV band to the FIR bands of *Herschel*, including ALMA detections of all my samples. This has allowed us to investigate the effect of the morphology of dusty star-forming galaxies on dust attenuation. Effective radii in HSC's *Y* band and ALMA-detected dust continuum maps were calculated for the sample in this study. Additionally, having full panchromatic coverage, SEDs were computed.

This work presents the largest statistical work done on a large sample of galaxies examining dust attenuation and morphological extensions. The most widely used attenuation laws in the literature were used in this work. These laws include the simple Calzetti et al. (2000) law and that of Charlot et al. (2000). The results showed that the relative spatial extent of the emission from the stellar population and star-forming regions compared to that of the dust was crucial in determining the appropriate dust attenuation curve. Galaxies with relatively compact star-to-dust radii ratios were best fit by the starburst curve of Calzetti et al. (2000), while those with compact dust emission and extended stellar radii required shallow curves and double exponential attenuation laws. The study also found that the star-to-dust compactness of the unobscured star-forming regions and stellar population regions to dust emission of these galaxies peaked around the cosmic noon ($z \sim 2$). Additionally, the energy balance between the stellar emission and their infrared counterparts was investigated, revealing that most sources produced the same dust emission when relying on an energetic balance from short wavelengths, but some galaxies expressed dimmer star formation when the Calzetti et al. (2000) attenuation law was used. Overall, these findings are promising for future surveys of deep field observations, such as the JWST and LSST, where highly-resolved high redshift observations in the short and mid-infrared wavelengths could generalize these findings over a larger statistical sample of galaxies.

In my last work of this thesis, I focused on investigating the IRX-β dust attenuation relation at intermediate redshift. On the one hand, I needed a large sample to generalize the previous findings of the morphological role in dust attenuation in galaxies. On the other hand, intermediate redshift is often left unvisited by large studies, where most of the works focus either on the local Universe or very high redshifts. Therefore, I constructed a large sample of more than $1\,000$ galaxies at a redshift range of $0.5 < z < 0.8$, with detections of their Hβ, [O II], and [O III] lines. Additionally, this sample's morphological parameters were estimated previously by Krywult et al. (2017), along with the environments they reside in (Cucciati et al., 2017). These galaxies did not have detections by ALMA and therefore their dust continua were not observed. However, it was found that gas-phase metallicity is one of the strongest properties to correlate with the loci of the galaxies in the IRX-β diagram. Strong trends were also found with the stellar masses and the age of their main stellar population. The specific star formation rate was found to decrease at lower β values due to the competition between star formation rates and stellar mass. Specific dust mass is strongly correlated with shifting galaxies away from the IRX-β relation towards lower β values. The morphological parameters of the sample were analyzed, and a strong correlation was found with the Sérsic index, where more optically-compact objects are witnessing a larger amount of attenuation than less compact galaxies. Galaxy inclination was found not to affect the scatter of this dust attenuation relation significantly. Additionally, one of the most important results was the insignificance of the environments in which galaxies reside in playing a role in the attenuation that these galaxies exhibit. At intermediate redshift, the dependence of dust attenuation on physical properties, especially metallicity and galaxy morphology, remains a

key factor in shaping the dust attenuation curve.

These combined works highlight the strong importance of dust attenuation at intermediate and high redshifts. One important finding was the crucial aspect of galaxy morphology, especially the relative spatial extent of the star-forming regions and that of dust emission. This relative compactness should be considered prior to SED fitting. This is a generalization of the previous work of Buat et al. (2019) in which they studied the effect of the spatial distribution of stars and dust on attenuation. However, their sample was statistically insignificant and not complete, and their galaxies were around the cosmic noon. In my study, I found a similar correlation in a wide redshift range. Moreover, having a large statistical sample of galaxies at intermediate redshift, with robust estimations of physical properties, I find the IRX-β relation for star-forming galaxies.

This thesis, with the works presented in it, is a starting point for future works that will complement and complete these findings. The aspect of galaxies' compactness and its link to estimated other properties such as the SFR and dust properties will greatly benefit from the plethora of high redshift observations of new powerful instruments. This answers the question of what attenuation law to use at high redshift. Moreover, as a complementary follow-up for my third work (presented in chapter 4), I will investigate the star formation history of the sample that I achieved, and I will reverse-engineer the episodes of star formation using the observed metallicities. To achieve this, I will include models of stellar evolution (e.g., Côté et al., 2017; Nanni et al., 2020).

Bibliography

Russell, Henry Norris (1922). Dark Nebulae. *Proceedings of the National Academy of Sciences of the United States of America* 8.5, pp. 115–118. ISSN: 00278424. URL: http://www.jstor.org/stable/84390 (visited on 03/24/2023).

Eddington, A. S. (1926). *The Internal Constitution of the Stars*.

Hubble, Edwin (Jan. 1934). The Distribution of Extra-Galactic Nebulae. 79, p. 8. DOI: 10.1086/143517.

Salpeter, Edwin E. (Jan. 1955). The Luminosity Function and Stellar Evolution. 121, p. 161. DOI: 10.1086/145971.

Schmidt, Maarten (1959). The Rate of Star Formation. 129, p. 243. DOI: 10.1086/146614.

Pagel, B. E. J. et al. (Oct. 1979). On the composition of H II regions in southern galaxies - I. NGC 300 and 1365. 189, pp. 95–113. DOI: 10.1093/mnras/189.1.95.

Baldwin, J. A. et al. (Feb. 1981). Classification parameters for the emission-line spectra of extragalactic objects. 93, pp. 5–19. DOI: 10.1086/130766.

Draine, B. T. et al. (Oct. 1984). Optical Properties of Interstellar Graphite and Silicate Grains. 285, p. 89. DOI: 10.1086/162480.

Desert, F. X. et al. (Oct. 1990). Interstellar Dust Models for Extinction and Emission. 237, p. 215.

Calzetti, Daniela et al. (July 1994). Dust Extinction of the Stellar Continua in Starburst Galaxies: The Ultraviolet and Optical Extinction Law. 429, p. 582. DOI: 10.1086/174346.

Meurer, G. R. et al. (Dec. 1995). Starbursts and Star Clusters in the Ultraviolet. 110, p. 2665. DOI: 10.1086/117721. arXiv: astro-ph/9509038 [astro-ph].

Smail, Ian et al. (Nov. 1997). A Deep Sub-millimeter Survey of Lensing Clusters: A New Window on Galaxy Formation and Evolution. 490.1, pp. L5–L8. DOI: 10.1086/311017. arXiv: astro-ph/9708135 [astro-ph].

Solomon, P. M. et al. (Mar. 1997). The Molecular Interstellar Medium in Ultraluminous Infrared Galaxies. 478.1, pp. 144–161. DOI: 10.1086/303765. arXiv: astro-ph/9610166 [astro-ph].

Downes, D. et al. (Nov. 1998). Rotating Nuclear Rings and Extreme Starbursts in Ultraluminous Galaxies. 507.2, pp. 615–654. DOI: 10.1086/306339. arXiv: astro-ph/9806377 [astro-ph].

Ferland, G. J. et al. (July 1998). CLOUDY 90: Numerical Simulation of Plasmas and Their Spectra. 110.749, pp. 761–778. DOI: 10.1086/316190.

Kennicutt Robert C., Jr. (1998). Star Formation in Galaxies Along the Hubble Sequence. 36, pp. 189–232. DOI: 10.1146/annurev.astro.36.1.189. arXiv: astro-ph/9807187 [astro-ph].

Schlegel, David J. et al. (June 1998). Maps of Dust Infrared Emission for Use in Estimation of Reddening and Cosmic Microwave Background Radiation Foregrounds. 500.2, pp. 525–553. DOI: 10.1086/305772. arXiv: astro-ph/9710327 [astro-ph].

Meurer, Gerhardt R. et al. (Aug. 1999). Dust Absorption and the Ultraviolet Luminosity Density at z ~3 as Calibrated by Local Starburst Galaxies. 521.1, pp. 64–80. DOI: 10.1086/307523. arXiv: astro-ph/9903054 [astro-ph].

Calzetti, Daniela et al. (Apr. 2000). The Dust Content and Opacity of Actively Star-forming Galaxies. 533.2, pp. 682–695. DOI: 10.1086/308692. arXiv: astro-ph/9911459 [astro-ph].

Charlot, Stéphane et al. (Aug. 2000). A Simple Model for the Absorption of Starlight by Dust in Galaxies. 539.2, pp. 718–731. DOI: 10.1086/309250. arXiv: astro-ph/0003128 [astro-ph].

Gordon, Karl D. et al. (Apr. 2000). The Flux Ratio Method for Determining the Dust Attenuation of Starburst Galaxies. 533.1, pp. 236–244. DOI: 10.1086/308668. arXiv: astro-ph/9912034 [astro-ph].

Pozzetti, L. et al. (Sept. 2000). Extremely red galaxies: age and dust degeneracy solved? *Monthly Notices of the Royal Astronomical Society* 317.1, pp. L17–L21. ISSN: 0035-8711. DOI: 10.1046/j.1365-8711.2000.03829.x. eprint: https://academic.oup.com/mnras/article-pdf/317/1/L17/18635221/317-1-L17.pdf. URL: https://doi.org/10.1046/j.1365-8711.2000.03829.x.

Bell, Eric F. et al. (Mar. 2001). Stellar Mass-to-Light Ratios and the Tully-Fisher Relation. 550.1, pp. 212–229. DOI: 10.1086/319728. arXiv: astro-ph/0011493 [astro-ph].

Calzetti, Daniela (Dec. 2001). The Dust Opacity of Star-forming Galaxies. 113.790, pp. 1449–1485. DOI: 10.1086/324269. arXiv: astro-ph/0109035 [astro-ph].

Dunne, Loretta et al. (Nov. 2001). The SCUBA Local Universe Galaxy Survey - II. 450-μm data: evidence for cold dust in bright IRAS galaxies. 327.3, pp. 697–714. DOI: 10.1046/j.1365-8711.2001.04789.x. arXiv: astro-ph/0106362 [astro-ph].

Papovich, Casey et al. (Oct. 2001). The Stellar Populations and Evolution of Lyman Break Galaxies. 559.2, pp. 620–653. DOI: 10.1086/322412. arXiv: astro-ph/0105087 [astro-ph].

Pilyugin, L. S. (Aug. 2001). Oxygen abundances in dwarf irregular galaxies and the metallicity-luminosity relationship. 374, pp. 412–420. DOI: 10.1051/0004-6361:20010732. arXiv: astro-ph/0105360 [astro-ph].

Shapley, Alice E. et al. (Nov. 2001). The Rest-Frame Optical Properties of z∼=3 Galaxies. 562.1, pp. 95–123. DOI: 10.1086/323432. arXiv: astro-ph/0107324 [astro-ph].

Weingartner, Joseph C. et al. (June 2001). Photoelectric Emission from Interstellar Dust: Grain Charging and Gas Heating. 134.2, pp. 263–281. DOI: 10.1086/320852. arXiv: astro-ph/9907251 [astro-ph].

Blain, Andrew W. et al. (Oct. 2002). Submillimeter galaxies. 369.2, pp. 111–176. DOI: 10.1016/S0370-1573(02)00134-5. arXiv: astro-ph/0202228 [astro-ph].

Carlstrom, John E. et al. (Jan. 2002). Cosmology with the Sunyaev-Zel'dovich Effect. 40, pp. 643–680. DOI: 10.1146/annurev.astro.40.060401.093803. arXiv: astro-ph/0208192 [astro-ph].

Dale, Daniel A. et al. (Sept. 2002). The Infrared Spectral Energy Distribution of Normal Star-forming Galaxies: Calibration at Far-Infrared and Submillimeter Wavelengths. 576.1, pp. 159–168. DOI: 10.1086/341632. arXiv: astro-ph/0205085 [astro-ph].

Kroupa, Pavel (Jan. 2002). The Initial Mass Function of Stars: Evidence for Uniformity in Variable Systems. *Science* 295.5552, pp. 82–91. DOI: 10.1126/science.1067524. arXiv: astro-ph/0201098 [astro-ph].

Peng, Chien Y. et al. (July 2002). Detailed Structural Decomposition of Galaxy Images. 124.1, pp. 266–293. DOI: 10.1086/340952. arXiv: astro-ph/0204182 [astro-ph].

Rosa-González, Daniel et al. (May 2002). An empirical calibration of star formation rate estimators. 332.2, pp. 283–295. DOI: 10.1046/j.1365-8711.2002.05285.x. arXiv: astro-ph/0112556 [astro-ph].

Bell, Eric F. et al. (Dec. 2003). The Optical and Near-Infrared Properties of Galaxies. I. Luminosity and Stellar Mass Functions. 149.2, pp. 289–312. DOI: 10.1086/378847. arXiv: astro-ph/0302543 [astro-ph].

Bruzual, G. et al. (Oct. 2003). Stellar population synthesis at the resolution of 2003. 344.4, pp. 1000–1028. DOI: 10.1046/j.1365-8711.2003.06897.x. arXiv: astro-ph/0309134 [astro-ph].

Chabrier, Gilles (July 2003). Galactic Stellar and Substellar Initial Mass Function. 115.809, pp. 763–795. DOI: 10.1086/376392. arXiv: astro-ph/0304382 [astro-ph].

Chapman, S. C. et al. (Apr. 2003). A median redshift of 2.4 for galaxies bright at submillimetre wavelengths. 422.6933, pp. 695–698. DOI: 10.1038/nature01540. arXiv: astro-ph/0304235 [astro-ph].

Downes, D. et al. (Jan. 2003). Molecular Gas and Dust at z=2.6 in SMM J14011+0252: A Strongly Lensed Ultraluminous Galaxy, Not a Huge Massive Disk. 582.1, pp. 37–48. DOI: 10.1086/344594. arXiv: astro-ph/0210040 [astro-ph].

Draine, B. T. (Jan. 2003a). Interstellar Dust Grains. 41, pp. 241–289. DOI: 10.1146/annurev.astro.41.011802.094840. arXiv: astro-ph/0304489 [astro-ph].

— (Dec. 2003b). Scattering by Interstellar Dust Grains. I. Optical and Ultraviolet. 598.2, pp. 1017–1025. DOI: 10.1086/379118. arXiv: astro-ph/0304060 [astro-ph].

Goto, Tomotsugu et al. (June 2003). Hδ-Strong Galaxies in the Sloan Digital Sky Survey: I. The Catalog. 55, pp. 771–787. DOI: 10.1093/pasj/55.4.771. arXiv: astro-ph/0301305 [astro-ph].

Hopkins, A. M. et al. (Dec. 2003). Star Formation Rate Indicators in the Sloan Digital Sky Survey. 599.2, pp. 971–991. DOI: 10.1086/379608. arXiv: astro-ph/0306621 [astro-ph].

Lambas, Diego G. et al. (Dec. 2003). Galaxy pairs in the 2dF survey - I. Effects of interactions on star formation in the field. 346.4, pp. 1189–1196. DOI: 10.1111/j.1365-2966.2003.07179.x. arXiv: astro-ph/0212222 [astro-ph].

Le Fèvre, Oliver et al. (Mar. 2003). Commissioning and performances of the VLT-VIMOS instrument. *Instrument Design and Performance for Optical/Infrared Ground-based Telescopes*. Ed. by Masanori Iye et al. Vol. 4841. Society of Photo-Optical Instrumentation Engineers (SPIE) Conference Series, pp. 1670–1681. DOI: 10.1117/12.460959.

Neri, R. et al. (Nov. 2003). Interferometric Observations of Powerful CO Emission from Three Submillimeter Galaxies at z=2.39, 2.51, and 3.35. 597.2, pp. L113–L116. DOI: 10.1086/379968. arXiv: astro-ph/0307310 [astro-ph].

Alonso, M. Sol et al. (Aug. 2004). Galaxy pairs in the 2dF survey - II. Effects of interactions on star formation in groups and clusters. 352.3, pp. 1081–1088. DOI: 10.1111/j.1365-2966.2004.08002.x. arXiv: astro-ph/0401455 [astro-ph].

Brinchmann, J. et al. (July 2004). The physical properties of star-forming galaxies in the low-redshift Universe. 351.4, pp. 1151–1179. DOI: 10.1111/j.1365-2966.2004.07881.x. arXiv: astro-ph/0311060 [astro-ph].

Cappellari, Michele et al. (Feb. 2004). Parametric Recovery of Line-of-Sight Velocity Distributions from Absorption-Line Spectra of Galaxies via Penalized Likelihood. 116.816, pp. 138–147. DOI: 10.1086/381875. arXiv: astro-ph/0312201 [astro-ph].

Rieke, G. H. et al. (Sept. 2004). The Multiband Imaging Photometer for Spitzer (MIPS). 154.1, pp. 25–29. DOI: 10.1086/422717.

Tremonti, Christy A. et al. (Oct. 2004). The Origin of the Mass-Metallicity Relation: Insights from 53 000 Star-forming Galaxies in the Sloan Digital Sky Survey. 613.2, pp. 898–913. DOI: 10.1086/423264. arXiv: astro-ph/0405537 [astro-ph].

Burgarella, D. et al. (July 2005). Star formation and dust attenuation properties in galaxies from a statistical ultraviolet-to-far-infrared analysis. 360.4, pp. 1413–1425. DOI: 10.1111/j.1365-2966.2005.09131.x. arXiv: astro-ph/0504434 [astro-ph].

Chapman, S. C. et al. (Apr. 2005). A Redshift Survey of the Submillimeter Galaxy Population. 622.2, pp. 772–796. DOI: 10.1086/428082. arXiv: astro-ph/0412573 [astro-ph].

Daddi, E. et al. (June 2005). Passively Evolving Early-Type Galaxies at 1.4 <~z <~2.5 in the Hubble Ultra Deep Field. 626.2, pp. 680–697. DOI: 10.1086/430104. arXiv: astro-ph/0503102 [astro-ph].

Greve, T. R. et al. (May 2005). An interferometric CO survey of luminous submillimetre galaxies. 359.3, pp. 1165–1183. DOI: 10.1111/j.1365-2966.2005.08979.x. arXiv: astro-ph/0503055 [astro-ph].

Takeuchi, T. T. et al. (Sept. 2005). The evolution of the ultraviolet and infrared luminosity densities in the universe at 0 < z < 1. 440.2, pp. L17–L20. DOI: 10.1051/0004-6361: 200500158. arXiv: astro-ph/0508124 [astro-ph].

Fritz, J. et al. (Mar. 2006). Revisiting the infrared spectra of active galactic nuclei with a new torus emission model. 366.3, pp. 767–786. DOI: 10.1111/j.1365-2966.2006.09866.x. arXiv: astro-ph/0511428 [astro-ph].

Gallazzi, Anna et al. (Aug. 2006). Ages and metallicities of early-type galaxies in the Sloan Digital Sky Survey: new insight into the physical origin of the colour-magnitude and the Mg_2-σ_V relations. 370.3, pp. 1106–1124. DOI: 10.1111/j.1365-2966.2006.10548.x. arXiv: astro-ph/0605300 [astro-ph].

Hopkins, Andrew M. et al. (Nov. 2006). On the Normalization of the Cosmic Star Formation History. 651.1, pp. 142–154. DOI: 10.1086/506610. arXiv: astro-ph/0601463 [astro-ph].

Maraston, C. et al. (Nov. 2006). Evidence for TP-AGB Stars in High-Redshift Galaxies, and Their Effect on Deriving Stellar Population Parameters. 652.1, pp. 85–96. DOI: 10.1086/508143. arXiv: astro-ph/0604530 [astro-ph].

Nagao, T. et al. (Nov. 2006). Gas metallicity diagnostics in star-forming galaxies. 459.1, pp. 85–101. DOI: 10.1051/0004-6361:20065216. arXiv: astro-ph/0603580 [astro-ph].

Tacconi, L. J. et al. (Mar. 2006). High-Resolution Millimeter Imaging of Submillimeter Galaxies. 640.1, pp. 228–240. DOI: 10.1086/499933. arXiv: astro-ph/0511319 [astro-ph].

Burgarella, D. et al. (Sept. 2007). Lyman break galaxies at z ~1 and the evolution of dust attenuation in star-forming galaxies with redshift. 380.3, pp. 986–998. DOI: 10.1111/j.1365-2966.2007.12063.x. arXiv: 0706.0810 [astro-ph].

Daddi, E. et al. (Nov. 2007). Multiwavelength Study of Massive Galaxies at z~2. I. Star Formation and Galaxy Growth. 670.1, pp. 156–172. DOI: 10.1086/521818. arXiv: 0705.2831 [astro-ph].

Draine, B. T. et al. (Mar. 2007). Infrared Emission from Interstellar Dust. IV. The Silicate-Graphite-PAH Model in the Post-Spitzer Era. 657.2, pp. 810–837. DOI: 10.1086/511055. arXiv: astro-ph/0608003 [astro-ph].

Dwek, Eli et al. (June 2007). The Evolution of Dust in the Early Universe with Applications to the Galaxy SDSS J1148+5251. 662.2, pp. 927–939. DOI: 10.1086/518430. arXiv: 0705.3799 [astro-ph].

Johnson, Benjamin D. et al. (Dec. 2007). Ultraviolet through Infrared Spectral Energy Distributions from 1000 SDSS Galaxies: Dust Attenuation. 173.2, pp. 392–403. DOI: 10.1086/522960. arXiv: 0712.3573 [astro-ph].

Kennicutt Robert C., Jr. et al. (Dec. 2007). Star Formation in NGC 5194 (M51a). II. The Spatially Resolved Star Formation Law. 671.1, pp. 333–348. DOI: 10.1086/522300. arXiv: 0708.0922 [astro-ph].

Lebouteiller, V. et al. (Aug. 2007). PAH Strength and the Interstellar Radiation Field around the Massive Young Cluster NGC 3603. 665.1, pp. 390–401. DOI: 10.1086/519014. arXiv: 0704.2068 [astro-ph].

McMullin, J. P. et al. (Oct. 2007). CASA Architecture and Applications. *Astronomical Data Analysis Software and Systems XVI*. Ed. by R. A. Shaw et al. Vol. 376. Astronomical Society of the Pacific Conference Series, p. 127.

Noeske, K. G. et al. (May 2007). Star Formation in AEGIS Field Galaxies since z=1.1: The Dominance of Gradually Declining Star Formation, and the Main Sequence of Star-forming Galaxies. 660.1, pp. L43–L46. DOI: `10.1086/517926`. arXiv: `astro-ph/0701924 [astro-ph]`.

Salim, Samir et al. (Dec. 2007). UV Star Formation Rates in the Local Universe. 173.2, pp. 267–292. DOI: `10.1086/519218`. arXiv: `0704.3611 [astro-ph]`.

Scoville, N. et al. (Sept. 2007). The Cosmic Evolution Survey (COSMOS): Overview. 172.1, pp. 1–8. DOI: `10.1086/516585`. arXiv: `astro-ph/0612305 [astro-ph]`.

Sparke, Linda S. et al. (2007). *Galaxies in the Universe: An Introduction*. 2nd ed. Cambridge University Press. DOI: `10.1017/CBO9780511807237`.

Cimatti, A. et al. (Apr. 2008). GMASS ultradeep spectroscopy of galaxies at z ∼2. II. Super-dense passive galaxies: how did they form and evolve? 482.1, pp. 21–42. DOI: `10.1051/0004-6361:20078739`. arXiv: `0801.1184 [astro-ph]`.

Coil, Alison L. et al. (Jan. 2008). The DEEP2 Galaxy Redshift Survey: Color and Luminosity Dependence of Galaxy Clustering at z ∼1. 672.1, pp. 153–176. DOI: `10.1086/523639`. arXiv: `0708.0004 [astro-ph]`.

da Cunha, Elisabete et al. (Aug. 2008). A simple model to interpret the ultraviolet, optical and infrared emission from galaxies. 388.4, pp. 1595–1617. DOI: `10.1111/j.1365-2966.2008.13535.x`. arXiv: `0806.1020 [astro-ph]`.

Panter, Benjamin et al. (Dec. 2008). The cosmic evolution of metallicity from the SDSS fossil record. 391.3, pp. 1117–1126. DOI: `10.1111/j.1365-2966.2008.13981.x`. arXiv: `0804.3091 [astro-ph]`.

Zhu, Yi-Nan et al. (Oct. 2008). Correlations between Mid-Infrared, Far-Infrared, Hα, and FUV Luminosities for Spitzer SWIRE Field Galaxies. 686.1, pp. 155–171. DOI: `10.1086/591121`.

Boquien, M. et al. (Nov. 2009). Star-Forming or Starbursting? The Ultraviolet Conundrum. 706.1, pp. 553–570. DOI: `10.1088/0004-637X/706/1/553`. arXiv: `0910.0774 [astro-ph.CO]`.

Cattaneo, A. et al. (July 2009). The role of black holes in galaxy formation and evolution. 460.7252, pp. 213–219. DOI: `10.1038/nature08135`. arXiv: `0907.1608 [astro-ph.CO]`.

Ilbert, O. et al. (Jan. 2009). Cosmos Photometric Redshifts with 30-Bands for 2-deg^2. 690.2, pp. 1236–1249. DOI: `10.1088/0004-637X/690/2/1236`. arXiv: `0809.2101 [astro-ph]`.

Kennicutt Robert C., Jr. et al. (Oct. 2009). Dust-corrected Star Formation Rates of Galaxies. I. Combinations of Hα and Infrared Tracers. 703.2, pp. 1672–1695. DOI: `10.1088/0004-637X/703/2/1672`. arXiv: `0908.0203 [astro-ph.CO]`.

Law, David R. et al. (June 2009). The Kiloparsec-scale Kinematics of High-redshift Star-forming Galaxies. 697.2, pp. 2057–2082. DOI: `10.1088/0004-637X/697/2/2057`. arXiv: `0901.2930 [astro-ph.GA]`.

Lilly, Simon J. et al. (Oct. 2009). The zCOSMOS 10k-Bright Spectroscopic Sample. 184.2, pp. 218–229. DOI: `10.1088/0067-0049/184/2/218`.

Muzzin, Adam et al. (Aug. 2009). A Near-Infrared Spectroscopic Survey of K-Selected Galaxies at z∼2.3: Comparison of Stellar Population Synthesis Codes and Constraints from the Rest-Frame NIR. 701.2, pp. 1839–1864. DOI: `10.1088/0004-637X/701/2/1839`. arXiv: `0906.2012 [astro-ph.CO]`.

Noll, S. et al. (Dec. 2009). Analysis of galaxy spectral energy distributions from far-UV to far-IR with CIGALE: studying a SINGS test sample. 507.3, pp. 1793–1813. DOI: `10.1051/0004-6361/200912497`. arXiv: `0909.5439 [astro-ph.CO]`.

Rieke, G. H. et al. (Feb. 2009). Determining Star Formation Rates for Infrared Galaxies. 692.1, pp. 556–573. DOI: 10.1088/0004-637X/692/1/556. arXiv: 0810.4150 [astro-ph].

Zibetti, Stefano et al. (Dec. 2009). Resolved stellar mass maps of galaxies - I. Method and implications for global mass estimates. 400.3, pp. 1181–1198. DOI: 10.1111/j.1365-2966.2009.15528.x. arXiv: 0904.4252 [astro-ph.CO].

Conroy, Charlie et al. (July 2010). Dust Attenuation in Disk-dominated Galaxies: Evidence for the 2175 Å Dust Feature. 718.1, pp. 184–198. DOI: 10.1088/0004-637X/718/1/184. arXiv: 1003.2202 [astro-ph.CO].

Daddi, E. et al. (May 2010). Different Star Formation Laws for Disks Versus Starbursts at Low and High Redshifts. 714.1, pp. L118–L122. DOI: 10.1088/2041-8205/714/1/L118. arXiv: 1003.3889 [astro-ph.CO].

Garilli, B. et al. (July 2010). EZ: A Tool For Automatic Redshift Measurement. 122.893, p. 827. DOI: 10.1086/654903. arXiv: 1005.2825 [astro-ph.IM].

Genzel, R. et al. (Oct. 2010). A study of the gas-star formation relation over cosmic time. 407.4, pp. 2091–2108. DOI: 10.1111/j.1365-2966.2010.16969.x. arXiv: 1003.5180 [astro-ph.CO].

Gilbank, David G. et al. (July 2010). The local star formation rate density: assessing calibrations using [OII], H and UV luminosities. 405.4, pp. 2594–2614. DOI: 10.1111/j.1365-2966.2010.16640.x. arXiv: 1002.3172 [astro-ph.CO].

Lamareille, F. (Jan. 2010). Spectral classification of emission-line galaxies from the Sloan Digital Sky Survey. I. An improved classification for high-redshift galaxies. 509, A53, A53. DOI: 10.1051/0004-6361/200913168. arXiv: 0910.4814 [astro-ph.CO].

Peng, Ying-jie et al. (Sept. 2010). Mass and Environment as Drivers of Galaxy Evolution in SDSS and zCOSMOS and the Origin of the Schechter Function. 721.1, pp. 193–221. DOI: 10.1088/0004-637X/721/1/193. arXiv: 1003.4747 [astro-ph.CO].

Tacconi, L. J. et al. (Feb. 2010). High molecular gas fractions in normal massive star-forming galaxies in the young Universe. 463.7282, pp. 781–784. DOI: 10.1038/nature08773. arXiv: 1002.2149 [astro-ph.CO].

Takagi, T. et al. (May 2010). Polycyclic aromatic hydrocarbon (PAH) luminous galaxies at z ~1. 514, A5, A5. DOI: 10.1051/0004-6361/200913466. arXiv: 1002.3654 [astro-ph.CO].

Takeuchi, T. T. et al. (May 2010). Star formation and dust extinction properties of local galaxies from the AKARI-GALEX all-sky surveys . First results from the most secure multiband sample from the far-ultraviolet to the far-infrared. 514, A4, A4. DOI: 10.1051/0004-6361/200913476. arXiv: 0912.5051 [astro-ph.CO].

Vazdekis, A. et al. (June 2010). Evolutionary stellar population synthesis with MILES - I. The base models and a new line index system. 404.4, pp. 1639–1671. DOI: 10.1111/j.1365-2966.2010.16407.x. arXiv: 1004.4439 [astro-ph.CO].

Arnouts, S. et al. (Aug. 2011). LePHARE: Photometric Analysis for Redshift Estimate (ascl:1108.009). ascl: 1108.009.

Buat, V. et al. (Sept. 2011). GOODS-Herschel: evidence of a UV extinction bump in galaxies at z > 1. 533, A93, A93. DOI: 10.1051/0004-6361/201117264. arXiv: 1107.1049 [astro-ph.CO].

Elbaz, D. et al. (Sept. 2011). GOODS-Herschel: an infrared main sequence for star-forming galaxies. 533, A119, A119. DOI: 10.1051/0004-6361/201117239. arXiv: 1105.2537 [astro-ph.CO].

Gielen, C. et al. (Dec. 2011). Carbonaceous molecules in the oxygen-rich circumstellar environment of binary post-AGB stars. C_{60} fullerenes and polycyclic aromatic hydrocarbons. 536, A54, A54. DOI: 10.1051/0004-6361/201117961. arXiv: 1110.5996 [astro-ph.SR].

Glover, S. C. O. et al. (Mar. 2011). On the relationship between molecular hydrogen and carbon monoxide abundances in molecular clouds. 412.1, pp. 337–350. DOI: 10.1111/j.1365-2966.2010.17907.x. arXiv: 1003.1340 [astro-ph.GA].

Hainline, Laura J. et al. (Oct. 2011). The Stellar Mass Content of Submillimeter-selected Galaxies. 740.2, 96, p. 96. DOI: 10.1088/0004-637X/740/2/96. arXiv: 1006.0238 [astro-ph.CO].

Hao, Cai-Na et al. (2011). DUST-CORRECTED STAR FORMATION RATES OF GALAXIES. II. COMBINATIONS OF ULTRAVIOLET AND INFRARED TRACERS. 741.2, p. 124. DOI: 10.1088/0004-637X/741/2/124. URL: https://dx.doi.org/10.1088/0004-637X/741/2/124.

Komatsu, E. et al. (Feb. 2011). Seven-year Wilkinson Microwave Anisotropy Probe (WMAP) Observations: Cosmological Interpretation. 192.2, 18, p. 18. DOI: 10.1088/0067-0049/192/2/18. arXiv: 1001.4538 [astro-ph.CO].

Lutz, D. et al. (Aug. 2011). PACS Evolutionary Probe (PEP) - A Herschel key program. 532, A90, A90. DOI: 10.1051/0004-6361/201117107. arXiv: 1106.3285 [astro-ph.CO].

Mendez, Alexander J. et al. (Aug. 2011). AEGIS: The Morphologies of Green Galaxies at $0.4 < z < 1.2$. 736.2, 110, p. 110. DOI: 10.1088/0004-637X/736/2/110. arXiv: 1101.3353 [astro-ph.CO].

Murphy, E. J. et al. (May 2011). An Accounting of the Dust-obscured Star Formation and Accretion Histories Over the Last ⁓11 Billion Years. 732.2, 126, p. 126. DOI: 10.1088/0004-637X/732/2/126. arXiv: 1102.3920 [astro-ph.CO].

Overzier, Roderik A. et al. (Jan. 2011). Dust Attenuation in UV-selected Starbursts at High Redshift and Their Local Counterparts: Implications for the Cosmic Star Formation Rate Density. 726.1, L7, p. L7. DOI: 10.1088/2041-8205/726/1/L7. arXiv: 1011.6098 [astro-ph.CO].

Rodighiero, G. et al. (Oct. 2011). The Lesser Role of Starbursts in Star Formation at $z = 2$. 739.2, L40, p. L40. DOI: 10.1088/2041-8205/739/2/L40. arXiv: 1108.0933 [astro-ph.CO].

Taylor, Edward N. et al. (Dec. 2011). Galaxy And Mass Assembly (GAMA): stellar mass estimates. *Monthly Notices of the Royal Astronomical Society* 418.3, pp. 1587–1620. ISSN: 0035-8711. DOI: 10.1111/j.1365-2966.2011.19536.x. eprint: https://academic.oup.com/mnras/article-pdf/418/3/1587/18437265/mnras0418-1587.pdf. URL: https://doi.org/10.1111/j.1365-2966.2011.19536.x.

Wild, Vivienne et al. (Nov. 2011). Empirical determination of the shape of dust attenuation curves in star-forming galaxies. 417.3, pp. 1760–1786. DOI: 10.1111/j.1365-2966.2011.19367.x. arXiv: 1106.1646 [astro-ph.CO].

Boquien, M. et al. (Mar. 2012). The IRX-β relation on subgalactic scales in star-forming galaxies of the Herschel Reference Survey. 539, A145, A145. DOI: 10.1051/0004-6361/201118624. arXiv: 1201.2405 [astro-ph.CO].

Bouwens, R. J. et al. (Aug. 2012). UV-continuum Slopes at z ⁓4-7 from the HUDF09+ERS+CANDELS Observations: Discovery of a Well-defined UV Color-Magnitude Relationship for $z >= 4$ Star-forming Galaxies. 754.2, 83, p. 83. DOI: 10.1088/0004-637X/754/2/83. arXiv: 1109.0994 [astro-ph.CO].

Buat, V. et al. (Sept. 2012). GOODS-Herschel: dust attenuation properties of UV selected high redshift galaxies. 545, A141, A141. DOI: 10.1051/0004-6361/201219405. arXiv: 1207.3528 [astro-ph.CO].

Casey, Caitlin M. (Oct. 2012). Far-infrared spectral energy distribution fitting for galaxies near and far. 425.4, pp. 3094–3103. DOI: 10.1111/j.1365-2966.2012.21455.x. arXiv: 1206.1595 [astro-ph.CO].

Hopkins, Philip F. et al. (Apr. 2012). Stellar feedback in galaxies and the origin of galaxy-scale winds. *Monthly Notices of the Royal Astronomical Society* 421.4, pp. 3522–3537.

ISSN: 0035-8711. DOI: 10.1111/j.1365-2966.2012.20593.x. eprint: https://academic.oup.com/mnras/article-pdf/421/4/3522/3835045/mnras0421-3522.pdf. URL: https://doi.org/10.1111/j.1365-2966.2012.20593.x.

Hudelot, P. et al. (Sept. 2012). VizieR Online Data Catalog: The CFHTLS Survey (T0007 release) (Hudelot+ 2012). *VizieR Online Data Catalog*, II/317, pp. II/317.

Ichikawa, Takashi et al. (May 2012). A universal stellar mass-size relation of galaxies in the GOODS-North region. 422.2, pp. 1014–1027. DOI: 10.1111/j.1365-2966.2012.20674.x. arXiv: 1202.1138 [astro-ph.CO].

Kennicutt, Robert C. et al. (2012). Star Formation in the Milky Way and Nearby Galaxies. *Annual Review of Astronomy and Astrophysics* 50.1, pp. 531–608. DOI: 10.1146/annurev-astro-081811-125610. eprint: https://doi.org/10.1146/annurev-astro-081811-125610. URL: https://doi.org/10.1146/annurev-astro-081811-125610.

Magdis, Georgios E. et al. (Nov. 2012). The Evolving Interstellar Medium of Star-forming Galaxies since z = 2 as Probed by Their Infrared Spectral Energy Distributions. 760.1, 6, p. 6. DOI: 10.1088/0004-637X/760/1/6. arXiv: 1210.1035 [astro-ph.CO].

Martí-Vidal, I. et al. (May 2012). Over-resolution of compact sources in interferometric observations. 541, A135, A135. DOI: 10.1051/0004-6361/201118334. arXiv: 1203.2071 [astro-ph.IM].

Masaki, Shogo et al. (June 2012). Distribution of dust around galaxies: an analytic model. 423.1, pp. L117–L121. DOI: 10.1111/j.1745-3933.2012.01268.x. arXiv: 1203.6414 [astro-ph.CO].

Michałowski, M. J. et al. (May 2012). The stellar masses and specific star-formation rates of submillimetre galaxies. 541, A85, A85. DOI: 10.1051/0004-6361/201016308. arXiv: 1108.6058 [astro-ph.CO].

Oliver, S. J. et al. (Aug. 2012). The Herschel Multi-tiered Extragalactic Survey: HerMES. 424.3, pp. 1614–1635. DOI: 10.1111/j.1365-2966.2012.20912.x. arXiv: 1203.2562 [astro-ph.CO].

Pforr, Janine et al. (May 2012). Recovering galaxy stellar population properties from broadband spectral energy distribution fitting. *Monthly Notices of the Royal Astronomical Society* 422.4, pp. 3285–3326. ISSN: 0035-8711. DOI: 10.1111/j.1365-2966.2012.20848.x. eprint: https://academic.oup.com/mnras/article-pdf/422/4/3285/18603204/mnras0422-3285.pdf. URL: https://doi.org/10.1111/j.1365-2966.2012.20848.x.

Shull, J. Michael et al. (Nov. 2012). The Baryon Census in a Multiphase Intergalactic Medium: 30% of the Baryons May Still be Missing. 759.1, 23, p. 23. DOI: 10.1088/0004-637X/759/1/23. arXiv: 1112.2706 [astro-ph.CO].

Takeuchi, Tsutomu T. et al. (Aug. 2012). Reexamination of the Infrared Excess-Ultraviolet Slope Relation of Local Galaxies. 755.2, 144, p. 144. DOI: 10.1088/0004-637X/755/2/144. arXiv: 1206.3905 [astro-ph.CO].

Asano, Ryosuke S. et al. (June 2013). What determines the grain size distribution in galaxies? 432.1, pp. 637–652. DOI: 10.1093/mnras/stt506. arXiv: 1303.5528 [astro-ph.GA].

Behroozi, Peter S. et al. (June 2013). The Average Star Formation Histories of Galaxies in Dark Matter Halos from z = 0-8. 770.1, 57, p. 57. DOI: 10.1088/0004-637X/770/1/57. arXiv: 1207.6105 [astro-ph.CO].

Bolatto, Alberto D. et al. (Aug. 2013). The CO-to-H_2 Conversion Factor. 51.1, pp. 207–268. DOI: 10.1146/annurev-astro-082812-140944. arXiv: 1301.3498 [astro-ph.GA].

Bothwell, M. S. et al. (Mar. 2013a). A survey of molecular gas in luminous sub-millimetre galaxies. 429.4, pp. 3047–3067. DOI: 10.1093/mnras/sts562. arXiv: 1205.1511 [astro-ph.CO].

Bothwell, M. S. et al. (Dec. 2013b). SPT 0538-50: Physical Conditions in the Interstellar Medium of a Strongly Lensed Dusty Star-forming Galaxy at z = 2.8. 779.1, 67, p. 67. DOI: 10.1088/0004-637X/779/1/67. arXiv: 1309.3275 [astro-ph.CO].

Buat, V. (Oct. 2013). Dust attenuation in galaxies up to redshift 2. *Earth, Planets and Space* 65.10, pp. 1095–1100. DOI: 10.5047/eps.2013.02.001.

Carilli, C. L. et al. (2013). Cool Gas in High-Redshift Galaxies. 51.1, pp. 105–161. DOI: 10.1146/annurev-astro-082812-140953. arXiv: 1301.0371 [astro-ph.CO].

Conroy, Charlie (Aug. 2013). Modeling the Panchromatic Spectral Energy Distributions of Galaxies. 51.1, pp. 393–455. DOI: 10.1146/annurev-astro-082812-141017. arXiv: 1301.7095 [astro-ph.CO].

Dubois, Yohan et al. (Aug. 2013). AGN-driven quenching of star formation: morphological and dynamical implications for early-type galaxies. 433.4, pp. 3297–3313. DOI: 10.1093/mnras/stt997. arXiv: 1301.3092 [astro-ph.CO].

Hilton, Matt et al. (Nov. 2013). The Atacama Cosmology Telescope: the stellar content of galaxy clusters selected using the Sunyaev-Zel'dovich effect. 435.4, pp. 3469–3480. DOI: 10.1093/mnras/stt1535. arXiv: 1301.0780 [astro-ph.CO].

Hirashita, Hiroyuki et al. (Oct. 2013). Evolution of dust grain size distribution by shattering in the interstellar medium: Robustness and uncertainty. *Earth, Planets and Space* 65.10, pp. 1083–1094. DOI: 10.5047/eps.2013.03.008. arXiv: 1303.3958 [astro-ph.GA].

Ilbert, O. et al. (Aug. 2013). Mass assembly in quiescent and star-forming galaxies since z 4 from UltraVISTA. 556, A55, A55. DOI: 10.1051/0004-6361/201321100. arXiv: 1301.3157 [astro-ph.CO].

Kriek, Mariska et al. (Sept. 2013). The Dust Attenuation Law in Distant Galaxies: Evidence for Variation with Spectral Type. 775.1, L16, p. L16. DOI: 10.1088/2041-8205/775/1/L16. arXiv: 1308.1099 [astro-ph.CO].

Tacconi, L. J. et al. (May 2013). Phibss: Molecular Gas Content and Scaling Relations in z ~1-3 Massive, Main-sequence Star-forming Galaxies. 768.1, 74, p. 74. DOI: 10.1088/0004-637X/768/1/74. arXiv: 1211.5743 [astro-ph.CO].

van der Burg, R. F. J. et al. (Sept. 2013). The environmental dependence of the stellar mass function at z ~1. Comparing cluster and field between the GCLASS and UltraVISTA surveys. 557, A15, A15. DOI: 10.1051/0004-6361/201321237. arXiv: 1304.5525 [astro-ph.CO].

Viero, M. P. et al. (July 2013). HerMES: Cosmic Infrared Background Anisotropies and the Clustering of Dusty Star-forming Galaxies. 772.1, 77, p. 77. DOI: 10.1088/0004-637X/772/1/77. arXiv: 1208.5049 [astro-ph.CO].

Weiß, A. et al. (Oct. 2013a). A Redshift Survey of Strongly Lensed Submm Galaxies Based on Molecular Emission Lines Observed with ALMA. *New Trends in Radio Astronomy in the ALMA Era: The 30th Anniversary of Nobeyama Radio Observatory*. Ed. by R. Kawabe et al. Vol. 476. Astronomical Society of the Pacific Conference Series, p. 33.

Weiß, A. et al. (Apr. 2013b). ALMA Redshifts of Millimeter-selected Galaxies from the SPT Survey: The Redshift Distribution of Dusty Star-forming Galaxies. 767.1, 88, p. 88. DOI: 10.1088/0004-637X/767/1/88. arXiv: 1303.2726 [astro-ph.CO].

Whitaker, Katherine E. et al. (June 2013). Quiescent Galaxies in the 3D-HST Survey: Spectroscopic Confirmation of a Large Number of Galaxies with Relatively Old Stellar Populations at z ~2. 770.2, L39, p. L39. DOI: 10.1088/2041-8205/770/2/L39. arXiv: 1305.1943 [astro-ph.CO].

Béthermin, Matthieu et al. (July 2014). Clustering, host halos, and environment of z ~2 galaxies as a function of their physical properties. 567, A103, A103. DOI: 10.1051/0004-6361/201423451. arXiv: 1405.0492 [astro-ph.GA].

Buat, V. et al. (Jan. 2014). Ultraviolet to infrared emission of z > 1 galaxies: Can we derive reliable star formation rates and stellar masses? 561, A39, A39. DOI: 10.1051/0004-6361/201322081. arXiv: 1310.7712 [astro-ph.CO].

Casey, C. M. et al. (Dec. 2014). Are Dusty Galaxies Blue? Insights on UV Attenuation from Dust-selected Galaxies. 796.2, 95, p. 95. DOI: 10.1088/0004-637X/796/2/95. arXiv: 1410.0702 [astro-ph.GA].

Ciesla, L. et al. (May 2014). Dust spectral energy distributions of nearby galaxies: an insight from the Herschel Reference Survey. 565, A128, A128. DOI: 10.1051/0004-6361/201323248. arXiv: 1402.3597 [astro-ph.GA].

Draine, B. T. et al. (Jan. 2014). Andromeda's Dust. 780.2, 172, p. 172. DOI: 10.1088/0004-637X/780/2/172. arXiv: 1306.2304 [astro-ph.CO].

Garilli, B. et al. (Feb. 2014). The VIMOS Public Extragalactic Survey (VIPERS). First Data Release of 57 204 spectroscopic measurements. 562, A23, A23. DOI: 10.1051/0004-6361/201322790. arXiv: 1310.1008 [astro-ph.CO].

Guzzo, L. et al. (June 2014). The VIMOS Public Extragalactic Redshift Survey (VIPERS). An unprecedented view of galaxies and large-scale structure at $0.5 < z < 1.2$. 566, A108, A108. DOI: 10.1051/0004-6361/201321489. arXiv: 1303.2623 [astro-ph.CO].

Hirashita, Hiroyuki et al. (Sept. 2014). Constraining dust formation in high-redshift young galaxies. 443.2, pp. 1704–1712. DOI: 10.1093/mnras/stu1290. arXiv: 1406.6762 [astro-ph.GA].

Madau, Piero et al. (2014). Cosmic Star-Formation History. 52, pp. 415–486. DOI: 10.1146/annurev-astro-081811-125615. arXiv: 1403.0007 [astro-ph.CO].

Magnelli, B. et al. (Jan. 2014). The evolution of the dust temperatures of galaxies in the SFR-M_* plane up to $z \sim 2$. 561, A86, A86. DOI: 10.1051/0004-6361/201322217. arXiv: 1311.2956 [astro-ph.CO].

Małek, K. et al. (Feb. 2014). Properties of star forming galaxies in AKARI Deep Field-South. 562, A15, A15. DOI: 10.1051/0004-6361/201321665. arXiv: 1312.0765 [astro-ph.GA].

McGee, Sean L. et al. (Jan. 2014). The stellar mass function and efficiency of galaxy formation with a varying initial mass function. *Monthly Notices of the Royal Astronomical Society* 438.4, pp. 3188–3204. ISSN: 0035-8711. DOI: 10.1093/mnras/stt2426. eprint: https://academic.oup.com/mnras/article-pdf/438/4/3188/3836756/stt2426.pdf. URL: https://doi.org/10.1093/mnras/stt2426.

Meidt, Sharon E. et al. (June 2014). Reconstructing the Stellar Mass Distributions of Galaxies Using S^{4}G IRAC 3.6 and 4.5 μm Images. II. The Conversion from Light to Mass. 788.2, 144, p. 144. DOI: 10.1088/0004-637X/788/2/144. arXiv: 1402.5210 [astro-ph.GA].

Nayyeri, H. et al. (Oct. 2014). A Study of Massive and Evolved Galaxies at High Redshift. 794.1, 68, p. 68. DOI: 10.1088/0004-637X/794/1/68. arXiv: 1408.3684 [astro-ph.GA].

Perret, V. et al. (Feb. 2014). Evolution of the mass, size, and star formation rate in high redshift merging galaxies. MIRAGE - A new sample of simulations with detailed stellar feedback. 562, A1, A1. DOI: 10.1051/0004-6361/201322395. arXiv: 1307.7130 [astro-ph.CO].

Sánchez Almeida, Jorge et al. (July 2014). Star formation sustained by gas accretion. 22, 71, p. 71. DOI: 10.1007/s00159-014-0071-1. arXiv: 1405.3178 [astro-ph.GA].

Santini, P. et al. (Feb. 2014). The evolution of the dust and gas content in galaxies. 562, A30, A30. DOI: 10.1051/0004-6361/201322835. arXiv: 1311.3670 [astro-ph.CO].

Sargent, M. T. et al. (Sept. 2014). Regularity Underlying Complexity: A Redshift-independent Description of the Continuous Variation of Galaxy-scale Molecular Gas Properties in the

Mass-star Formation Rate Plane. 793.1, 19, p. 19. DOI: `10.1088/0004-637X/793/1/19`. arXiv: `1303.4392 [astro-ph.CO]`.

Seok, Ji Yeon et al. (Apr. 2014). Formation history of polycyclic aromatic hydrocarbons in galaxies. 439.2, pp. 2186–2196. DOI: `10.1093/mnras/stu120`. arXiv: `1401.3943 [astro-ph.GA]`.

Speagle, J. S. et al. (Oct. 2014). A Highly Consistent Framework for the Evolution of the Star-Forming "Main Sequence" from z ∼0-6. 214.2, 15, p. 15. DOI: `10.1088/0067-0049/214/2/15`. arXiv: `1405.2041 [astro-ph.GA]`.

Toft, S. et al. (Feb. 2014). Submillimeter Galaxies as Progenitors of Compact Quiescent Galaxies. 782.2, 68, p. 68. DOI: `10.1088/0004-637X/782/2/68`. arXiv: `1401.1510 [astro-ph.GA]`.

Béthermin, Matthieu et al. (2015). Evolution of the dust emission of massive galaxies up to z= 4 and constraints on their dominant mode of star formation. *A&A* 573, A113.

Ciesla, L. et al. (Apr. 2015). Constraining the properties of AGN host galaxies with spectral energy distribution modelling. 576, A10, A10. DOI: `10.1051/0004-6361/201425252`. arXiv: `1501.03672 [astro-ph.GA]`.

Clark, Paul C. et al. (Sept. 2015). Does the CO-to-H_2 conversion factor depend on the star formation rate? 452.2, pp. 2057–2070. DOI: `10.1093/mnras/stv1369`. arXiv: `1506.06503 [astro-ph.GA]`.

Daddi, E. et al. (May 2015). CO excitation of normal star-forming galaxies out to z = 1.5 as regulated by the properties of their interstellar medium. 577, A46, A46. DOI: `10.1051/0004-6361/201425043`. arXiv: `1409.8158 [astro-ph.GA]`.

Gruppioni, C. et al. (Aug. 2015). Star formation in Herschel's Monsters versus semi-analytic models. 451.4, pp. 3419–3426. DOI: `10.1093/mnras/stv1204`. arXiv: `1506.01518 [astro-ph.GA]`.

Guo, Yicheng et al. (2015). Clumpy Galaxies in CANDELS. I. The Definition of UV Clumps and the Fraction of Clumpy Galaxies at 0.5 < z < 3. 800.1, 39, p. 39. DOI: `10.1088/0004-637X/800/1/39`. arXiv: `1410.7398 [astro-ph.GA]`.

Guzman-Ramirez, L. et al. (July 2015). Witnessing the emergence of a carbon star. 451, pp. L1–L5. DOI: `10.1093/mnrasl/slv055`. arXiv: `1504.03349 [astro-ph.SR]`.

Lo Faro, B. et al. (Mar. 2015). Combining physical galaxy models with radio observations to constrain the SFRs of high-z dusty star-forming galaxies. 447.4, pp. 3442–3466. DOI: `10.1093/mnras/stu2593`. arXiv: `1412.3458 [astro-ph.GA]`.

Michałowski, Michał J. (May 2015). Dust production 680-850 million years after the Big Bang. 577, A80, A80. DOI: `10.1051/0004-6361/201525644`. arXiv: `1503.08210 [astro-ph.GA]`.

Narayanan, Desika et al. (Sept. 2015). The formation of submillimetre-bright galaxies from gas infall over a billion years. 525.7570, pp. 496–499. DOI: `10.1038/nature15383`. arXiv: `1509.06377 [astro-ph.GA]`.

Ruiz-Lara, T. et al. (Nov. 2015). Recovering star formation histories: Integrated-light analyses vs. stellar colour-magnitude diagrams. 583, A60, A60. DOI: `10.1051/0004-6361/201526752`. arXiv: `1509.02414 [astro-ph.GA]`.

Schreiber, C. et al. (2015). The Herschel view of the dominant mode of galaxy growth from z = 4 to the present day. 575, A74, A74. DOI: `10.1051/0004-6361/201425017`. arXiv: `1409.5433 [astro-ph.GA]`.

Scoville, Nick et al. (Feb. 2015). Dust Attenuation in High Redshift Galaxies: "Diamonds in the Sky". 800.2, 108, p. 108. DOI: `10.1088/0004-637X/800/2/108`. arXiv: `1412.8219 [astro-ph.GA]`.

Snaith, O. et al. (June 2015). Reconstructing the star formation history of the Milky Way disc(s) from chemical abundances. 578, A87, A87. DOI: `10.1051/0004-6361/201424281`. arXiv: `1410.3829 [astro-ph.GA]`.

Zeimann, Gregory R. et al. (Dec. 2015). The Dust Attenuation Curve versus Stellar Mass for Emission Line Galaxies at z ~2. 814.2, 162, p. 162. DOI: `10.1088/0004-637X/814/2/162`. arXiv: `1511.00651 [astro-ph.GA]`.

Álvarez-Márquez, J. et al. (Mar. 2016). Dust properties of Lyman-break galaxies at z ~3. 587, A122, A122. DOI: `10.1051/0004-6361/201527190`. arXiv: `1512.04120 [astro-ph.GA]`.

Ciesla, L. et al. (Jan. 2016). The imprint of rapid star formation quenching on the spectral energy distributions of galaxies. 585, A43, A43. DOI: `10.1051/0004-6361/201527107`. arXiv: `1510.07657 [astro-ph.GA]`.

Clauwens, Bart et al. (July 2016). Implications of a variable IMF for the interpretation of observations of galaxy populations. *Monthly Notices of the Royal Astronomical Society* 462.3, pp. 2832–2846. ISSN: 0035-8711. DOI: `10.1093/mnras/stw1808`. eprint: `https://academic.oup.com/mnras/article-pdf/462/3/2832/8009342/stw1808.pdf`. URL: `https://doi.org/10.1093/mnras/stw1808`.

Curti, M. et al. (June 2016). New fully empirical calibrations for strong-line metallicity indicators in star forming galaxies, 22. Ed. by S. F. Sanchez et al., p. 22.

Davidzon, I. et al. (Feb. 2016). The VIMOS Public Extragalactic Redshift Survey (VIPERS). Environmental effects shaping the galaxy stellar mass function. 586, A23, A23. DOI: `10.1051/0004-6361/201527129`. arXiv: `1511.01145 [astro-ph.GA]`.

Davies, L. J. M. et al. (Sept. 2016). GAMA/H-ATLAS: a meta-analysis of SFR indicators - comprehensive measures of the SFR-M_* relation and cosmic star formation history at z < 0.4. 461.1, pp. 458–485. DOI: `10.1093/mnras/stw1342`. arXiv: `1606.06299 [astro-ph.GA]`.

Ferrara, A. et al. (Nov. 2016). The problematic growth of dust in high-redshift galaxies. 463.1, pp. L112–L116. DOI: `10.1093/mnrasl/slw165`. arXiv: `1606.07214 [astro-ph.GA]`.

Hodge, J. A. et al. (Dec. 2016). Kiloparsec-scale Dust Disks in High-redshift Luminous Submillimeter Galaxies. 833.1, 103, p. 103. DOI: `10.3847/1538-4357/833/1/103`. arXiv: `1609.09649 [astro-ph.GA]`.

Laigle, C. et al. (June 2016). The COSMOS2015 Catalog: Exploring the 1 < z < 6 Universe with Half a Million Galaxies. 224.2, 24, p. 24. DOI: `10.3847/0067-0049/224/2/24`. arXiv: `1604.02350 [astro-ph.GA]`.

Moutard, T. et al. (May 2016). The VIPERS Multi-Lambda Survey. I. UV and near-IR observations, multi-colour catalogues, and photometric redshifts. 590, A102, A102. DOI: `10.1051/0004-6361/201527945`. arXiv: `1602.05915 [astro-ph.GA]`.

Pacifici, Camilla et al. (2016). THE EVOLUTION OF STAR FORMATION HISTORIES OF QUIESCENT GALAXIES. *The Astrophysical Journal* 832.1, p. 79. DOI: `10.3847/0004-637X/832/1/79`. URL: `https://dx.doi.org/10.3847/0004-637X/832/1/79`.

Rujopakarn, W. et al. (Dec. 2016). VLA and ALMA Imaging of Intense Galaxy-wide Star Formation in z ∼ 2 Galaxies. 833.1, 12, p. 12. DOI: `10.3847/0004-637X/833/1/12`. arXiv: `1607.07710 [astro-ph.GA]`.

Salmon, Brett et al. (Aug. 2016). Breaking the Curve with CANDELS: A Bayesian Approach to Reveal the Non-Universality of the Dust-Attenuation Law at High Redshift. 827.1, 20, p. 20. DOI: `10.3847/0004-637X/827/1/20`. arXiv: `1512.05396 [astro-ph.GA]`.

Shipley, Heath V. et al. (Feb. 2016). A New Star Formation Rate Calibration from Polycyclic Aromatic Hydrocarbon Emission Features and Application to High-redshift Galaxies. 818.1, 60, p. 60. DOI: `10.3847/0004-637X/818/1/60`. arXiv: `1601.01698 [astro-ph.GA]`.

Strandet, M. L. et al. (May 2016). The Redshift Distribution of Dusty Star-forming Galaxies from the SPT Survey. 822.2, 80, p. 80. DOI: `10.3847/0004-637X/822/2/80`. arXiv: `1603.05094 [astro-ph.GA]`.

Béthermin, Matthieu et al. (Nov. 2017). The impact of clustering and angular resolution on far-infrared and millimeter continuum observations. 607, A89, A89. DOI: `10.1051/0004-6361/201730866`. arXiv: `1703.08795 [astro-ph.GA]`.

Bourne, N. et al. (May 2017). Evolution of cosmic star formation in the SCUBA-2 Cosmology Legacy Survey. 467.2, pp. 1360–1385. DOI: `10.1093/mnras/stx031`. arXiv: `1607.04283 [astro-ph.GA]`.

Brown, Michael J. I. et al. (Oct. 2017). Calibration of Ultraviolet, Mid-infrared, and Radio Star Formation Rate Indicators. 847.2, 136, p. 136. DOI: `10.3847/1538-4357/aa8ad2`. arXiv: `1709.00183 [astro-ph.GA]`.

Casey, Caitlin M. et al. (May 2017). Near-infrared MOSFIRE Spectra of Dusty Star-forming Galaxies at $0.2 < z < 4$. 840.2, 101, p. 101. DOI: `10.3847/1538-4357/aa6cb1`. arXiv: `1703.10168 [astro-ph.GA]`.

Ciesla, L. et al. (Dec. 2017). The SFR-M_* main sequence archetypal star-formation history and analytical models. 608, A41, A41. DOI: `10.1051/0004-6361/201731036`. arXiv: `1706.08531 [astro-ph.GA]`.

Combes, Francoise (Sept. 2017). AGN feedback and its quenching efficiency. *Frontiers in Astronomy and Space Sciences* 4, 10, p. 10. DOI: `10.3389/fspas.2017.00010`. arXiv: `1707.09621 [astro-ph.GA]`.

Côté, Benoit et al. (Feb. 2017). The Impact of Modeling Assumptions in Galactic Chemical Evolution Models. 835.2, 128, p. 128. DOI: `10.3847/1538-4357/835/2/128`. arXiv: `1604.07824 [astro-ph.GA]`.

Cucciati, O. et al. (June 2017). The VIMOS Public Extragalactic Redshift Survey (VIPERS). The decline of cosmic star formation: quenching, mass, and environment connections. 602, A15, A15. DOI: `10.1051/0004-6361/201630113`. arXiv: `1611.07049 [astro-ph.GA]`.

Cullen, F. et al. (Sept. 2017). The First Billion Years project: constraining the dust attenuation law of star-forming galaxies at z 5. 470.3, pp. 3006–3026. DOI: `10.1093/mnras/stx1451`. arXiv: `1701.07869 [astro-ph.GA]`.

Dunlop, J. S. et al. (Apr. 2017). A deep ALMA image of the Hubble Ultra Deep Field. 466.1, pp. 861–883. DOI: `10.1093/mnras/stw3088`. arXiv: `1606.00227 [astro-ph.GA]`.

Ferrara, A. et al. (Nov. 2017). The infrared-dark dust content of high redshift galaxies. 471.4, pp. 5018–5024. DOI: `10.1093/mnras/stx1898`. arXiv: `1607.01824 [astro-ph.GA]`.

Fujimoto, Seiji et al. (Nov. 2017). Demonstrating a New Census of Infrared Galaxies with ALMA (DANCING-ALMA). I. FIR Size and Luminosity Relation at $z = 0$-6 Revealed with 1034 ALMA Sources. 850.1, 83, p. 83. DOI: `10.3847/1538-4357/aa93e6`. arXiv: `1703.02138 [astro-ph.GA]`.

Hirashita, Hiroyuki et al. (Dec. 2017). Dust masses of $z > 5$ galaxies from SED fitting and ALMA upper limits. 472.4, pp. 4587–4597. DOI: `10.1093/mnras/stx2349`. arXiv: `1709.02526 [astro-ph.GA]`.

Hurley, P. D. et al. (Jan. 2017). HELP: XID+, the probabilistic de-blender for Herschel SPIRE maps. 464.1, pp. 885–896. DOI: `10.1093/mnras/stw2375`. arXiv: `1606.05770 [astro-ph.GA]`.

Ikarashi, Soh et al. (Nov. 2017). Very Compact Millimeter Sizes for Composite Star-forming/AGN Submillimeter Galaxies. 849.2, L36, p. L36. DOI: `10.3847/2041-8213/aa9572`. arXiv: `1710.09021 [astro-ph.GA]`.

Krywult, J. et al. (Feb. 2017). The VIMOS Public Extragalactic Redshift Survey (VIPERS). The coevolution of galaxy morphology and colour to z 1. 598, A120, A120. DOI: `10.1051/0004-6361/201628953`. arXiv: `1605.05502 [astro-ph.GA]`.

Lo Faro, B. et al. (Dec. 2017). Characterizing the UV-to-NIR shape of the dust attenuation curve of IR luminous galaxies up to $z \sim 2$. 472.2, pp. 1372–1391. DOI: `10.1093/mnras/stx1901`. arXiv: `1707.09805 [astro-ph.GA]`.

Małek, K. et al. (Feb. 2017). [Ultra] luminous infrared galaxies selected at 90 μm in the AKARI deep field: a study of AGN types contributing to their infrared emission. 598, A1, A1. DOI: 10.1051/0004-6361/201527969. arXiv: 1611.07410 [astro-ph.GA].

Pearson, W. J. et al. (July 2017). De-blending deep Herschel surveys: A multi-wavelength approach. 603, A102, A102. DOI: 10.1051/0004-6361/201630105. arXiv: 1704.02192 [astro-ph.GA].

Popping, Gergö et al. (Nov. 2017). The dust content of galaxies from z = 0 to z = 9. 471.3, pp. 3152–3185. DOI: 10.1093/mnras/stx1545. arXiv: 1609.08622 [astro-ph.GA].

Smolčić, V. et al. (June 2017). The VLA-COSMOS 3 GHz Large Project: Continuum data and source catalog release. 602, A1, A1. DOI: 10.1051/0004-6361/201628704. arXiv: 1703.09713 [astro-ph.GA].

Wakelam, Valentine et al. (Dec. 2017). H_2 formation on interstellar dust grains: The viewpoints of theory, experiments, models and observations. *Molecular Astrophysics* 9, pp. 1–36. DOI: 10.1016/j.molap.2017.11.001. arXiv: 1711.10568 [astro-ph.GA].

Wang, Wei-Chen et al. (Mar. 2017). Dust evolution processes in normal galaxies at z > 6 detected by ALMA. 465.3, pp. 3475–3482. DOI: 10.1093/mnras/stw2966. arXiv: 1611.06654 [astro-ph.GA].

Whitaker, Katherine E. et al. (Dec. 2017). The Constant Average Relationship between Dust-obscured Star Formation and Stellar Mass from z = 0 to z = 2.5. 850.2, 208, p. 208. DOI: 10.3847/1538-4357/aa94ce. arXiv: 1710.06872 [astro-ph.GA].

Wiseman, P. et al. (Mar. 2017). Evolution of the dust-to-metals ratio in high-redshift galaxies probed by GRB-DLAs. 599, A24, A24. DOI: 10.1051/0004-6361/201629228. arXiv: 1607.00288 [astro-ph.GA].

Zahid, H. Jabran et al. (Sept. 2017). Stellar Absorption Line Analysis of Local Star-forming Galaxies: The Relation between Stellar Mass, Metallicity, Dust Attenuation, and Star Formation Rate. 847.1, 18, p. 18. DOI: 10.3847/1538-4357/aa88ae. arXiv: 1708.07107 [astro-ph.GA].

Zhang, Hong-Xin et al. (2017). The Impact of Star Formation Histories on Stellar Mass Estimation: Implications from the Local Group Dwarf Galaxies. *The Astrophysical Journal Supplement Series* 233.1, p. 13. DOI: 10.3847/1538-4365/aa937b. URL: https://dx.doi.org/10.3847/1538-4365/aa937b.

Beeston, R. A. et al. (June 2018). GAMA/H-ATLAS: the local dust mass function and cosmic density as a function of galaxy type - a benchmark for models of galaxy evolution. 479.1, pp. 1077–1099. DOI: 10.1093/mnras/sty1460. arXiv: 1712.07261 [astro-ph.GA].

Buat, V. et al. (Nov. 2018). Dust attenuation and Hα emission in a sample of galaxies observed with Herschel at 0.6 < z < 1.6. 619, A135, A135. DOI: 10.1051/0004-6361/201833841. arXiv: 1809.00161 [astro-ph.GA].

Carnall, A. C. et al. (Nov. 2018). Inferring the star formation histories of massive quiescent galaxies with BAGPIPES: evidence for multiple quenching mechanisms. 480.4, pp. 4379–4401. DOI: 10.1093/mnras/sty2169. arXiv: 1712.04452 [astro-ph.GA].

Ciesla, L. et al. (July 2018). Identification of galaxies that experienced a recent major drop of star formation. 615, A61, A61. DOI: 10.1051/0004-6361/201832715. arXiv: 1803.10239 [astro-ph.GA].

Duncan, Kenneth J. et al. (Jan. 2018). Photometric redshifts for the next generation of deep radio continuum surveys - I. Template fitting. 473.2, pp. 2655–2672. DOI: 10.1093/mnras/stx2536. arXiv: 1709.09183 [astro-ph.GA].

Durkalec, A. et al. (Apr. 2018). The VIMOS Ultra Deep Survey. Luminosity and stellar mass dependence of galaxy clustering at z 3. 612, A42, A42. DOI: 10.1051/0004-6361/201730734. arXiv: 1703.02049 [astro-ph.GA].

Elbaz, D. et al. (Aug. 2018). Starbursts in and out of the star-formation main sequence. 616, A110, A110. DOI: 10.1051/0004-6361/201732370. arXiv: 1711.10047 [astro-ph.GA].

Galliano, Frédéric et al. (Sept. 2018). The Interstellar Dust Properties of Nearby Galaxies. 56, pp. 673–713. DOI: 10.1146/annurev-astro-081817-051900. arXiv: 1711.07434 [astro-ph.GA].

Jin, Shuowen et al. (Sept. 2018). "Super-deblended" Dust Emission in Galaxies. II. Far-IR to (Sub)millimeter Photometry and High-redshift Galaxy Candidates in the Full COSMOS Field. 864.1, 56, p. 56. DOI: 10.3847/1538-4357/aad4af. arXiv: 1807.04697 [astro-ph.GA].

Koprowski, M. P. et al. (Oct. 2018). A direct calibration of thtae IRX-β relation in Lyman-break Galaxies at z = 3-5. 479.4, pp. 4355–4366. DOI: 10.1093/mnras/sty1527. arXiv: 1801.00791 [astro-ph.GA].

Lapi, A. et al. (Apr. 2018). The Dramatic Size and Kinematic Evolution of Massive Early-type Galaxies. 857.1, 22, p. 22. DOI: 10.3847/1538-4357/aab6af. arXiv: 1803.04734 [astro-ph.GA].

Leja, Joel et al. (Feb. 2018). Hot Dust in Panchromatic SED Fitting: Identification of Active Galactic Nuclei and Improved Galaxy Properties. 854.1, 62, p. 62. DOI: 10.3847/1538-4357/aaa8db. arXiv: 1709.04469 [astro-ph.GA].

Małek, K. et al. (Nov. 2018). HELP: modelling the spectral energy distributions of Herschel detected galaxies in the ELAIS N1 field. 620, A50, A50. DOI: 10.1051/0004-6361/201833131. arXiv: 1809.00529 [astro-ph.GA].

Matsuoka, K. et al. (2018). The mass-metallicity relation of high-z type-2 active galactic nuclei. *A&A* 616, p. L4. DOI: 10.1051/0004-6361/201833418. URL: https://doi.org/10.1051/0004-6361/201833418.

McLure, R. J. et al. (May 2018). Dust attenuation in 2 < z < 3 star-forming galaxies from deep ALMA observations of the Hubble Ultra Deep Field. 476.3, pp. 3991–4006. DOI: 10.1093/mnras/sty522. arXiv: 1709.06102 [astro-ph.GA].

Merlin, E. et al. (2018). Chasing passive galaxies in the early Universe: a critical analysis in CANDELS GOODS-South. 473.2, pp. 2098–2123. DOI: 10.1093/mnras/stx2385. arXiv: 1709.00429 [astro-ph.GA].

Miyazaki, Satoshi et al. (Jan. 2018). Hyper Suprime-Cam: System design and verification of image quality. 70, S1, S1. DOI: 10.1093/pasj/psx063.

Narayanan, Desika et al. (Dec. 2018). A Theory for the Variation of Dust Attenuation Laws in Galaxies. 869.1, 70, p. 70. DOI: 10.3847/1538-4357/aaed25. arXiv: 1805.06905 [astro-ph.GA].

Nicastro, F. et al. (June 2018). Observations of the missing baryons in the warm-hot intergalactic medium. 558.7710, pp. 406–409. DOI: 10.1038/s41586-018-0204-1. arXiv: 1806.08395 [astro-ph.GA].

Pearson, W. J. et al. (July 2018). Main sequence of star forming galaxies beyond the Herschel confusion limit. 615, A146, A146. DOI: 10.1051/0004-6361/201832821. arXiv: 1804.03482 [astro-ph.GA].

Reddy, Naveen A. et al. (Jan. 2018). The HDUV Survey: A Revised Assessment of the Relationship between UV Slope and Dust Attenuation for High-redshift Galaxies. 853.1, 56, p. 56. DOI: 10.3847/1538-4357/aaa3e7. arXiv: 1705.09302 [astro-ph.GA].

Salim, Samir et al. (May 2018). Dust Attenuation Curves in the Local Universe: Demographics and New Laws for Star-forming Galaxies and High-redshift Analogs. 859.1, 11, p. 11. DOI: 10.3847/1538-4357/aabf3c. arXiv: 1804.05850 [astro-ph.GA].

Schreiber, C. et al. (2018a). Jekyll & Hyde: quiescence and extreme obscuration in a pair of massive galaxies 1.5 Gyr after the Big Bang. 611, A22, A22. DOI: 10.1051/0004-6361/201731917. arXiv: 1709.03505 [astro-ph.GA].

Schreiber, C. et al. (Oct. 2018b). Near infrared spectroscopy and star-formation histories of 3 ≤ z ≤ 4 quiescent galaxies. 618, A85, A85. DOI: 10.1051/0004-6361/201833070. arXiv: 1807.02523 [astro-ph.GA].

Scodeggio, M. et al. (Jan. 2018). The VIMOS Public Extragalactic Redshift Survey (VIPERS). Full spectroscopic data and auxiliary information release (PDR-2). 609, A84, A84. DOI: 10.1051/0004-6361/201630114. arXiv: 1611.07048 [astro-ph.GA].

Wang, Weichen et al. (Dec. 2018). Galaxy Inclination and the IRX-β Relation: Effects on UV Star Formation Rate Measurements at Intermediate to High Redshifts. 869.2, 161, p. 161. DOI: 10.3847/1538-4357/aaef79. arXiv: 1811.03671 [astro-ph.GA].

Battisti, A. J. et al. (Sept. 2019). MAGPHYS+photo-z: Constraining the Physical Properties of Galaxies with Unknown Redshifts. 882.1, 61, p. 61. DOI: 10.3847/1538-4357/ab345d. arXiv: 1908.00771 [astro-ph.GA].

Behroozi, Peter et al. (Sept. 2019). UNIVERSEMACHINE: The correlation between galaxy growth and dark matter halo assembly from z = 0-10. 488.3, pp. 3143–3194. DOI: 10.1093/mnras/stz1182. arXiv: 1806.07893 [astro-ph.GA].

Boquien, M. et al. (Feb. 2019). CIGALE: a python Code Investigating GALaxy Emission. 622, A103, A103. DOI: 10.1051/0004-6361/201834156. arXiv: 1811.03094 [astro-ph.GA].

Buat, V. et al. (Dec. 2019). Cold dust and stellar emissions in dust-rich galaxies observed with ALMA: a challenge for SED-fitting techniques. 632, A79, A79. DOI: 10.1051/0004-6361/201936643.

Chevallard, Jacopo et al. (Feb. 2019). Simulating and interpreting deep observations in the Hubble Ultra Deep Field with the JWST/NIRSpec low-resolution 'prism'. 483.2, pp. 2621–2640. DOI: 10.1093/mnras/sty2426. arXiv: 1711.07481 [astro-ph.GA].

Cook, B. A. et al. (May 2019). Measuring Star Formation Histories, Distances, and Metallicities with Pixel Color-Magnitude Diagrams. I. Model Definition and Mock Tests. 876.1, 78, p. 78. DOI: 10.3847/1538-4357/ab16e5. arXiv: 1904.00011 [astro-ph.GA].

Decarli, Roberto et al. (Sept. 2019). The ALMA Spectroscopic Survey in the HUDF: CO Luminosity Functions and the Molecular Gas Content of Galaxies through Cosmic History. 882.2, 138, p. 138. DOI: 10.3847/1538-4357/ab30fe. arXiv: 1903.09164 [astro-ph.GA].

Decleir, Marjorie et al. (June 2019). Revealing the dust attenuation properties on resolved scales in NGC 628 with SWIFT UVOT data. 486.1, pp. 743–767. DOI: 10.1093/mnras/stz805. arXiv: 1903.06715 [astro-ph.GA].

Falkendal, Theresa et al. (Jan. 2019). Massive galaxies on the road to quenching: ALMA observations of powerful high redshift radio galaxies. 621, A27, A27. DOI: 10.1051/0004-6361/201732485. arXiv: 1809.09427 [astro-ph.GA].

Hou, L. G. et al. (Nov. 2019). Radio recombination line observations towards Spitzer infrared bubbles with the TianMa radio telescope. 489.4, pp. 4862–4874. DOI: 10.1093/mnras/stz2466.

Leśniewska, Aleksandra et al. (Apr. 2019). Dust production scenarios in galaxies at z ∼6-8.3. 624, L13, p. L13. DOI: 10.1051/0004-6361/201935149. arXiv: 1904.11185 [astro-ph.GA].

Li, Qi et al. (Nov. 2019a). The dust-to-gas and dust-to-metal ratio in galaxies from z = 0 to 6. 490.1, pp. 1425–1436. DOI: 10.1093/mnras/stz2684. arXiv: 1906.09277 [astro-ph.GA].

Li, Yuan et al. (Dec. 2019b). The Fate of Asymptotic Giant Branch Winds in Massive Galaxies and the Intracluster Medium. 887.1, 41, p. 41. DOI: 10.3847/1538-4357/ab4bca. arXiv: 1901.10481 [astro-ph.GA].

Liu, Daizhong et al. (2019). Automated Mining of the ALMA Archive in the COSMOS Field (A3COSMOS). I. Robust ALMA Continuum Photometry Catalogs and Stellar Mass and Star Formation Properties for ∼700 Galaxies at z = 0.5–6. *ApJS* 244.2, p. 40. DOI: 10.3847/1538-4365/ab42da. URL: https://doi.org/10.3847%2F1538-4365%2Fab42da.

Pantoni, L. et al. (Aug. 2019). New Analytic Solutions for Galaxy Evolution: Gas, Stars, Metals, and Dust in Local ETGs and Their High-z Star-forming Progenitors. 880.2, 129, p. 129. DOI: 10.3847/1538-4357/ab2adc. arXiv: 1906.07458 [astro-ph.GA].

Pearson, W. J. et al. (Nov. 2019). Effect of galaxy mergers on star-formation rates. 631, A51, A51. DOI: 10.1051/0004-6361/201936337. arXiv: 1908.10115 [astro-ph.GA].

Puglisi, A. et al. (June 2019). The Main Sequence at z 1.3 Contains a Sizable Fraction of Galaxies with Compact Star Formation Sizes: A New Population of Early Post-starbursts? 877.2, L23, p. L23. DOI: 10.3847/2041-8213/ab1f92. arXiv: 1905.02958 [astro-ph.GA].

Salim, Samir et al. (Feb. 2019). Diversity of Galaxy Dust Attenuation Curves Drives the Scatter in the IRX-β Relation. 872.1, 23, p. 23. DOI: 10.3847/1538-4357/aaf88a. arXiv: 1812.05606 [astro-ph.GA].

Shirley, Raphael et al. (Nov. 2019). HELP: a catalogue of 170 million objects, selected at 0.36-4.5 μm, from 1270 deg^2 of prime extragalactic fields. 490.1, pp. 634–656. DOI: 10.1093/mnras/stz2509. arXiv: 1909.04003 [astro-ph.GA].

Wang, T. et al. (Aug. 2019). A dominant population of optically invisible massive galaxies in the early Universe. 572.7768, pp. 211–214. DOI: 10.1038/s41586-019-1452-4. arXiv: 1908.02372 [astro-ph.GA].

Xie, Yanxia et al. (Oct. 2019). A New Calibration of Star Formation Rate in Galaxies Based on Polycyclic Aromatic Hydrocarbon Emission. 884.2, 136, p. 136. DOI: 10.3847/1538-4357/ab4200. arXiv: 1909.01110 [astro-ph.GA].

Aufort, G. et al. (Mar. 2020). Constraining the recent star formation history of galaxies: an approximate Bayesian computation approach. 635, A136, A136. DOI: 10.1051/0004-6361/201936788. arXiv: 2002.07815 [astro-ph.GA].

Béthermin, M. et al. (Nov. 2020). The ALPINE-ALMA [CII] survey: Data processing, catalogs, and statistical source properties. 643, A2, A2. DOI: 10.1051/0004-6361/202037649. arXiv: 2002.00962 [astro-ph.GA].

Burgarella, D. et al. (May 2020). Observational and theoretical constraints on the formation and early evolution of the first dust grains in galaxies at 5 < z < 10. 637, A32, A32. DOI: 10.1051/0004-6361/201937143. arXiv: 2002.01858 [astro-ph.GA].

Carnall, A. C. et al. (July 2020). Timing the earliest quenching events with a robust sample of massive quiescent galaxies at 2 < z < 5. 496.1, pp. 695–707. DOI: 10.1093/mnras/staa1535. arXiv: 2001.11975 [astro-ph.GA].

Cassata, P. et al. (Nov. 2020). The ALPINE-ALMA [CII] survey. Small Lyα-[CII] velocity offsets in main-sequence galaxies at 4.4 < z < 6. 643, A6, A6. DOI: 10.1051/0004-6361/202037517. arXiv: 2002.00967 [astro-ph.GA].

Ciesla, L. et al. (Mar. 2020). A hyper luminous starburst at z = 4.72 magnified by a lensing galaxy pair at z = 1.48. 635, A27, A27. DOI: 10.1051/0004-6361/201936727. arXiv: 2001.03641 [astro-ph.GA].

Curti, Mirko et al. (Jan. 2020). The mass-metallicity and the fundamental metallicity relation revisited on a fully T_e-based abundance scale for galaxies. 491.1, pp. 944–964. DOI: 10.1093/mnras/stz2910. arXiv: 1910.00597 [astro-ph.GA].

Donevski, D. et al. (Dec. 2020). In pursuit of giants. I. The evolution of the dust-to-stellar mass ratio in distant dusty galaxies. 644, A144, A144. DOI: 10.1051/0004-6361/202038405. arXiv: 2008.09995 [astro-ph.GA].

Faisst, A. L. et al. (Apr. 2020). The ALPINE-ALMA [C II] Survey: Multiwavelength Ancillary Data and Basic Physical Measurements. 247.2, 61, p. 61. DOI: 10.3847/1538-4365/ab7ccd. arXiv: 1912.01621 [astro-ph.GA].

Fudamoto, Y. et al. (Nov. 2020). The ALPINE-ALMA [CII] survey. Dust attenuation properties and obscured star formation at z ∼ 4.4-5.8. 643, A4, A4. DOI: 10.1051/0004-6361/202038163. arXiv: 2004.10760 [astro-ph.GA].

González-López, Jorge et al. (July 2020). The ALMA Spectroscopic Survey in the HUDF: Deep 1.2 mm Continuum Number Counts. 897.1, 91, p. 91. DOI: 10.3847/1538-4357/ab765b. arXiv: 2002.07199 [astro-ph.GA].

Gruppioni, C. et al. (Nov. 2020). The ALPINE-ALMA [CII] survey. The nature, luminosity function, and star formation history of dusty galaxies up to z 6. 643, A8, A8. DOI: 10.1051/0004-6361/202038487. arXiv: 2006.04974 [astro-ph.GA].

Khusanova, Y. et al. (July 2020). The ALPINE-ALMA [CII] Survey: Obscured Star Formation Rate Density and Main Sequence of star-forming galaxies at z>4. *arXiv e-prints*, arXiv:2007.08384, arXiv:2007.08384. arXiv: 2007.08384 [astro-ph.GA].

Li, Niu et al. (June 2020). Estimating Dust Attenuation from Galactic Spectra. I. Methodology and Tests. 896.1, 38, p. 38. DOI: 10.3847/1538-4357/ab92a1. arXiv: 2001.02815 [astro-ph.GA].

Lower, Sidney et al. (Nov. 2020). How Well Can We Measure the Stellar Mass of a Galaxy: The Impact of the Assumed Star Formation History Model in SED Fitting. 904.1, 33, p. 33. DOI: 10.3847/1538-4357/abbfa7. arXiv: 2006.03599 [astro-ph.GA].

Nanni, A. et al. (Sept. 2020). The gas, metal, and dust evolution in low-metallicity local and high-redshift galaxies. 641, A168, A168. DOI: 10.1051/0004-6361/202037833. arXiv: 2006.15146 [astro-ph.GA].

Planck Collaboration et al. (Sept. 2020). Planck 2018 results. VI. Cosmological parameters. 641, A6, A6. DOI: 10.1051/0004-6361/201833910. arXiv: 1807.06209 [astro-ph.CO].

Reuter, C. et al. (Oct. 2020). The Complete Redshift Distribution of Dusty Star-forming Galaxies from the SPT-SZ Survey. 902.1, 78, p. 78. DOI: 10.3847/1538-4357/abb599. arXiv: 2006.14060 [astro-ph.GA].

Riechers, Dominik A. et al. (June 2020). VLA-ALMA Spectroscopic Survey in the Hubble Ultra Deep Field (VLASPECS): Total Cold Gas Masses and CO Line Ratios for z = 2-3 Main-sequence Galaxies. 896.2, L21, p. L21. DOI: 10.3847/2041-8213/ab9595. arXiv: 2005.09653 [astro-ph.GA].

Salim, Samir et al. (Aug. 2020). The Dust Attenuation Law in Galaxies. 58, pp. 529–575. DOI: 10.1146/annurev-astro-032620-021933. arXiv: 2001.03181 [astro-ph.GA].

Schulz, Sebastian et al. (Oct. 2020). A redshift-dependent IRX-β dust attenuation relation for TNG50 galaxies. 497.4, pp. 4773–4794. DOI: 10.1093/mnras/staa1900. arXiv: 2001.04992 [astro-ph.GA].

Shivaei, Irene et al. (Nov. 2020). Dependence of the IRX-β Dust Attenuation Relation on Metallicity and Environment. 903.2, L28, p. L28. DOI: 10.3847/2041-8213/abc1ef. arXiv: 2010.10538 [astro-ph.GA].

Slavin, Jonathan D. et al. (Oct. 2020). The Dynamics, Destruction, and Survival of Supernova-formed Dust Grains. 902.2, 135, p. 135. DOI: 10.3847/1538-4357/abb5a4. arXiv: 2009.01895 [astro-ph.HE].

Trayford, James W. et al. (Jan. 2020). Fade to grey: systematic variation of galaxy attenuation curves with galaxy properties in the EAGLE simulations. 491.3, pp. 3937–3951. DOI: 10.1093/mnras/stz3234. arXiv: 1908.08956 [astro-ph.GA].

Valentino, F. et al. (Sept. 2020). CO emission in distant galaxies on and above the main sequence. 641, A155, A155. DOI: 10.1051/0004-6361/202038322. arXiv: 2006.12521 [astro-ph.GA].

Wang, Ting-Wen et al. (Dec. 2020). Extinction-free Census of AGNs in the AKARI/IRC North Ecliptic Pole Field from 23-band infrared photometry from Space Telescopes. 499.3, pp. 4068–4081. DOI: 10.1093/mnras/staa2988. arXiv: 2010.08225 [astro-ph.GA].

Wenzel, G. et al. (Sept. 2020). Astrochemical relevance of VUV ionization of large PAH cations. 641, A98, A98. DOI: 10.1051/0004-6361/202038139. arXiv: 2005.02103 [astro-ph.GA].

Zelko, Ioana A. et al. (Nov. 2020). Implications of Grain Size Distribution and Composition for the Correlation between Dust Extinction and Emissivity. 904.1, 38, p. 38. DOI: 10. 3847/1538-4357/abbb8d. arXiv: 2009.11869 [astro-ph.GA].

Calzetti, Daniela et al. (May 2021). Revisiting Attenuation Curves: The Case of NGC 3351. 913.1, 37, p. 37. DOI: 10.3847/1538-4357/abf118. arXiv: 2103.12117 [astro-ph.GA].

Ferreras, Ignacio et al. (July 2021). Constraints on the dust extinction law of the Galaxy with Swift/UVOT, Gaia, and 2MASS. 505.1, pp. 283–292. DOI: 10.1093/mnras/stab1270. arXiv: 2105.02240 [astro-ph.GA].

Hamed, M. et al. (Feb. 2021). Multiwavelength dissection of a massive heavily dust-obscured galaxy and its blue companion at z∼2. 646, A127, A127. DOI: 10.1051/0004-6361/ 202039577. arXiv: 2101.07724 [astro-ph.GA].

Lin, Yen-Hsing et al. (Oct. 2021). Geometry effects on dust attenuation curves with different grain sources at high redshift. 507.2, pp. 2755–2765. DOI: 10.1093/mnras/stab2242. arXiv: 2109.03072 [astro-ph.GA].

Pantoni, L. et al. (Nov. 2021a). An ALMA view of 11 dusty star-forming galaxies at the peak of cosmic star formation history. 507.3, pp. 3998–4015. DOI: 10.1093/mnras/ stab2346. arXiv: 2108.05596 [astro-ph.GA].

Pantoni, L. et al. (June 2021b). Unveiling the nature of 11 dusty star-forming galaxies at the peak of cosmic star formation history. 504.1, pp. 928–950. DOI: 10.1093/mnras/ stab674. arXiv: 2103.05011 [astro-ph.GA].

Schouws, Sander et al. (May 2021). Significant Dust-Obscured Star Formation in Luminous Lyman-break Galaxies at *z*∼7−8. *arXiv e-prints*, arXiv:2105.12133, arXiv:2105.12133. arXiv: 2105.12133 [astro-ph.GA].

Shirley, R. et al. (May 2021). HELP: The Herschel Extragalactic Legacy Project. *arXiv e-prints*, arXiv:2105.05659, arXiv:2105.05659. arXiv: 2105.05659 [astro-ph.GA].

Villa-Vélez, J. A. et al. (Oct. 2021). Fitting spectral energy distributions of FMOS-COSMOS emission-line galaxies at z ∼ 1.6: Star formation rates, dust attenuation, and [OIII]λ5007 emission-line luminosities. 654, A153, A153. DOI: 10.1051/0004-6361/202140890. arXiv: 2108.13321 [astro-ph.GA].

Aihara, Hiroaki et al. (Apr. 2022). Third data release of the Hyper Suprime-Cam Subaru Strategic Program. 74.2, pp. 247–272. DOI: 10.1093/pasj/psab122. arXiv: 2108. 13045 [astro-ph.IM].

Boquien, Médéric et al. (July 2022). The ALPINE-ALMA [C II] survey. Dust attenuation curves at z = 4.4-5.5. 663, A50, A50. DOI: 10.1051/0004-6361/202142537. arXiv: 2202.11723 [astro-ph.GA].

Figueira, M. et al. (Nov. 2022). SFR estimations from z = 0 to z = 0.9. A comparison of SFR calibrators for star-forming galaxies. 667, A29, A29. DOI: 10.1051/0004-6361/ 202141701. arXiv: 2209.04390 [astro-ph.GA].

Gómez-Guijarro, C. et al. (Feb. 2022). GOODS-ALMA 2.0: Source catalog, number counts, and prevailing compact sizes in 1.1 mm galaxies. 658, A43, A43. DOI: 10.1051/0004- 6361/202141615. arXiv: 2106.13246 [astro-ph.GA].

Hamed, Mahmoud et al. (Oct. 2022). Dust attenuation in Ultra Dusty Star-Forming galaxies up to z ∼ 4. *XL Polish Astronomical Society Meeting*. Ed. by Ewa Szuszkiewicz et al. Vol. 12, pp. 38–41.

Lower, Sidney et al. (May 2022). How Well Can We Measure Galaxy Dust Attenuation Curves? The Impact of the Assumed Star-dust Geometry Model in Spectral Energy Distribution Fitting. 931.1, 14, p. 14. DOI: 10.3847/1538-4357/ac6959. arXiv: 2203. 00074 [astro-ph.GA].

Pistis, F. et al. (July 2022). The fundamental metallicity relation from SDSS (z ∼ 0) to VIPERS (z ∼ 0.7). Data selection or evolution. 663, A162, A162. DOI: 10.1051/0004- 6361/202142430. arXiv: 2206.02458 [astro-ph.GA].

Qin, Jianbo et al. (Mar. 2022). Systematic biases in determining dust attenuation curves through galaxy SED fitting. 511.1, pp. 765–783. DOI: 10.1093/mnras/stac132. arXiv: 2201.05467 [astro-ph.GA].

Shen, Xuejian et al. (Jan. 2022). High-redshift predictions from IllustrisTNG – III. Infrared luminosity functions, obscured star formation, and dust temperature of high-redshift galaxies. *Monthly Notices of the Royal Astronomical Society* 510.4, pp. 5560–5578. ISSN: 0035-8711. DOI: 10.1093/mnras/stab3794. eprint: https://academic.oup.com/mnras/article-pdf/510/4/5560/42259009/stab3794.pdf. URL: https://doi.org/10.1093/mnras/stab3794.

Siudek, M. et al. (Oct. 2022). Shaping physical properties of galaxy subtypes in the VIPERS survey: Environment matters. 666, A131, A131. DOI: 10.1051/0004-6361/202243613. arXiv: 2205.14736 [astro-ph.GA].

Xie, Yanxia et al. (Feb. 2022). The Ionization and Destruction of Polycyclic Aromatic Hydrocarbons in Powerful Quasars. 925.2, 218, p. 218. DOI: 10.3847/1538-4357/ac32e2. arXiv: 2110.09705 [astro-ph.GA].

Adams, N. J. et al. (Jan. 2023). Discovery and properties of ultra-high redshift galaxies (9 < z < 12) in the JWST ERO SMACS 0723 Field. 518.3, pp. 4755–4766. DOI: 10.1093/mnras/stac3347. arXiv: 2207.11217 [astro-ph.GA].

Carnall, A. C. et al. (Apr. 2023). A surprising abundance of massive quiescent galaxies at 3 < z < 5 in the first data from JWST CEERS. 520.3, pp. 3974–3985. DOI: 10.1093/mnras/stad369. arXiv: 2208.00986 [astro-ph.GA].

Hamed, M. et al. (Apr. 2023). The slippery slope of dust attenuation curves: Correlation of dust attenuation laws with star-to-dust compactness up to z = 4. *arXiv e-prints*, arXiv:2304.13713, arXiv:2304.13713. DOI: 10.48550/arXiv.2304.13713. arXiv: 2304.13713 [astro-ph.GA].

Zhang, Lulu et al. (Jan. 2023). The Contribution of Evolved Stars to Polycyclic Aromatic Hydrocarbon Heating and Implications for Estimating Star Formation Rates. 943.1, 60, p. 60. DOI: 10.3847/1538-4357/acab60. arXiv: 2212.05688 [astro-ph.GA].